Judicious Design of Transition Metal Complexes for Photochemical Energy Conversion

Jonathan Abel Porras

SUBMITTED IN PARTIAL FULFILLMENT OF THE REQUIREMENTS FOR THE DEGREE OF DOCTOR OF PHILOSOPHY IN THE SUBJECT OF CHEMISTRY

Committee Members

Prof. Stefan Bernhard (Advisor)

Prof. Terrence J. Collins (Chair)

Prof. Marcel P. Bruchez

Prof. Kay M. Brummond (External Member, University of Pittsburgh)

Carnegie Mellon University

Pittsburgh, PA

July 2017

Abstract

In order for society to have a smooth transition away from carbonaceous fuels that continue to put undue stress on the environment, robust research into alternative, sustainable energy sources are of paramount importance. In particular, solar is a prime candidate given its abundance and minimal environmental consequences through its use compared to fossil fuels. While intermittent sunlight can diminish the value of using photovoltaics for a full 24-hour day, it is possible to store that energy into what can be considered a "solar fuel", with hydrogen being an ideal target. Similarly, the use of light energy can drive numerous reactions that are valuable to fields such as industrial synthesis, medicine, and sanitation, at a fraction of their current energy inputs.

This work reports on the design of new Ir(III) based photosensitizers that address concerns from previously established complex structures. Replacement of a labile bipyridine with an electron rich terpyridine imparts greater stability and photocatalytic abilities in highly coordinating solvent environments, which are known to degrade previously established photosensitizers. These complexes were assessed photophysically, electrochemically, computationally, as well as for photocatalytic hydrogen generation from water. The photosensitizers were also used for photoredox catalysis, a burgeoning area of research that uses light energy to drive synthetic transformations.

In addition, this work reports on the switching of a terpyridine ligand to a bis-quinolylpyridine for Ir(III) photosensitizers. This new ligand allows for improved coordination ability to the Ir center, and imparts an enhancement to several properties when compared to the corresponding bipyridine analogue. The complexes see excited state lifetimes as high as 30 microseconds, which is notable for Ir(III) complexes given

that there are no additional organic dye molecules tethered to the complexes, a common strategy employed to extend excited state lifetimes. The complexes were assessed as photosensitizers not only for photocatalytic hydrogen generation and photoredox catalysis, but also for singlet oxygen generation, where a longer excited state lifetime is advantageous.

Finally, this work reports the synthesis of Fe(II), Zn(II) and Ru(II) based hemicaged complexes that utilize the more rigid phenanthroline ligand in place of the traditional bipyridine. The ligand synthesis required adaptation for the phenanthroline moiety but also allowed for synthesis of a corresponding mesityl-capped hemicage as well. The complexes were evaluated photophysically and electrochemically in order to determine the effects of hemicaging on the ground state and excited state properties when compared to the corresponding phenanthroline analogues.

Acknowledgements

Welcome to the mainstage of my doctoral dissertation! For this final challenge, I've been asked to compile, assess, review, and submit a body of work worthy of a Doctorate of Philosophy in Chemistry, courtesy of Carnegie Mellon University. Now before we get to that, there's some important people that need to be thanked. Reader! Start your engines, and may my acknowledgement section win!

What you just read was a reference to a particular TV show that I wanted to acknowledge as one of the biggest sources of stability and sanity for me throughout my whole PhD. Cheers if you know what it is and if not, thank RuPaul! Now here we have the list of people I need to thank.

One of the first people that should be thanked is my advisor, Professor Stefan Bernhard aka Bossman. I can still vividly remember the first time I met you in your office, you saw my last name and immediately asked if I was Costa Rican. You were certainly right! Between the "Costa Rican vs Puerto Rican" jokes commiserating with me about things that made New Jersey awesome (yes, it is), and being a Mac user, I knew working with you for the next few years would be a great choice. I appreciate the spread of projects you gave me, and even when things were getting frustrating in the lab, having an "open" office door to come into made things easier. You were always honest and straightforward about so many things over the course of my graduate career, and looking back, I thank you for that. You've given me so many opportunities in and out of lab that have made for a phenomenal graduate experience.

A big thanks to the all the members of the Bernhard Lab who I've had the pleasure of working with over these past few years. It's been great to have a solid group

of people who I learned from, collaborated with, and could always go to for advice on any number of things. Thanks to my fellow “Bernlab” graduate students Anthony Brooks, James Woods, Danielle Chirdon, Husain Kagalwala, Mo Li, Isaac Mills, and Velabo Mdluli. I can’t imagine having made it through the PhD without you all. I’ve also had several amazing undergraduate students who have contributed to my work, and am thankful for having had the chance to mentor them, especially Joshua Zak, Victoria Van Benschoten, and Wesley Transue. There were plenty of other amazing undergraduate students who worked in the lab over my time who I’d also like to thank including Katherine Basore, Andrew Maurer, Nikita Budwal, Maegha Singh, Michael Jopling, and Jacqueline Lewis.

There’s also a number of people within the department that have made my experience as a graduate student go much smoother that deserve thanks. Thanks to Rea Freeland, Valerie Bridge, Sara Wainer, Brenda Chambers, and Tim Sager for handling lots of logistics and always answering questions I’ve had over the years. Also, big thanks to my fellow graduate students and post docs that have come through the department throughout my time here. I’ve also been privileged to work with some amazing faculty not just through research, but through teaching. It was there I really saw and grew to appreciate teaching enough to want to make a career out of it! Thanks to Karen Stump, Gizelle Sherwood, Carolyn Neiderlander, Kevin Hunter, Kelsey Diffley, and Georgene Wittig for making my teaching experience in the department go as smoothly as possible.

While at Carnegie Mellon, I’ve been able to meet and get to know people outside of the department as well. Through founding Carnegie Mellon University’s first Graduate

Student LGBT+ Group, Allies Grad, I've been able to make a great community of graduate students across disciplines. It was a great source of support for me.

Outside of graduate school, I've been fortunate enough to work with some great organizations here in Pittsburgh that have helped keep me just a little saner throughout my PhD. Thank you to Gay for Good: Pittsburgh, for being a place where I could meet so many new people and get to volunteer around Pittsburgh at different organizations. It was a great way to learn more about the city and come to appreciate it. Also thanks to the Humane Animal Rescue (formerly the Western PA Human Society and Animal Rescue League) for giving me the chance to have been a foster home for at least TEN (yes ten) cats and kittens. It was great to have something to home to and keep me occupied whenever I worked late nights at home. I could name all the cats I've fostered but that might make me look even more like a crazy cat person.

I'm especially grateful for my family for coming along with me on this journey. The support from my father Abel, my mother Beatriz Elizabeth, and my sister Claudia have given me over these past few years has been amazing. Being the first person in your family to go after a PhD sure had its challenges. I'm happy to have had such great support from the, whether it was through answering calls and text messages late at night, driving to and from Pittsburgh to fix things that weren't working (outside of the lab), to picking me up from the airport every time I'd come home for an important event, to always making sure I had plenty of home-cooked food to bring back to Pittsburgh. It's hard to imagine having gotten to this point without you all. I love you all very much.

I couldn't complete this acknowledgement section without mentioning good old Thaddeus aka TJ. You've been a solid source of support for me throughout this whole

thing. Whether you were in New Jersey, off to England, or even here in Pittsburgh, I always knew you were there for me. You've done everything from help me edit things, to help keep the apartment in decent shape when things got hectic, to help me make sure I wasn't going to crazy with some outfit choices, to being there when things were going haywire. The list could probably go on and on but I just want you to know I appreciate everything you've done for me. I could write more but let's be honest, you're the English Major/Master of Medieval Literature and could write circles around me. So, I'll end with a good, simple, and heartfelt thank you.

Table of Contents

Abstract iii

Acknowledgements v

List of Figures xiii

List of Schemes xviii

List of Tables xx

List of Abbreviations xxi

Chapter 1. Harnessing the Power of Light 1

1.1 Current Energy Demand *1*

1.2 Light Energy Use and Storage *2*

1.2.1 The Ideal Solar Civilization *2*

1.2.2 The Case for Ir(III) Photosensitizers *3*

1.2.3 Photocatalytic Hydrogen Generation from Water *8*

1.2.4 Photoredox Catalysis for Organic Transformations *13*

1.2.5 Photochemical Generation of Singlet Oxygen *19*

1.3 Summary and Motivation of Thesis *22*

1.4 References *23*

Chapter 2. Push Pull $[Ir(tpy)(ppy)X]^{+}$ Complexes via C-F Insertion 26

2.1 Introduction *26*

2.2 Experimental ***31***

2.2.1 General *31*

2.2.2 Synthetic Procedures *32*

2.2.3 Electrochemical Characterization *38*

2.2.4 Computational Modeling *39*

2.2.5 Photophysical Characterization *39*

2.2.6 Photocatalytic Hydrogen Generation *40*

2.2.7 Photoredox Catalysis *41*

2.3 Results and Discussion ***41***

2.3.1 Synthesis *41*

2.3.2 C-F Activation *44*

2.3.3 Computational Modeling *47*

2.3.4 UV-Vis Absorption Spectroscopy & TD-DFT *48*

2.3.5 Emission Spectroscopy *51*

2.3.6 Electrochemical Characterization *55*

2.3.7 Photocatalytic Hydrogen Evolution *59*

2.3.8 Photoredox Catalysis *60*

2.4 Conclusions ***64***

2.5 References ***65***

Chapter 3. Long Lived $[Ir(tbudqp)(ppy)X]^+$ Photosensitizers 68

3.1 Introduction ***68***

3.2 Experimental ***70***

3.2.1 General *70*

3.2.2 Synthetic Procedures *71*

3.2.3 Computational Modeling *76*

3.2.4 Electrochemical Characterization *77*

3.2.5 Photophysical Characterization *77*

3.2.6 Photocatalytic Hydrogen Generation *78*

3.2.7 Photoredox Catalysis *79*

3.2.8 Singlet Oxygen Generation *80*

3.3 Results and Discussion ***80***

3.3.1 Synthesis *80*

3.3.2 Computational Modeling *83*

3.3.3 UV-Vis Absorption Spectroscopy *85*

3.3.4 Emission Spectroscopy *88*

3.3.5 Electrochemical Characterization *90*

3.3.6 Photocatalytic Hydrogen Evolution *95*

3.3.7 Photoredox Catalysis *97*

3.3.8 Oxygen Quenching and Singlet Oxygen Generation *98*

3.4 Conclusions ***101***

3.5 References ***102***

Chapter 4. Phenanthroline Hemicage Metal Complexes **105**

4.1 Introduction ***105***

4.2 Experimental ***108***

4.2.1 General *108*

4.2.2 Synthetic Procedures *108*

4.2.3 Electrochemical Characterization *119*

4.2.4 Photophysical Characterization *119*

4.3 Results & Discussion ***120***

4.3.1 Synthesis *120*

4.3.2 Absorption & Emission Spectroscopy *125*

4.3.3 Electrochemical Characterization *130*

4.4 Conclusions ***133***

4.5 References ***134***

List of Figures

Figure 1-1. Structures of the cyclometallated Ir(III) dimer and the corresponding cationic mixed-ligand complex. 5

Figure 1-2. HSOMO and LSOMO of $Ru(bpy)_3^{2+}$ (Left) and $[Ir(ppy)_2(bpy)]^+$ (Right) showing pure ^{3}MLCT character in the $Ru(bpy)_3^{2+}$ orbitals and mixed ^{3}ILCT-^{3}MLCT character in the $[Ir(ppy)_2(bpy)]^+$ orbitals. Relevant orbital energies are shown in eV. 5

Figure 1-3. *Tert*-butyl substituted complex published by Slinker *et. al.* used in OLED fabrication.(Chapter 1, ref. 14) 6

Figure 1-4. Ligand structures evaluated in the combinatorial study published by Lowry *et. al.* 7

Figure 1-5: Bar graphs for emission energy (A), luminescence quantum yield (B), and log[excited state lifetime] in nanoseconds (C) for the complexes $[Ir(C\hat{}N)_2(L\hat{}L)]^+$. For all graphs, (C^N) is enumerated as (1) ppy, (2) dtbppy, (3) bhq, (4) thpy, (5) Fmppy, (6) Clmppy, (7) Brmppy, (8) MeOmppy, (9) Phmppy, and (10) Hmppy; (L^L) is indicated as (a) dppz, (b) dppe, (c) Me4-phen, (d) 5-MePhen, (e) 4-MePhen, (f) phen, (g) 5,5'-dmbpy, (h) 4,4'-dmbpy, (i) 4,4'-dtbbpy, (j) bpy. Reprinted with permission from Chapter 1, ref 15. Copyright American Chemical Society 2004. 7

Figure 1-6. Equations and energies for total water splitting into hydrogen and oxygen. ... 9

Figure 1-7. Reductive and oxidative quenching mechanisms for homogenous, photocatalytic generation of hydrogen..... 10

Figure 1-8: Effects of different sacrificial donors and solvents on water photoreduction catalysis with $[Rh(dtbbpy)_3]^{3+}$ as catalyst and $[Ir(Fmppy)_2(dtbbpy)]^+$ as photosensitizer. Reprinted with permission from ref. 21, Chapter 1. Copyright American Chemical Society 2008..... 12

Figure 1-9. Photocatatlyic reactivity of excited Ru(II) and Ir(III) complexes via oxidative or reductive quenching for photoredox catalysis. 14

Figure 1-10. Examples of published photoredox catalysis reactions using an array of Ru(II) and Ir(III) based photosensitizers. **A** (Chapter 1, ref. 25**)**, **B** (Chapter 1, ref. 31), **C** (Chapter 1, ref. 32), **D** (Chapter 1, ref. 33), **E** (Chapter 1, ref. 35), **F** (Chapter 1, ref. 37). Newly formed bonds indicated in red. 16

Figure 1-11. Structures of popular Ru(II) and Ir(III) based photosensitizers for photoredox catalysis..... 16

Figure 1-12. Commercial photoreactor design developed by the Macmillan group. Reprinted with permission from ref. 40, Chapter 1. Copyright American Chemical Society 2017..... 18

Figure 1-13. Side illuminating photoreactor design developed by the Bernhard group. Reprinted with permission from Chapter 1, ref. 41 . Copyright American Chemical Society 2013..... 18

Figure 1-14. Comparison of batch versus flow yields of the visible light initiated radical Smiles rearrangement. (Chapter 1, ref. 42)..... 19

Figure 1-15. Organic dyes used in photochemical singlet oxygen generation. 21

Figure 1-16. Transition metal photosensitizers for photochemical generation of singlet oxygen.. 22

Figure 2-1. ESI-MS Analysis of photocatatlytic hydrogen generation reactions in MeCN before (A) and after (B) irradiation. Adapted from ref. 2, Chapter 2. with permission. Copyright Wiley 2007. (C) Effect of solvent coordination on TON for photocatalytic hydrogen generation. Reprinted from ref. 3, Chapter 2 with permission. Copyright American Chemical Society 2009. 27

Figure 2-2. Photocatalytic H_2 evolution (solid lines, right axis) and rate of H_2 evolution (dotted lines, left axis) from $[Ir(phbpy)_2]^+$ (red) and $[Ir(ppy)_2(bpy)]^+$ (black) in 4:1 acetonitrile/water. Adapted from ref. 4, Chapter 2 with permission. Copyright 2009 American Chemical Society. 28

Figure 2-3. Cationic, bis-terdentate Ir(III) complexes which have previously been reported by Campagna *et. al*. $[Ir(N^N^C)_2]^+$, (ref. 5, Chapter 2) Williams *et. al*. $[Ir(N^C^N)(N^N^C)]^+$, (Chapter 2, ref. 6) and Scandola *et. al*. $[Ir(C^N^C)(N^N^N)]^+$. (Chapter 2, ref. 7,8)..... 28

Figure 2-4. $[Ir(tpy)(ppy)Cl]^+$ based photocatalysts investigated by Ishitani et. al. (Chapter 1, ref. 9) for photocatalytic CO_2 reduction. Turnover numbers for CO after 300 min in MeCN are provided for each complex.. 29

Figure 2-5. Singlet, ground state frontier orbitals of $[Ir(tpy)(ppy)Cl]^+$. Obtained with Gaussian '09 (B3LYP/LANL2DZ). Adapted with permission from ref. 10, Chapter 2. Copyright 2014 American Chemical Society. 30

Figure 2-6. First Generation "Push-Pull" Complex with corresponding photophysical properties as reported by Chirdon et. al. (Chapter 2, ref. 10) 30

Figure 2-7. C-F insertion reaction analyses. ^{19}F (A) and ESI-MS (B) of reaction of **1a** with 2,4-dFmppy along with ^{19}F (C) and ESI-MS (D) of reaction of **1a** with 2-Fmppy.. 45

Figure 2-8. Singlet and triplet frontier orbitals of **2c** (left) and **3c** (right) from Gaussian '09 DFT Calculations. Reduction in LUMO metal character, HSOMO metal character, and LSOMO metal character is observed when going from monofluorinated chloride complex **2c** to perfluorinated cyanide complex **3c**. Transition from HSOMO to LSOMO is a mixed MLCT/ILCT for **2c**, whereas in **3c** it is primarily ILCT. Reprinted from ref. 1, Chapter 2 with permission. Copyright 2016 American Chemical Society. 47

Figure 2-9. UV-vis absorption spectra for **2b** (solid black), **2f** (solid orange), and **3c** (dashed blue). Spectra were collected in MeCN (10 micromolar) at room temperature. The region from 325 nm to 550 nm is enlarged in the inset to show details of the weakest, low energy transitions. Reprinted from ref. 1, Chapter 2 with permission. Copyright 2016 American Chemical Society. 50

Figure 2-10. Experimental. (solid, colored) and calculated (black dashed) UV-Vis absorption spectra of **2c** (A), **2f** (B), **3c** (C). Calculated spectra were determined using Gaussian '09 TD-DFT calculations and Gaussum software with a fwhm = 4000 cm^{-1}. Oscillator strengths are included as vertical lines. Reprinted from ref. 1, Chapter 2 with permission. Copyright 2016 American Chemical Society..... 50

Figure 2-11. Room temperature emission spectra of degassed 10 μM solutions in acetonitrile. Complexes were excited at 380 nm. Vibrational substructure is visible in the spectra of complexes with predominantly ILCT transitions (**2e**-**2f**, **3a**-**3c**). Reprinted from ref. 1, Chapter 2 with permission. Copyright 2016 American Chemical Society. 52

Figure 2-12. Energy gap law correlation of complexes **2a**-**3c**. Cyan circles indicate complexes with emissions from a mixed MLCT/ILCT. Magenta squares indicate complexes with emissions having higher ILCT character. Differences in excited state character are evident from the vibrational substructure of the luminescence spectra (Figure 2-11) as well as the grouping of these data points. Reprinted from ref. 1, Chapter 2 with permission. Copyright 2016 American Chemical Society..... 53

Figure 2-13. DFT prediction of emission energy using (A) the energy difference between the singlet ground and triplet excited states at their respective optimized geometries or (B) the energy difference between the total energies of singlet and triplet excited states at the optimized triplet geometry. Cyan circles indicate the chloro complexes **2a**-**2f** and magenta circles indicate cyano complexes **3a**-**3c**. Reprinted from ref. 1, Chapter 2 with permission. Copyright 2016 American Chemical Society..... 55

Figure 2-14. Cyclic voltammograms of **2b** (A) and **3a** (B). Roman numerals indicate the unique reductions seen in the complexes. Voltammograms were recorded using argon-degassed 0.10 M tetra-n-butylammonium hexafluorophosphate (acetonitrile) solutions containing 0.5 mM of analyte, at 0.10 V/s with a three-electrode system. All potentials are referenced to SCE using ferrocene as an internal standard (fc/fc^{+} = 0.40 V). (Chapter 2, ref. 28) Adapted from ref. 1, Chapter 2 with permission. Copyright 2016 American Chemical Society. 56

Figure 2-15. Photocatalytic hydrogen evolution traces of complexes **2a**-**3c**. Quantities of hydrogen evolved are noted along with the TON of the Ir(III) photosensitizers. Figure produced by Isaac Mills and reprinted from ref. 1, Chapter 2 with permission. Copyright 2016 American Chemical Society. 60

Figure 2-16. Mechanistic similarities between decarboxylative fluorination (proposed by Ventre et. al. (Chapter 2, ref. 34)) and photocatalytic hydrogen evolution (proposed by Tinker et. al. (Chapter 2, ref. 2). 61

Figure 2-17. CO_2 evolution traces using **2b** with diphenylacetic acid at varying catalyst concentrations. 0.1 mol % (black), 0.05 mol % (orange), 0.025 mol % (blue), 0.0125 mol % (green), 0.010 mol % (yellow). Reprinted from ref. 1, Chapter 2 with permission. Copyright 2016 American Chemical Society. 63

Figure 3-1. Structure and photophysical properties of $[Ir(Mebip)(ppy)Cl]^+$ generated by Obara *et. al*. (Chapter 3, ref. 7) 68

Figure 3-2. Ru(II) polypyridyl complexes and their photophysical properties. (Chapter 3, ref. 9,11) 70

Figure 3-3. Singlet frontier orbital diagram of **2a**. Orbitals were calculated using Gaussian ’09 DFT (B3LYP/LANL2DZ). 84

Figure 3-4. Singlet frontier orbital diagram of **3d**. Orbitals were calculated using Gaussian ’09 DFT (B3LYP/LANL2DZ). 84

Figure 3-5. UV-Vis absorption spectra of **2a**, **2d**, **3a**, and **3d**. The portion of the spectrum from 350 nm to 500 nm is enlarged in the inset to show details of the weaker transitions. All spectra were collected at room temperature using 10 μM solutions. 87

Figure 3-6. Experimental (solid, colored) and calcuated (black dashed) UV-Vis absorption spectra of 2a, 2d, 3a, and 3d. Calculated spectra were determined using Gaussian '09 TD-DFT calculations and Gaussum software with a fwhm = 4000 cm^{-1}. Oscillator strengths are included as vertical lines. 87

Figure 3-7. Room temperature emission spectra of degassed 10 μM solutions of **2a**-**3d** in acetonitrile. Complexes were excited at 380 nm. 89

Figure 3-8. Cyclic voltammograms of **2d** and **3d**. Voltammograms were recorded using argon-degassed 0.10 M tetra-n-butylammonium hexafluorophosphate (acetonitrile) solutions containing 0.5 mM of analyte, at 0.10 V/s with a three-electrode system. All potentials are referenced to SCE using ferrocene as an internal standard (fc/fc^+ = 0.40 V). (Chapter 3, ref. 21) 93

Figure 3-9. Photocatalytic hydrogen evolution traces of **2a**-**3d**. Quantities of hydrogen evolved are noted along with the TON of the Ir(III) photosensitizers. 96

Figure 3-10. UV-Vis spectral changes in the photooxidation of DHN to Juglone using **2a** as the photosensitizer, with illumination using blue LEDs..... 101

Figure 4-1 Abundance (expressed as atoms of element per 106 atoms of Si) of chemical elements in the Earth's upper crust as a function of atomic number. Reprinted with permission from ref. 1, Chapter 4. Copyright 2014 The Royal Society of Chemistry. .. 105

Figure 4-2 External quantum efficiency of a $[Ru(bpy)_3](PF_6)_2$ device as a function of time. Reprinted with permission from ref 3, Chapter 4. Copyright 2002 American Chemical Society. 106

Figure 4-3 Ligand dissociation mechanism of $[Ru(bpy)_3]^{2+}$..... 107

Figure 4-4 Normalized emission and UV-Vis absorption spectra of Ru(II) complexes. Spectra were obtained using argon-degassed 25 μM solutions in MeCN at room temperature. 127

Figure 4-5 Normalized emission and UV-Vis absorption spectra of Zn(II) complexes. Spectra were obtained using argon-degassed 25 μM solutions in MeCN at room temperature. 128

Figure 4-6 Emission quenching of Zn(II) complexes by oxygen. 129

Figure 4-7 UV-Vis UV-Vis absorption spectra of Fe(II) complexes. Spectra were obtained using argon-degassed 25 μM solutions in MeCN at room temperature..... 130

Figure 4-8 Cyclic voltammograms of $[Fe(\mathbf{2})_3]^{2+}$ (A) and $[Fe(\mathbf{1})]^{2+}$ (B). Roman numerals indicate the different reductions observed. Voltammograms were recorded with argon-degassed acetonitrile solutions containing 0.10 M tetra-n-butylammonium hexafluorophosphate as the electrolyte and 0.5 mM of analyte. Scans recorded at 0.10 V/s with a three-electrode system. All potentials are referenced to SCE using ferrocene as an internal standard ($fc/fc^+ = 0.40$ V). (Chapter 4, ref. 17) 131

Figure 4-9 Cyclic voltammograms of $[Zn(\mathbf{2})_3]^{2+}$ (A) and $[Zn(\mathbf{1})]^{2+}$ (B). Roman numerals indicate the different reductions observed. Voltammograms were recorded with argon-degassed acetonitrile solutions containing 0.10 M tetra-n-butylammonium hexafluorophosphate as the electrolyte and 0.5 mM of analyte. Scans recorded at 0.10 V/s with a three-electrode system. All potentials are referenced to SCE using ferrocene as an internal standard ($fc/fc^+ = 0.40$ V). (Chapter 4, ref. 17) 132

Figure 4-10 Cyclic voltammogram of $[Ru(\mathbf{2})_3]^{2+}$. Roman numerals indicate the different reductions observed. Voltammogram was recorded with an argon-degassed 0.10 M tetra-n-butylammonium hexafluorophosphate (acetonitrile) solution containing 0.5 mM of analyte, at 0.10 V/s with a three-electrode system. All potentials are referenced to SCE using ferrocene as an internal standard ($fc/fc^+ = 0.40$ V). (Chapter 1, ref. 17) 133

List of Schemes

Scheme 2-1. Synthetic Pathways and Labels of Ir(III) Complexes. Isolated yields in parentheses. Reaction conditions as follows: a) mppy ligand, ethylene glycol, argon atmosphere, 182 ^{o}C, overnight. Adapted with permission from Chapter 2, ref 1. Copyright 2016 American Chemical Society. 42

Scheme 2-2. Chloride-Cyanide Exchange of Ir(III) Complexes. Reprinted with permission from ref 1. Reaction conditions as follows: a) mppy ligand, ethylene glycol, argon atmosphere, 182 ^{o}C, overnight. b) KCN (aq), ethylene glycol, argon atmosphere, 90 ^{o}C, 2 h. Reprinted from Chapter 2, ref. 1 with permission.Copyright 2016 American Chemical Society. 43

Scheme 2-3. Synthetic pathways for fluorinated phenylpyridine ligands. Reaction conditions as follows: a) NH_4OAc, MeOH, 65 ^{o}C overnight. b) K_3PO_4, 1,10-phenanthroline, CuI, DMF/Xylenes, overnight. 43

Scheme 2-4. Syntheses of **2a** and **2b** using C-F and C-H activation under identical reaction conditions. Isolated yields in parentheses. Note: The C-F activation products are the major product of the reactions, with trace amounts of the C-H products being detected by ^{19}F NMR and ESI-MS analysis of the crude reaction mixtures. Reprinted from Chapter 2, ref. 1 with permission. Copyright 2016 American Chemical Society. 46

Scheme 2-5. Decarboxylative Fluorination of Carboxylic Acids and structure of $[Ir(dF(CF_3)ppy)_2(dtbbpy)]^+$. 61

Scheme 3-1. Synthesis of tbudqp. Isolated yields in parentheses. 81

Scheme 3-2. Synthesis of Ir(III) complexes **1a**, **2a**-**2d**. Isolated yields in parentheses. Reaction conditions as follows: a) $IrCl_3 \bullet 4H_2O$, ethylene glycol, argon atmosphere 170 ^{o}C, 22 min. b) mppy ligand, ethylene glycol, argon atmosphere, 183 ^{o}C, overnight. 82

Scheme 3-3. Chloride-Cyanide Exchange of Ir(III) Complexes. Isolated yields in parentheses. Reaction conditions as follows: a) mppy ligand, ethylene glycol, argon atmosphere, 183 ^{o}C, overnight. b) KCN (aq), ethylene glycol, argon atmosphere, 90 ^{o}C, 2 hr. 82

Scheme 3-4. Decarboxylative Fluorination of Carboxylic Acids and the structure of $[Ir(dF(CF_3)ppy)_2(dtbbpy)]^+$. 98

Scheme 3-5. Photooxidation of DHN to Juglone. 100

Scheme 4-1. Attempted alkylations of 3-methylphenanthrolines towards a phenanthroline hemicaging ligand. 121

Scheme 4-2. Attempted synthesis of phenanthroline hemicage ligand via Sonogashira Coupling and Alkyne Hydrogenation. 122
Scheme 4-3. Synthesis of phenanthroline hemicaging ligand **1** and its corresponding metal complexes. Reaction conditions as follows: a) S_2Cl_2, Chlorobutane, Pyridine, Br_2, 95 ^oC, 5 h. b) Fe, AcOH, EtOH, H_2O, HCl, 120 ^oC, 2 h. c) H_2O, H_2SO_4, NaI, 110 ^oC, 5 h. d) $Pd(PPh_3)_4$, CuI, DMF, 120 ^oC, 24 h. e) THF, H_2O, LiOH, Pd/C, H_2, overnight. f) $M(BF_4)_2$, EtOH, 95 ^oC, 4-24 h. Isolated yields in parentheses. 123

Scheme 4-4. Synthesis of phenanthroline ligand **2** and its corresponding metal complexes. Reaction conditions as follows: a) H_2O, H_2SO_4, NaI, 110 ^oC, 24 h b) $Zn(BF_4)_2$/$Fe(BF_4)_2$, MeOH, H_2O, RT, 1 h or $RuCl_3$, ethylene glycol, MW, 10 min. Isolated yields in parentheses..... 124

Scheme 4-5. Synthesis of mesityl capped phenanthroline hemicaging ligand **3** and its corresponding Zn(II) complex. Reaction conditions as follows: a) $Pd(PPh_3)_4$, CuI, DMF, 120 ^oC, 24 h. b) THF, H_2O, LiOH, Pd/C, H_2, overnight. c) $Zn(BF_4)_2$, EtOH, 95 ^oC, 24 h. Isolated yields in parentheses..... 125

List of Tables

Table 1-1. Electrochemical data for select bis-cyclometallated Ir(III) complexes from work by Goldsmith et. al. (Chapter 1, ref. 16) All values are reported with respect to SCE. 8

Table 2-1. Photophysical Properties of "Push-Pull" Ir(III) Complexes. 51

Table 2-2. Electrochemical Properties of "Push-Pull" Complexes. 56

Table 2-3. Calculated Excited State Redox Potentials of "Push-Pull Complexes". 58

Table 2-4. Photosensitizer and Substrate Studies of the Decarboxylative Fluorination Reaction. Yields determined by ^{19}F NMR with C_6F_6 as an internal standard. 62

Table 3-1. Photophysical Properties of tbudqp Ir(III) Complexes. Samples were analyzed as 10 μM solutions in acetonitrile after purging and blanketing with argon. 88

Table 3-2. Electrochemical Properties of tbudqp Complexes. ΔE values reported in mV for reductions that are fully reversible. 94

Table 3-3. Calculated Excited State Redox Potentials of tbudqp Complexes. 95

Table 3-4. Photosensitizer and substrate studies of the Decarboxylative Fluorination Reaction. Yields determined by ^{19}F NMR after 18 hours of illumination with C_6F_6 as an internal standard. 98

Table 3-5. Emission quenching of Ir(III) complexes by O_2, measured in MeCN at room temperature. 99

Table 3-6. Photooxidation of DHN related parameters of Ir(III) complexes, measured in MeCN/isopropanol mixed solvent, at room temperature. 101

Table 4-1 Photophysical properties of Ru(II) complexes. 126

Table 4-2 Photophysical properties of Zn(II) complexes. 128

Table 4-3. Electrochemical Properties of Fe(II) complexes and $[Fe(bpy)_3]^{2+}$.(Chapter 4, ref. 35) 131

Table 4-4 Electrochemical Properties of Zn(II) complexes and $[Zn(bpy)_3]^{2+}$. (Chapter 4, ref. 36) Overlap of $Zn^{2+/0}$ plating onto electrode and complex reduction. 132

Table 4-5 Electrochemical Properties of Ru(II) complex $[Ru(\mathbf{2})_3]^{2+}$, $[Ru(bpy)_3]^{2+}$, and $[Ru(phen)_3]^{2+}$.(Chapter 4, ref. 37) 133

List of Abbreviations

ACN	acetonitrile
bpy	2,2’-bipyridine
bqp	2,6-bi(quinolin-8-yl)pyridine
DHN	1,5-dihydroxynaphthalene
dtbubpy	4,4'-di-*tert*-butyl-2,2'-bipyridine
dtbbpy	4,4'-di-*tert*-butyl-2,2'-bipyridine
ESI-MS	electrospray ionization mass spectrometry
HOMO	highest occupied molecular orbital
HSOMO	highest singly occupied molecular orbital
ILCT	intraligand charge transfer
LED	light emitting diode
LSOMO	lowest singly occupied molecular orbital
LUMO	lowest unoccupied molecular orbital
Mebip	bis(N-methyl-2-benzimidazolyl)pyridine
MeCN	acetonitrile
MLCT	metal to ligand charge transfer
mppy	5-methyl-2-phenylpyridine
pbpy	6-(pyridin-2-ylmethyl)-2,2'-bipyridine
phbpy	6-phenyl-2,2'-bipyridine
phen	1,10-phenanthroline
ppy	2-phenylpyridine
PS	photosensitizer
SCE	saturated calomel electrode
SR	sacrificial reductant
tbudqp	8,8'-(4-(*tert*-butyl)pyridine-2,6-diyl)diquinoline
TD-DFT	time-dependent density functional theory
TEA	triethylamine
TEOA	triethanolamine
THF	Tetrahydrofuran
TON	Turnover Number
tpy	2,2':6',2''-terpyridine
ttbutpy	4,4',4''-tri-*tert*-butyl-2,2':6',2''-terpyridine
WOC	Water Oxidation Catalyst
WRC	Water Reducing Catalyst

Chapter 1. Harnessing the Power of Light

1.1 Current Energy Demand

The United States has consistently been using carbonaceous fuels including oil, natural gas, and coal as their primary energy sources.[1] In 2016 alone, nearly 80% of the energy demand was met with oil, natural gas, and coal, with sustainable energy sources like wind and solar only accounting for 6%.[1] While it is projected that usage of fuels such as coal will see decreases due to costs of extraction and processing, petroleum and natural gas will continue to overtake them given their ease of access and abundance within the continental US. While the combustion of such fuels for energy is in fact improved in terms of emission of greenhouse gases compared to coal, it cannot be denied that their continued use will only accelerate the addition of greenhouse gases into the atmosphere, which has been continuing to rise due to anthropogenic involvement.[2] While short term needs for energy, employment, and capital are viewed by some as issues of greater importance, in reality they need to be viewed second to the long term consequences of continued actions that are being proven to be damaging to our current climate and compromising to our future.

Numerous sustainable alternatives are already being implemented including wind, hydroelectric, and solar. It cannot be denied that implementation of these new sources of energy not only bring about sustainable sources of energy, but development of areas of new research, new employment opportunities, and the ability to establish a greater degree of energy independence. While many argue against the "aesthetics" of large wind turbines, the high cost of infrastructure for hydroelectric power plants, or the intermittency of the sun for solar energy, optimizations and improvements have already

been taking place thanks to academic and industrial research efforts.[3–5] Continued support and investment into these sources are necessary to drive costs down, and continue to make them appealing, sustainable replacements for our energy needs in the hope of stalling further environmental damage.

This thesis describes efforts towards harnessing solar energy not only as a sustainable means to fulfill our energy needs through the splitting of water, but also a means to drive chemical reactions that are relevant to industrial scale synthesis. The first two chapters of this work is centered on the development of stable, efficient, and tunable Ir(III) based photosensitizers. Improvements in a number of key properties were meant to improve the usage of Ir based complexes and compensate for their rising costs compared to other earth abundant metals. The versatility of such photosensitizers for a wide variety of conditions allow for them to be used in numerous solar energy conversion applications. The final chapter is focused on efforts to improve the structures of photosensitizers from more earth-abundant metals including Zn and Fe, which unfortunately suffer from stability and photochemical issues that preclude their use as more cost-effective replacements for expensive metals like Ir.

1.2 Light Energy Use and Storage

1.2.1 The Ideal Solar Civilization

As early as 1912, chemists have been advancing towards a major transition in the sourcing of global energy needs from coal, oil, natural gas and other carbonaceous fuels to renewables such as solar energy. In a paper published in 1912 by the late Giacomo Luigi Ciamician, he makes the case for an ideal civilization where renewable energy, specifically solar energy, could not only remove global dependence on carbonaceous

fuels, but also rebalance the energy climates such that both poor and rich countries alike can have access to abundant, clean energy.[6]

> *"On the arid lands, there will spring up industrial colonies without smoke and without smokestacks; forests of glass tubes will extend over the plains and glass buildings will rise everywhere; inside of these will take place the photochemical processes that hitherto have been the guarded secret of the plants, but that will have been mastered by human industry which will know how to make them bear even more abundant fruit than nature, for nature is not in a hurry and mankind is. And if in a distant future the supply of coal becomes completely exhausted, civilization will not be checked by that, for life and civilization will continue as long as the sun shines!"* [6]

By making use of the vast photochemical processes available for energy, synthesis, manufacturing, and transportation it can be envisioned that photochemistry can be a means towards improving the global energy climate. This transition to photochemical energy can hopefully stave off the consequences that stem from the combustion of carbonaceous fuels, and allow for more sustainable energy landscape that can extend the viability of what remains of Earth's resources for future generations. For photochemists, development of molecules that are responsible for harnessing this energy into a usable or storable form is therefore of paramount importance.

1.2.2 The Case for Ir(III) Photosensitizers

The use of photoactive, transition metal complexes has been an area of great interest, especially for a number of photochemical applications. Complexes based on the $[Ru(bpy)_3]^{2+}$ structure have garnered interest due to the modest photoreducing and strong photooxidizing abilities, long-lived triplet excited states, and strong spin-orbit couplings.[7] Unfortunately, the use of this complex in industrially relevant applications, such as OLED fabrication or as a photosensitizer have been hampered due to the lack of

tunability of the complexes photophysical and electrochemical properties, which arises from a purely ^{3}MLCT transition in the excited state that is limited by a low-lying ^{3}MC state. Nevertheless, the readily-synthesized complex was extensively studied and its attractive properties were further enhanced by the synthesis of the corresponding $[Ir(bpy)_3]^{3+}$ and $[Ir(tpy)_2]^{3+}$ complexes. The complexes were potent photooxidants, but they still lacked a means of tunability. Furthermore, they were difficult to synthesize as the temperatures required for the reactions often result in mixtures of cyclometallated and non-cyclometallated complexes.

One major advancement in improving the photophysical properties of the Ir(III) complexes was achieved through deliberate cyclometallation of the Ir(III) center by replacing the bipyridine ligand with a phenylpyridine. This generated the dichloro-bridged $[Ir(ppy)_2Cl]_2$ dimer (Figure 1-1).[8,9] Color and redox tunability for the complexes was subsequently observed with the synthesis of the mixed-ligand $[Ir(ppy)_2(bpy)]PF_6$ complex (Figure 1-1) and its derivatives.[10] Computational analysis of the excited states of the mixed-ligand complexes indicated that the emissions were the result of mixed ^{3}ILCT-^{3}MLCT transitions, with strong partitioning of the HSOMO on the bipyridine and the LSOMO on the phenylpyridine ligands (Figure 1-2).[11,12] The result is a new set of complexes which possess substantial metal character in their excited states, strong spin-orbit coupling, and partitioned electronic structures that allow for highly tunable photoexcited states. Furthermore, the triplet states of the complexes can be both powerfully oxidizing *and* reducing allowing the complexes to be tuned to suit a variety of different photochemical processes involving electron transfers.

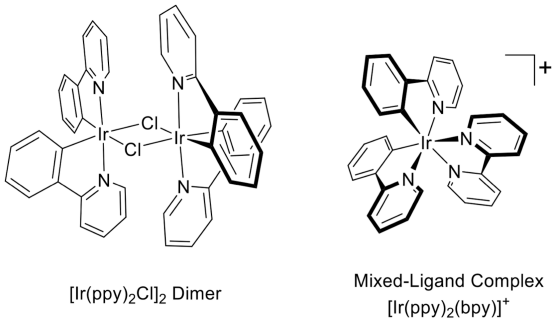

Figure 1-1. Structures of the cyclometallated Ir(III) dimer and the corresponding cationic mixed-ligand complex.

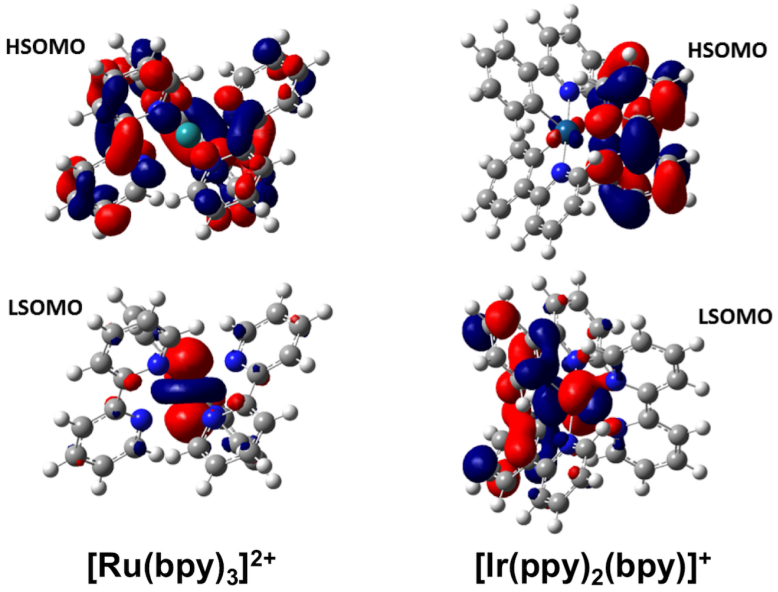

Figure 1-2. HSOMO and LSOMO of $Ru(bpy)_3^{2+}$ (Left) and $[Ir(ppy)_2(bpy)]^+$ (Right) showing pure ^{3}MLCT character in the $Ru(bpy)_3^{2+}$ orbitals and mixed ^{3}ILCT-^{3}MLCT character in the $[Ir(ppy)_2(bpy)]^+$ orbitals.

One of the first applications of this family of luminophores was in work by Kenneth Lo, who first used the complexes as luminescent probes for biological imaging. Biotin was attached to the bipyridine ligand, which was not found to disturb the luminescence properties of the complexes.[13] Variation of the cyclometallating ligands, however, produced a modest variation in the emission maxima of the complexes, with complexes emitting between 554 – 587 nm in degassed acetonitrile at room temperature.

Similarly, work in the Bernhard Lab was investigating the cationic bis-cyclometallated iridium complexes in OLEDs. Work by Slinker *et. al*., published a vastly-improved variant of the traditional $[Ir(ppy)_2(bpy)]^+$ complex, where the 4 and 4' positions of the bipyridine ligand were substituted with *tert*-butyl groups (Figure 1-3). The steric bulk of the groups led to a three-fold increase in the luminescence quantum yield along with a nearly two-fold extension of the excited state lifetime. The complex was also an efficient luminophore in a single layer OLED with a light output of 10 Lm/W and a brightness at 300 cd/m^2, both at 3 V.[14]

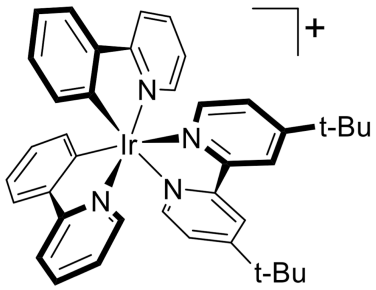

Figure 1-3. *Tert*-butyl substituted complex published by Slinker *et. al.* used in OLED fabrication.[14]

Subsequently, Lowry *et. al.* synthesized 76 new bis-cyclometallated Ir(III) complexes via a combinatorial approach to probe the limits of synthetic tunability. Over 100 complexes were synthesized, including previously published controls, via a step-wise synthesis starting with the dimer with one of 10 cyclometallating ligands followed by cleavage with one of 10 neutral bidentate ligands (Figure 1-4). The controls were in excellent agreement with previous results, while the new complexes proved these complexes' emission maxima, excited state lifetime, and quantum yield can all be tuned by variation of the ligands (Figure 1-5).[15]

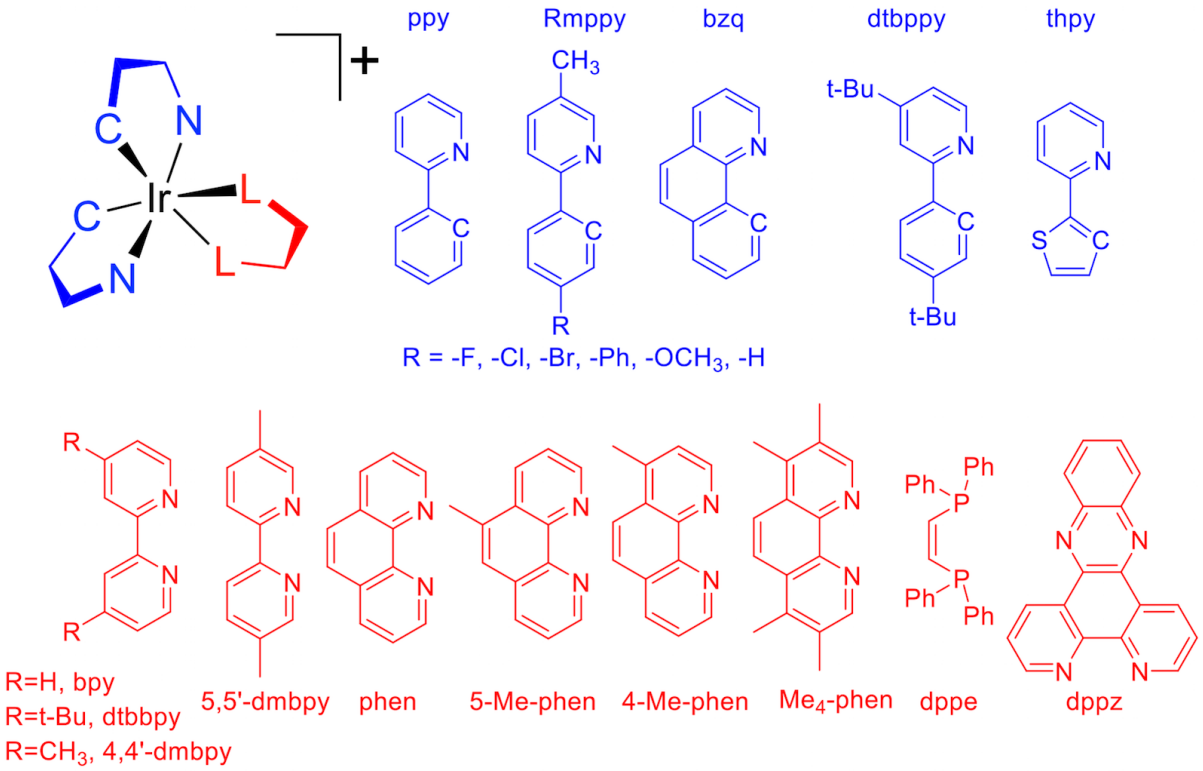

Figure 1-4. Ligand structures evaluated in the combinatorial study published by Lowry *et. al.*

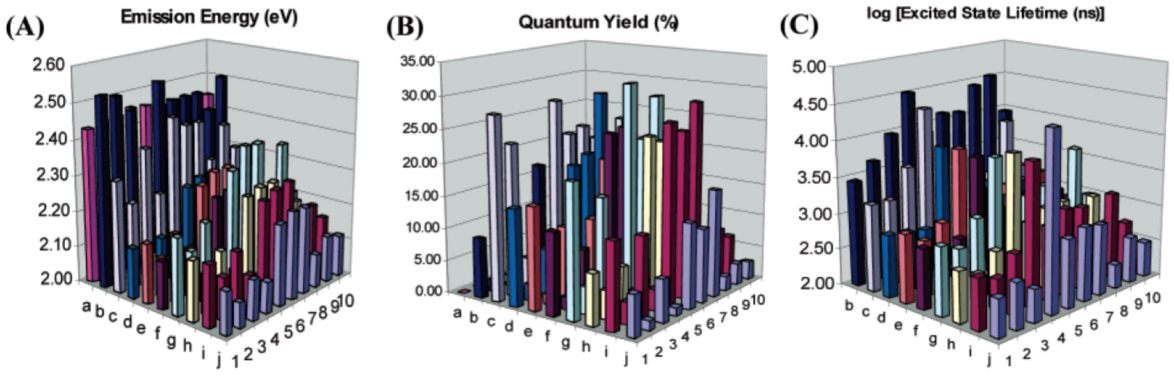

Figure 1-5: Bar graphs for emission energy (A), luminescence quantum yield (B), and log[excited state lifetime] in nanoseconds (C) for the complexes $[Ir(C^N)_2(L^L)]^+$. For all graphs, (C^N) is enumerated as (1) ppy, (2) dtbppy, (3) bhq, (4) thpy, (5) Fmppy, (6) Clmppy, (7) Brmppy, (8) MeOmppy, (9) Phmppy, and (10) Hmppy; (L^L) is indicated as (a) dppz, (b) dppe, (c) Me4-phen, (d) 5-MePhen, (e) 4-MePhen, (f) phen, (g) 5,5'-dmbpy, (h) 4,4'-dmbpy, (i) 4,4'-dtbbpy, (j) bpy. Reprinted with permission from ref [15]. Copyright American Chemical Society 2004.

To utilize the partitioning of the frontier orbitals to separate ligands, the oxidation and reduction potentials were directly tuned through ligand modification as well. The basic strategy follows that with the HOMO and LSOMO reside on the cyclometallating ligand, and may be stabilized by the inclusion of electron-withdrawing groups to increase the oxidation potential of the complex. The LUMO and HSOMO can be tuned by incorporation of electron-donating groups to the diimine ligand. This produces a destabilizing effect on the orbitals gives a less negative 1st reduction. Modification of the cyclometallating ligand was found to produce the more dramatic tuning effects compared to modification of the diimine ligand (Table 1-1).[16]

Table 1-1. Electrochemical data for select bis-cyclometallated Ir(III) complexes from work by Goldsmith et. al.[16] All values are reported with respect to SCE.

Photosensitizer	**$E^{0'}$ $M^{n+}/M^{(n+1)+b}$ (V vs SCE)**	**ΔE_p (mV)**	**$E^{0'}$ L/L^- (V vs SCE)**	**ΔE_p (mV)**
$[Ir(ppy)_2(bpy)]^+$	+1.25	65	-1.42	70
$[Ir(ppy)_2(phen)]^+$	+1.24	65	-1.42	80
$[Ir(ppy)_2(dphphen)]^+$	+1.23	75	-1.38	70
$[Ir(Fmppy)_2(bpy)]^+$	+1.38	75	-1.39	60
$[Ir(Fmppy)_2(phen)]^+$	+1.36	60	-1.39	80
$[Ir(Fmppy)_2(dphphen)]^+$	+1.36	75	-1.35	70

1.2.3 Photocatalytic Hydrogen Generation from Water

Given the success in tuning of the Ir(III) photosensitizers, their application into solar fuel generation, specifically hydrogen generation from water, logically follows. The use of water as a feedstock is considerably attractive because not only is it an abundant, benign fuel, but the emissions from combustion of the hydrogen and oxygen products of water splitting only yield water and does not contribute any additional greenhouse gases to the atmosphere. In addition, hydrogen can be readily used in a number of contemporary technologies including fuel-cell based vehicles. When produced through

photocatalytic means, the infrastructure necessary to generate hydrogen as a fuel is dramatically smaller and more energy efficient when compared to current processes including steam reforming.

A number of possible conditions and components exist that require a highly tunable, optimized photosensitizer to best work with the components of the system. While ideal conditions involve the total splitting of water into hydrogen and oxygen photocatalytically, the conditions required for the water oxidation component are highly detrimental to the integrity of the components involved. Furthermore, the energies required to drive the four electron, four proton transfer reaction (Figure 1-6) photochemically are well beyond that of traditional photosensitizers (E_{ox} ~ 1 V vs SCE) which typically only transfer a single electron at a time, therefore leaving the water oxidation reaction to generally be studied as a dark reaction. [17,18]

$2H_2O \longrightarrow O_2 + 4H^+ + 4e^-$ $\quad E^o = -1.23$ V vs NHE

$4H^+ + 4e^- \longrightarrow 2H_2$ $\quad E^o = 0.00$ V vs NHE

$2H_2O \longrightarrow O_2 + 2H_2$ $\quad \Delta E^o = -1.23$ V

$\Delta G^o = 475$ kJ, 237 kJ/mol H_2O

Figure 1-6. Equations and energies for total water splitting into hydrogen and oxygen.

Generally, in homogenous systems for the hydrogen generation reaction, there are three key components involved: the photosensitizer (PS), water reduction catalyst (WRC), and the sacrificial reductant (SR). The purpose of the SR is to mimic the oxidation half reaction of water splitting. As shown in Figure 1-7, these components can interact through either a reductive quenching mechanism or an oxidative quenching mechanism. Reductive quenching involves the photoexcited PS being reduced by the SR prior to donating its electron to the WRC. In contrast, an oxidative quenching mechanism

involves donation of an electron from the photoexcited PS to the WRC, and then returning to its ground state via accepting an electron from the SR. To better determine the efficiency of the reaction, quantification of the hydrogen generated can be achieved through the use of specific hydrogen sensors, mass spectrometry, or gas chromatography. To develop a precise mechanism of a given set of components, quenching studies can be used to determine whether quenching by the WRC or the SR is faster, thereby indicating the type of mechanism. Electrochemistry can also be used to identify any instabilities in the components, or to probe any possible reaction intermediates.

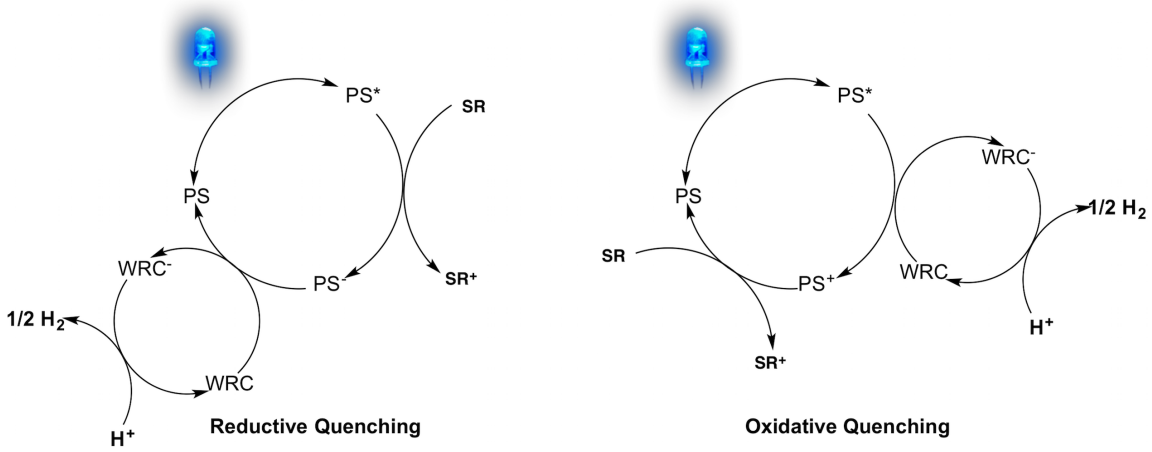

Figure 1-7. Reductive and oxidative quenching mechanisms for homogenous, photocatalytic generation of hydrogen.

With several components involved, optimization for the process in a homogenous system can be easily pursued by tuning each components' properties. Generally, the SR is an affordable, abundant compound that can sufficiently quench the PS and moderate the pH of the solution over the course of the reaction. Common, commercially available SRs include triethylamine (TEA), triethanolamine (TEOA), ascorbate, or EDTA. It's also worth noting that reaction byproducts from the SR can also hinder a reaction,[19] and

therefore evaluation of several different SRs for a particular system is still worth pursuing.

Based on the successes of tuning bis-cyclometallated Ir (III) complexes as luminophores for OLEDs, work also began towards using these complexes to drive the generation of hydrogen from water. Previous systems were able to use $[Ru(bpy)_3]^{2+}$ derivatives as a photosensitizer and $[Co(bpy)_3]^{2+}$ as the water reduction catalyst.[20] Despite the lower molar extinction coefficients of the iridium complexes compared to the ruthenium complexes, the iridium-based photosensitizers achieved much higher turnovers, up to a maximum of 920 compared to 580 for the Ru(II) system.[16] Compared to Ru(II) based complexes, the Ir(III) complexes are up to 20 times more efficient when accounting for the differences in molar absorptivity.

Efforts to further improve upon the photocatalytic water reduction system with the Ir(III) photosensitizers were realized by the replacement of $[Co(bpy)_3]^{2+}$ by K_2PtCl_4 as a catalyst. This catalyst allowed photocatalytic hydrogen generation *via* reductive quenching without the use of an electron relay, simplifying future studies on efficient photosensitizer and catalyst designs. Initially, this system was only capable of 63 PS turnovers with a photon-to-hydrogen conversion efficiency of 26%.[12] Additionally, modified $[Rh(bpy)_3]^{3+}$ complexes were also evaluated for the system.[21] Replacing K_2PtCl_4, which is known to form colloids in situ, with a molecular catalyst allowed a maximum of 5000 PS turnovers. As mentioned before, total optimization for all of the reaction components is necessary, including the sacrificial reductant and reaction co-solvent. These two choices, while at times trivial, must be carefully made as the solvent dictates electron transfer rates between the PS and the catalyst (Figure 1-8). The ligating

power of the solvent can also stabilize or destabilize key intermediates, and the sacrificial reductant plays a vital role in quenching of the excited photosensitizer and prevention of unwanted side reactions.

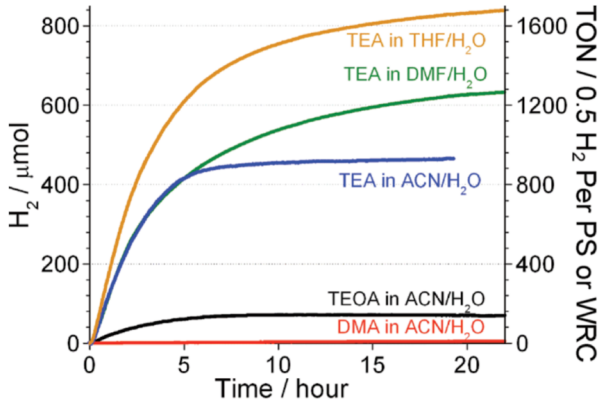

Figure 1-8: Effects of different sacrificial donors and solvents on water photoreduction catalysis with $[Rh(dtbbpy)_3]^{3+}$ as catalyst and $[Ir(Fmppy)_2(dtbbpy)]^{+}$ as photosensitizer. Reprinted with permission from ref [21]. Copyright American Chemical Society 2008.

While major strides have been made in implementing Ir(III) photosensitizers into solar energy based applications such as homogenous photocatalytic hydrogen generation, a number of challenges still remain. The high costs of the precursors needed for the Ir, Pt, and Rh species involved coupled with the inability to recycle most of the catalysts after reaction make scalability of the reactions difficult. In terms of atom economy, a sacrificial reductant is not an efficient component to use and scale up, and should eventually be replaced by the water oxidation reaction. Of course, the dramatic differences in reaction conditions between the two reactions continue to make the processes difficult to unite. In spite of this, the high tunability of the Ir(III) complexes mentioned as photosensitizers continue to make them prime candidates for future explorations into new conditions for photocatalytic hydrogen generation.

1.2.4 Photoredox Catalysis for Organic Transformations

In addition to being an abundant, renewable, and inexpensive source of clean energy, sunlight and light energy in general can also be viewed as an ideal reagent for clean, environmentally friendly chemical synthesis. Nature has already developed means to harness solar energy to synthesize necessary compounds through photosynthesis, which can be viewed as one of the most economical cases of synthesis. It is especially noteworthy given the simplicity of the starting materials and complexity of the reaction products, all from a series of enzymes and photosystems that can efficiently translate light energy into the formation of chemical bonds. Despite the recognition photochemistry has garnered as a route to alternative, sustainable energy, it's utility in synthetic chemistry has been limited up until the past few years.

Most simple organic molecules have weak visible light absorbance and strong absorbances in the ultra-violet region. Unfortunately, UV light is not as abundant in the solar spectrum compared to visible light, and the safe generation of the necessary UV light to drive photochemical reactions requires highly specialized equipment which proves problematic on an industrial scale. It can also be envisioned that high energy UV light also has the potential to promote side reactions and cleavage of valuable C-C bonds that would further complicate the use of an abundant energy source. In order to make use of the major wavelengths in the visible region of the solar energy spectrum, photostable compounds with stronger absorbances in the visible region would be necessary.

The harnessing of solar energy has already benefitted immensely from research into transition metal complexes that have strong absorbances in the visible spectrum. As previously highlighted, Ru(II) and Ir(III) complexes have been thoroughly researched and

designed to be able to absorb visible light and produce an excited state that is a great source of chemical potential energy. The chemical processes involved in the conversion of photochemical energy for organic transformations, much like in the photocatalytic splitting of water (Figure 1-7), rely on the oxidative or reductive quenching of an excited photosensitizer to generate either a strongly oxidizing or reducing species, followed by regeneration of the original species. This process has been heavily studied with $[Ru(bpy)_3]^{2+}$ based complexes, which were the earliest examples of transition metal complexes being used as photosensitizers for organic transformations.[22–28] The respective donor or acceptor molecules involved can gain or lose an electron, respectively, from the excited photosensitizer, and then proceed to terminate with an additional radical species, which may also be formed by the regeneration of the photosensitizer (Figure 1-9). This fundamental principal has governed numerous photoredox catalysis reactions. It was only with further research that substitutions of Ru(II) complexes by Ir(III) complexes were realized given that Ir(III) complexes can also serve to be oxidatively or reductively quenched.

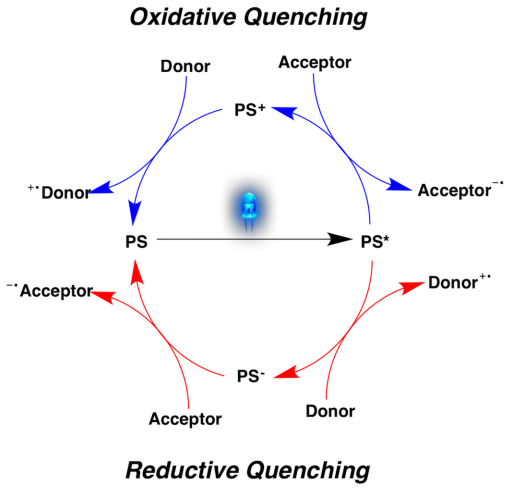

Figure 1-9. Photocatatlyic reactivity of excited Ru(II) and Ir(III) complexes via oxidative or reductive quenching for photoredox catalysis.

Much like photocatalytic water reduction, the choice of photosensitizer can impact the reaction efficiency of photoredox catalysis. Coupled with the diversity of the reactions (Figure 1-10) that can be performed through photoredox catalysis, optimization of the photosensitizers for each new reaction is necessary. In terms of Ru(II) and Ir(III) based photosensitizers, the Macmillan group at Princeton University and the Yoon group at University of Wisconsin-Madison have pioneered the use of a wide variety of complexes (Figure 1-11). The initial studies of photoredox catalysis were conducted using $[Ru(bpy)_3]^{2+}$,[29,30] however in later work, the Yoon group investigated the newer $[Ru(bpz)_3]^{2+}$ complex as a more oxidizing analogue.[31] Meanwhile, the Macmillan group began to transition to the use of Ir(III) photosensitizers given their improved photostability and higher quantum efficiencies compared to Ru(II) based complexes. While initial efforts utilized the simpler $[Ir(ppy)_3]$ structure,[32] the improved tunability of the $[Ir(ppy)_2(bpy)]^+$ based complexes lead to increased usage of $[Ir(ppy)_2(dtbubpy)]^+$ [33] and especially a complex pioneered by the Bernhard group as an OLED luminophore and photosensitizer for water reduction,[34] $[Ir(dF(CF_3)ppy)_2(dtbubpy)]^+$ [35,36], which had the highest quantum efficiency of the series to date. The Macmillan group has also been developing reaction that couple the Ir(III) photosensitizer with a Ni catalyst[37] to facilitate cross-coupling reactions.[38]

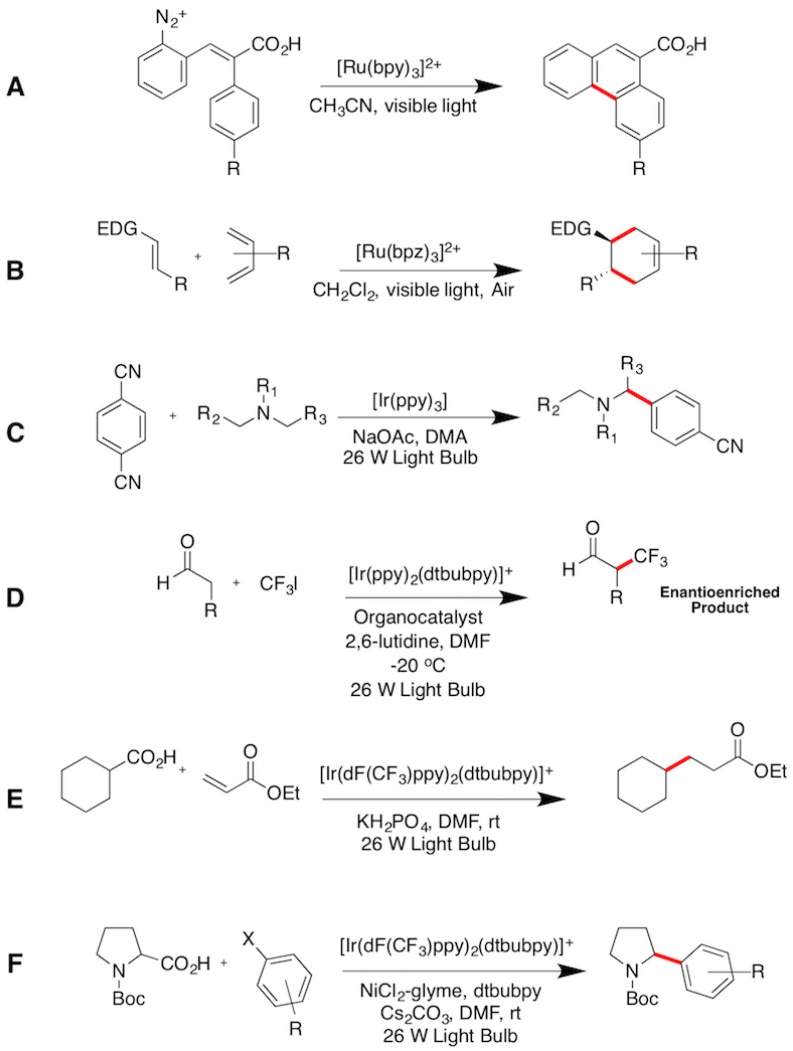

Figure 1-10. Examples of published photoredox catalysis reactions using an array of Ru(II) and Ir(III) based photosensitizers. **A**,[25] **B**,[31] **C**,[32] **D**,[33] **E**,[35] **F**.[37]. Newly formed bonds indicated in red.

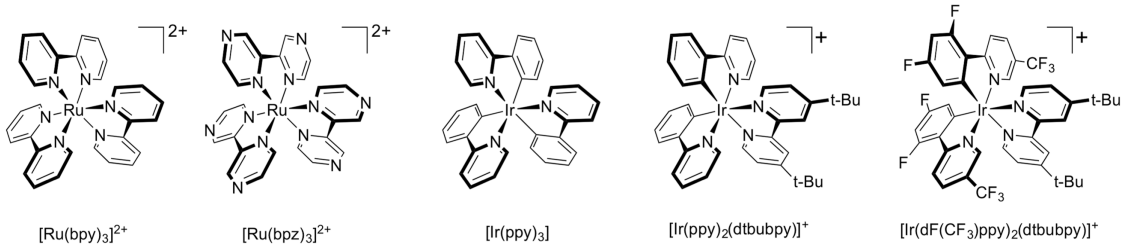

Figure 1-11. Structures of popular Ru(II) and Ir(III) based photosensitizers for photoredox catalysis.

The optimization of the photosensitizer for each reaction relies heavily on the ground and excited state redox potentials of the photosensitizer and how well they overlap with those of the corresponding donor and acceptor species involved in the reactions. While increased photophysical efficiency (higher quantum yields) do improve the photosensitizer performance, this cannot compensate for a complex being too weak of an oxidant or reductant. Further studies have attempted to correlate excited state lifetimes as a measure of efficiency in photoredox,[39] but the findings ultimately corroborated with the idea that reduction and oxidation potentials and tuning of those is the more efficient method to optimizing a photosensitizer for photoredox catalysis.

Given the importance of light as a reagent for photoredox catalysis, appropriate reaction design is key to achieving optimal conversions. Parameters such as light color, intensity, and even distance from the reaction vessel all can drastically influence the efficiency of a reaction. In order to achieve consistently high yields for reactions, the Macmillan group has recently developed a commercialized photoreactor (Figure 1-12).[40] The apparatus ensures intense, uniform light distribution for the reaction, as well as optimal temperature control. The ease of exchanging the light source allows for a variety of visible wavelengths, and even white light, as the energy source to drive the reactions. It is also worth noting that while a commercial photoreactor can standardize future photoredox catalysis, simpler photoreactors[41] can be substituted as well depending on available resources (Figure 1-13) and with careful reporting of the necessary parameters, access to photoredox catalysis can be spread beyond those who can afford such intricate equipment.

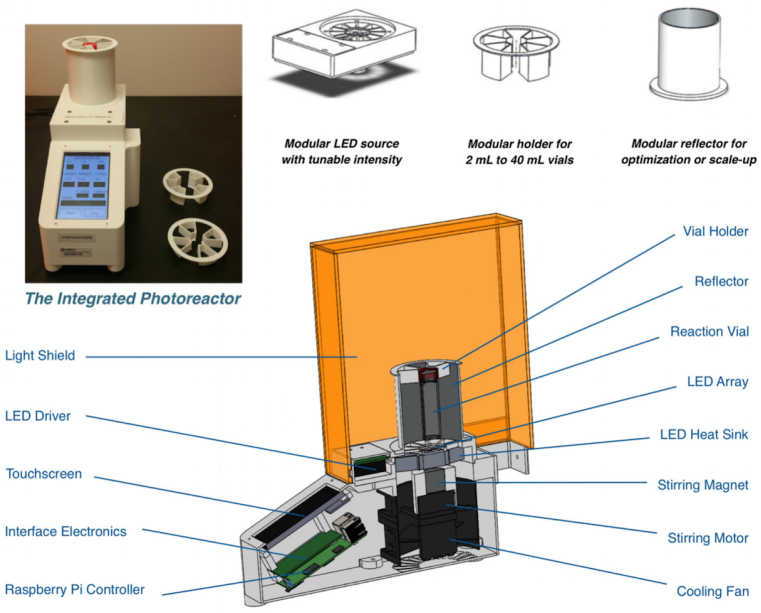

Figure 1-12. Commercial photoreactor design developed by the Macmillan group. Reprinted with permission from ref [40] . Copyright American Chemical Society 2017.

Figure 1-13. Side illuminating photoreactor design developed by the Bernhard group. Reprinted with permission from ref [41] . Copyright American Chemical Society 2013.

Further improvements to photoredox catalysis have also involved translating the process into the more industrially-favored flow reactors. Work by the Stephenson group at University of Michigan- Ann Arbor worked to design and optimize flow reaction

conditions for photoredox reactions (Figure 1-14).[42,43] When compared to batch reactors, the flow reactions give comparable yields, can generate product more steadily, and be performed with significantly less hazards, all of which are highly favorable for an industrial scale synthesis.

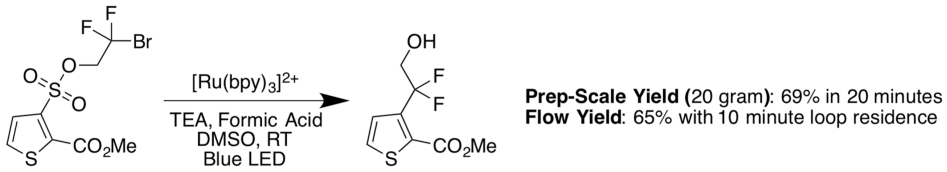

Figure 1-14. Comparison of batch versus flow yields of the visible light initiated radical Smiles rearrangement.[42]

Given the importance of optimizing the photosensitizer for each new photoredox reaction, the high degree of tunability of Ir(III) complexes makes them highly desirable for use. Much like in photocatalytic hydrogen generation however, the cost of the Ir precursors may preclude their use in significantly larger scales. By developing and exploring new photosensitizer structures that would be more stable and efficient, while still maintaining the ability to tune the redox properties, photoredox catalysis can continue to grow as fast as it has in recent years. As highlighted in numerous review articles, photoredox is looking to take full advantage of light energy as a reagent for chemical synthesis.[38,44–49]

1.2.5 Photochemical Generation of Singlet Oxygen

Much like photoredox catalysis, the photogeneration of singlet oxygen aims to utilize readily available energy from light to convert abundant, gaseous oxygen into its singlet state to generate a more oxidizing, electrophilic species. While thermal generation of singlet oxygen is also possible through aromatic endoperoxide species, the yields of singlet oxygen are compromised by the generation of triplet oxygen, as well as other

radical species that interfere with singlet oxygen's ability to react with the corresponding substrates.[50–52] In general, singlet oxygen can be utilized for a whole host of applications including chemical synthesis, wastewater treatment, sanitation, and biological applications including cellular imaging and photodynamic therapy.[53]

The necessary characteristics of a photosensitizer for efficient photochemical generation of singlet oxygen are quite similar to those needed for photoredox catalysis and photocatalytic hydrogen generation, with a few additional criteria. In order to efficiently harness light energy, the photosensitizer needs to be have a high extinction coefficient at the wavelength of excitation, which would ideally be in the visible region given its greater abundance in the solar spectrum. Subsequently, the photosensitizer must possess a triplet state with a longer excited state lifetime (> 1 μs) to ensure that it has ample time to fully relax to the lowest triplet excited state that could subsequently transfer the necessary energy to oxygen to promote it to its singlet state. Finally, the photosensitizer should be able to survive any quenching or reaction with singlet oxygen such that it can repeatedly generate singlet oxygen without being destroyed by it.[54]

While a number of organic photosensitizers including rose bengal, fluorescein, eosin blue, erythrosine b, and methylene blue have been shown to photochemically produce singlet oxygen efficiently (Figure 1-15),[53] they rely on the use of heavier atoms to promote necessary intersystem crossing, which may not be suitable for applications in biological systems where they can compromise the integrity of the subject or the photosensitizer upon degradation. In addition, tuning of the absorbance, redox properties, and functionalities of smaller organic systems can prove to be complicated and limit the ability to tune each organic dye to a specific application. This is a similar problem with

highly efficient porphyrins and phthalocyanines, which while easily tunable, suffer from low synthetic yields.[53] In contrast, the photophysical and redox properties of transition metal complexes can be very easily tuned to a specific application through functionalization of the ligands. In addition, Ru(II) and Ir(III) complexes are able to take advantage of the spin orbit coupling of the metal center to promote the rate of intersystem crossing, allowing for more efficient singlet oxygen generation without the need for additional functionalization with heavy atoms such as halogens.

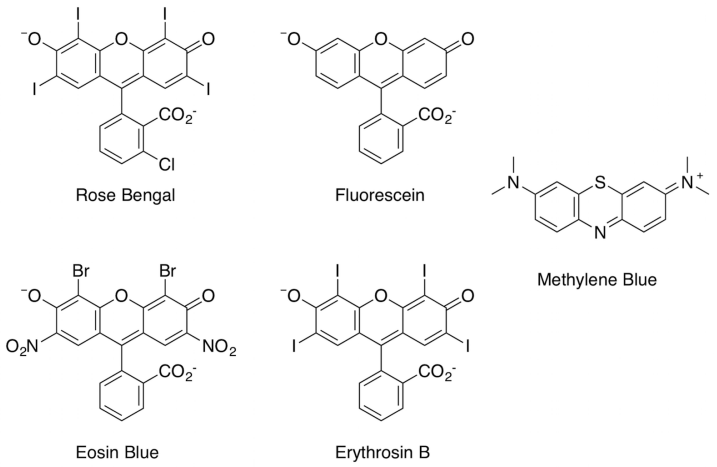

Figure 1-15. Organic dyes used in photochemical singlet oxygen generation.

To date, a number of Ru(II)[55–57] and Ir(III)[58–61]complexes (Figure 1-16) have been used as photosensitizers for singlet oxygen generation. In some cases, the performances of the complexes were better than the established organic dyes, with much lower catalyst loadings. Unfortunately, the complexes do still suffer from poorer absorption of visible wavelengths of light compared to the organic dyes. This is especially problematic for applications including photodynamic therapy, which rely on the absorbance of longer wavelengths of light in the visible and even infrared because they can more easily transmit through a number of photoactive species found in skin.[62]

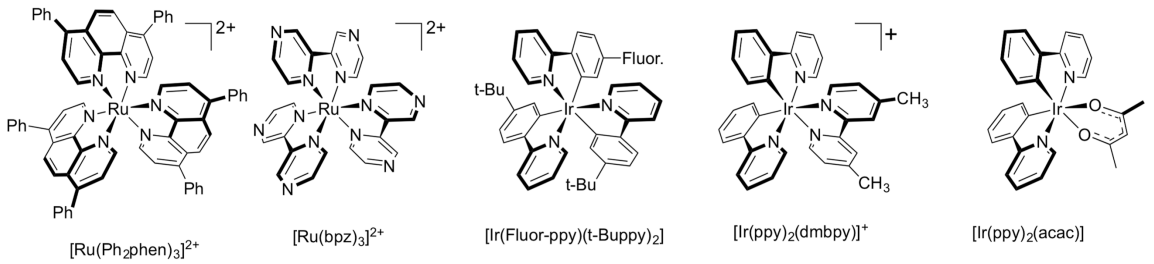

Figure 1-16. Transition metal photosensitizers for photochemical generation of singlet oxygen.

One strategy to bypass this issue has been the tethering of strongly absorbing organic dyes to increases the absorbance in the visible region, and also extend the excited state lifetimes of the complexes. Some examples include tethering of BODIPY,[63,64] corroles,[65] fluorene,[66] perylenebisimide,[67] coumarin,[68] and incorporation into a polymer backbone.[69] Unfortunately, these synthetic modifications complicate the syntheses of already expensive transition metal complexes. In order for transitional metal complexes to surmount organic dyes as photosensitizers for photochemical singlet oxygen generation, research towards designing complexes that have simple, yet effective ligand structures are of great importance.

1.3 Summary and Motivation of Thesis

In order to fully harness the abundant quantities of light energy available, the ability to efficiently convert this energy into a usable, storable form or to directly transfer it towards a particular application requires efficient, reliable photosensitizing molecules. While simple organic molecules can and have been used, they lack the immense adaptability and tunability of metal based complexes which can be tuned to each particular application. By evaluating the impacts of deliberate, structural changes to metal complexes through their ligands, the ease of designing and optimizing a system's photosensitizer can be drastically simplified. In addition, having a library of different

properties within a single family of complexes only further bolsters the utility of a single, tunable metal complex structure.

This work aims to highlight the ability to enhance the photocatalytic properties of transition metal complexes through deliberate, judicious modifications to their ligand architectures. To improve the recently explored class of $[Ir(N^N^N)(C^N)X]^+$ complexes, deliberate tuning of the electronic structure of the complexes through a "push-pull" design to further assess the impacts on photocatalytic properties for solar hydrogen generation from water and for photoredox catalysis. Additional work has extended the excited state lifetimes of Ir(III) photosensitizers with a change in the structure of the corresponding tridentate ligand, achieving excited state lifetimes that are notably high despite the lack of any organic dyes. Finally, hemicaging of more abundant metal centers including Zn(II) and Fe(II) was explored as a strategy for making more cost-effective replacements for Ru(II) and Ir(III) based photosensitizing complexes.

1.4 References

(1) U.S. Energy Information Administration. *Annual Energy Outlook 2017 with projections to 2050*; 2017.
(2) U.S. Energy Information Administration. *Projected carbon dioxide emissions are sensitive to factors driving fossil fuel use*; 2017.
(3) U.S. Department of Energy. *2010 Solar Technologies Market Report*; 2011.
(4) U.S. Department of Energy. *2014 Wind Technologies Market Report*; 2015.
(5) U.S. Department of Energy. *Hydropower Vision: A New Chapter for Americas 1st Renewable Electricity Source*; 2016.
(6) Ciamician, G. *Science* **1912**, *36*, 385–394.
(7) Juris, A.; Valzani, V.; Barigelletti, F.; Campagna, S.; Belser, P.; von Zelewsky, A. *Coord. Chem. Rev.* **1988**, *84*, 85–277.
(8) Garces, F. O.; King, K. A.; Watts, R. J. *Inorg. Chem.* **1988**, *27*, 3464–3471.
(9) Sprouse, S.; King, K. A.; Spellane, P. J.; Watts, R. J. *J. Am. Chem. Soc.* **1984**, *106*, 6647–6653.
(10) Ohsawa, Y.; Sprouse, S.; King, K. A.; DeArmond, M. K.; W., H. K.; Watts, R. J. *J. Phys. Chem. B* **1987**, *91*, 1047–1054.
(11) Colombo, M. G.; Hauser, A.; Guedel, H. U. *Inorg. Chem.* **1993**, *32*, 3088–3092.
(12) Tinker, L. L.; McDaniel, N. D.; Curtin, P. N.; Smith, C. K.; Ireland, M. J.;

Bernhard, S. *Chem. Eur. J.* **2007**, *13*, 8726–8732.
(13) Lo, K. K.; Chan, J. S.; Lui, L.; Chung, C. *Organometallics* **2004**, *23*, 3108–3116.
(14) Slinker, J. D.; Gorodetsky, A. A.; Lowry, M. S.; Wang, J.; Parker, S.; Rohl, R.; Bernhard, S.; Malliaras, G. G. *J. Am. Chem. Soc.* **2004**, *126*, 2763–2767.
(15) Lowry, M. S.; Hudson, W. R.; Pascal, R. A.; Bernhard, S. *J. Am. Chem. Soc.* **2004**, *126*, 14129–14135.
(16) Goldsmith, J. I.; Hudson, W. R.; Lowry, M. S.; Anderson, T. H.; Bernhard, S. *J. Am. Chem. Soc.* **2005**, *127*, 7502–7510.
(17) Sala, X.; Maji, S.; Bofill, R.; García-Antón, J.; Escriche, L.; Llobet, A. *Acc. Chem. Res.* **2014**, *47*, 504–516.
(18) Kärkäs, M. D.; Verho, O.; Johnston, E. V; Åkermark, B. *Chem. Rev.* **2014**, *114*, 11863–12001.
(19) Andreiadis, E. S.; Chavarot-Kerlidou, M.; Fontecave, M.; Artero, V. *Photochem. Photobiol.* **2011**, *87*, 946–964.
(20) Krishnan, C. V.; Brunschwig, B. S.; Creutz, C.; Sutin, N. *J. Am. Chem. Soc.* **1985**, *107*, 2005–2014.
(21) Cline, E. D.; Adamson, S. E.; Bernhard, S. *Inorg. Chem.* **2008**, *47*, 10378–10388.
(22) Cano-Yelo, H.; Deronzier, A. *Tetrahedron Lett.* **1984**, *25*, 5517–5520.
(23) Okada, K.; Okamoto, K.; Morita, N.; Okubo, K.; Oda, M. *J. Am. Chem. Soc.* **1991**, *113*, 9401–9402.
(24) Hasegawa, E.; Takizawa, S.; Seida, T.; Yamaguchi, A.; Yamaguchi, N.; Chiba, N.; Takahashi, T.; Ikeda, H.; Akiyama, K. *Tetrahedron* **2006**, *62*, 6581–6588.
(25) Cano-Yelo, H.; Deronzier, A. *J. Chem. Soc., Perkin Trans. 2* **1984**, 1093–1098.
(26) Okada, K.; Okubo, K.; Morita, N.; Oda, M. *Chem. Lett.* **1993**, *22*, 2021–2024.
(27) Csiba, M. A.; Barton, H. R. *Tetrahedron Lett.* **1994**, *35*, 2869–2872.
(28) Okada, K.; Okubo, K.; Morita, N.; Oda, M. *Tetrahedron Lett.* **1992**, *33*, 7377–7380.
(29) Ischay, M. A.; Anzovino, M. E.; Du, J.; Yoon, T. P. *J. Am. Chem. Soc.* **2008**, *130*, 12886–12887.
(30) Nicewicz, D. A.; MacMillan, D. W. C. *Science* **2008**, *322*, 77–80.
(31) Lin, S.; Ischay, M. A.; Fry, C. G.; Yoon, T. P. *J. Am. Chem. Soc.* **2011**, *133*, 19350–19353.
(32) McNally, A.; Prier, C. K.; MacMillan, D. W. C. *Science* **2011**, *334*, 1114–1117.
(33) Nagib, D. A.; Scott, M. E.; MacMillan, D. W. C. *J. Am. Chem. Soc.* **2009**, *131*, 10875–10877.
(34) Lowry, M. S.; Goldsmith, J. I.; Slinker, J. D.; Pascal, R. A.; Malliaras, G. G.; Bernhard, S.; Rohl, R. *Chem Mater* **2005**, *17*, 5712–5719.
(35) Chu, L.; Ohta, C.; Zuo, Z.; MacMillan, D. W. C. *J. Am. Chem. Soc.* **2014**, *136*, 10886–10889.
(36) Ventre, S.; Petronijevic, F. R.; Macmillan, D. W. C. *J. Am. Chem. Soc.* **2015**, *137*, 5654–5657.
(37) Zuo, Z.; Ahneman, D. T.; Chu, L.; Terrett, J. A.; Doyle, A. G.; MacMillan, D. W. C. *Science* **2014**, *345*, 437–440.
(38) Skubi, K. L.; Blum, T. R.; Yoon, T. P. *Chem. Rev.* **2016**, acs.chemrev.6b00018.
(39) Ochola, J. R.; Wolf, M. O. *Org. Biomol. Chem.* **2016**, *14*, 9088–9092.
(40) Le, C. "Chip"; Wismer, M. K.; Shi, Z.-C.; Zhang, R.; Conway, D. V.; Li, G.;

Vachal, P.; Davies, I. W.; MacMillan, D. W. C. *ACS Cent. Sci.* **2017**, *3*, 647–653.
(41) Brooks, A. C.; Basore, K.; Bernhard, S. *Inorg. Chem.* **2013**, *52*, 5794–5800.
(42) Douglas, J. J.; Sevrin, M. J.; Cole, K. P.; Stephenson, C. R. J. *Org. Process Res. Dev.* **2016**, *20*, 1148–1155.
(43) Beatty, J. W.; Douglas, J. J.; Miller, R.; McAtee, R. C.; Cole, K. P.; Stephenson, C. R. J. *Chem* **2016**, *1*, 456–472.
(44) Schultz, D. M.; Yoon, T. P. *Science* **2014**, *343*, 1239176–1239176.
(45) Yoon, T. P.; Ischay, M. A.; Du, J. *Nat. Chem.* **2010**, *2*, 527–532.
(46) Narayanam, J. M. R.; Stephenson, C. R. J. *Chem. Soc. Rev.* **2011**, *40*, 102–113.
(47) Shaw, M. H.; Twilton, J.; MacMillan, D. W. C. *J. Org. Chem.* **2016**, *81*, 6898–6926.
(48) Tucker, J. W.; Stephenson, C. R. J. *J. Org. Chem.* **2012**, *77*, 1617–1622.
(49) Prier, C. K.; Rankic, D. A.; MacMillan, D. W. C. *Chem. Rev.* **2013**, *113*, 5322–5363.
(50) Turro, N. J.; Chow, M. F. *J. Am. Chem. Soc.* **1981**, *103*, 7218–7224.
(51) Aubry, J. M.; Pierlot, C.; Rigaudy, J.; Schmidt, R. *Acc. Chem. Res.* **2003**, *36*, 668–675.
(52) Turro, N. J. *J. Org. Chem.* **2011**, *76*, 9863–9890.
(53) DeRosa, M. C.; Crutchley, R. J. *Coord. Chem. Rev.* **2002**, *234*, 351–371.
(54) Ashen-Garry, D.; Selke, M. *Photochem. Photobiol.* **2014**, *90*, 257–274.
(55) Demas, J. N.; Harris, E. W.; McBride, R. P. *J. Am. Chem. Soc.* **1977**, *99*, 3547–3551.
(56) Garcìa-Fresnadillo, D.; Georgiadou, Y.; Orellana, G.; Braun, A. M.; Oliveros, E. *Helv. Chim. Acta* **1996**, *79*, 1222–1238.
(57) Mulazzani, Q. G.; Sun, H.; Hoffman, M. Z.; Ford, W. E.; Rodgers, M. A. J. *J. Phys. Chem.* **1994**, *98*, 1145–1150.
(58) Djurovich, P. I.; Murphy, D.; Thompson, M. E.; Hernandez, B.; Gao, R.; Hunt, P. L.; Selke, M. *Dalton Trans.* **2007**, 3763.
(59) Gao, R.; Ho, D. G.; Hernandez, B.; Selke, M.; Murphy, D.; Djurovich, P. I.; Thompson, M. E. *J. Am. Chem. Soc.* **2002**, *124*, 14828–14829.
(60) Kando, A.; Hisamatsu, Y.; Ohwada, H.; Itoh, T.; Moromizato, S.; Kohno, M.; Aoki, S. *Inorg. Chem.* **2015**, *54*, 5342–5357.
(61) Takizawa, S.; Aboshi, R.; Murata, S. *Photochem. Photobiol. Sci.* **2011**, *10*, 895.
(62) Bonnett, R. *Chem. Soc. Rev.* **1995**, *24*, 19.
(63) Zhou, J.; Gai, L.; Zhou, Z.; Mack, J.; Xu, K.; Zhao, J.; Qiu, H.; Chan, K. S.; Shen, Z. *RSC Adv.* **2016**, *6*, 72115–72120.
(64) Wang, J.; Lu, Y.; McGoldrick, N.; Zhang, C.; Yang, W.; Zhao, J.; Draper, S. M. *J. Mater. Chem. C.* **2016**, *4*, 6131–6139.
(65) Sinha, W.; Ravotto, L.; Ceroni, P.; Kar, S. *Dalt. Trans.* **2015**, *44*, 17767–17773.
(66) Jiang, X.; Peng, J.; Wang, J.; Guo, X.; Zhao, D.; Ma, Y. *ACS Appl. Mater. Inter.* **2016**, *8*, 3591–3600.
(67) Sun, J.; Zhong, F.; Zhao, J. *Dalton Trans.* **2013**, *42*, 9595–9605.
(68) Sun, J.; Zhao, J.; Guo, H.; Wu, W. *Chem. Commun.* **2012**, *48*, 4169.
(69) Maggioni, D.; Galli, M.; D'Alfonso, L.; Inverso, D.; Dozzi, M. V.; Sironi, L.; Iannacone, M.; Collini, M.; Ferruti, P.; Ranucci, E.; D'Alfonso, G. *Inorg. Chem.* **2015**, *54*, 544–553.

Chapter 2. Push Pull $[Ir(tpy)(ppy)X]^+$ Complexes via C-F Insertion

This chapter has been adapted from a 2016 publication in the Journal of the American Chemical Society.[1] *The contributions of collaborators are noted in the experimental section.*

2.1 Introduction

The efficiency and versatility of $[Ir(ppy)_2(bpy)]^+$ based complexes as photosensitizers is attributed to the ease of tunability and functionalization of the ligand architecture. Whether it's for photocatalytic hydrogen generation, as a luminophores for OLEDs, or a photosensitizer for photocatalytic reactions including photoredox catalysis or singlet oxygen generation, the complexes can be electronically tailored for a specific application. However, the complexes continue to suffer from photodegradation regardless of application. Upon photoexcitation, the antibonding π^* orbital of the diimine ligand is populated, which leads to ligand dissociation from the reduced species. The loss of the ligand renders the complex photocatalytically inactive. This degradation has been observed experimentally when photocatalytic hydrogen generation is conducted in acetonitrile. The starting complex is no longer present after illumination, according to ESI-MS, and instead the *m*/*z* for the bis-acetonitrile adduct is observed (Figure 2-1, A and B).[2] Furthermore, there is a direct correlation between the coordinating ability of the solvent and TON of the photosensitizers for photocatalytic hydrogen generation (Figure 2-1, C).[3] Thus, efforts to circumvent this problem by design of a new, more stable architecture are of importance.

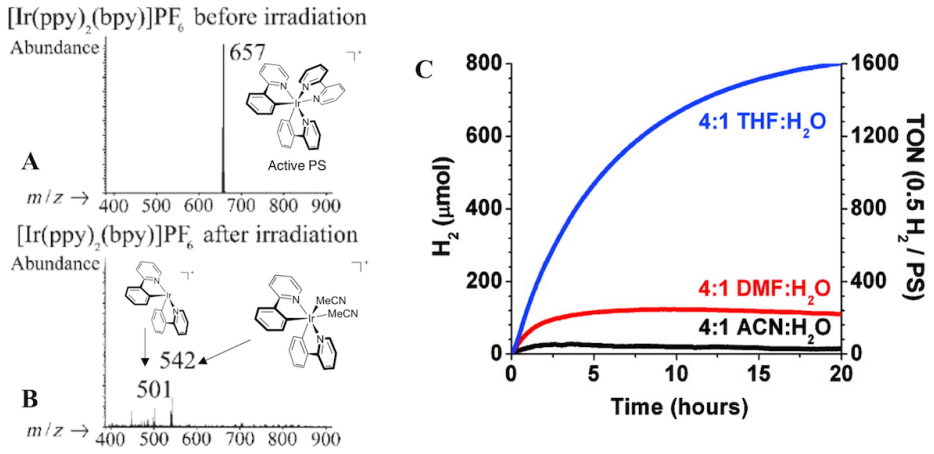

Figure 2-1. ESI-MS Analysis of photocatatlytic hydrogen generation reactions in MeCN before (A) and after (B) irradiation. Adapted from ref. [2] with permission. Copyright Wiley 2007. (C) Effect of solvent coordination on TON for photocatalytic hydrogen generation. Reprinted from ref. [3] with permission. Copyright American Chemical Society 2009.

Switching from a tris-bidentate ligand system to a bis-terdentate system could serve to improve the overall photostability of the complexes. Work by Tinker *et. al.* demonstrated that such a change results in an almost 3-fold improvement in TON (Figure 2-2) for hydrogen generation.[4] Therefore $[Ir(phbpy)_2]^+$ served as a more stable analogue to the $[Ir(ppy)_2(bpy)]^+$ structure. However, it's diminished quantum yield and complicated purification reduce its practicality as a replacement for the $[Ir(ppy)_2(bpy)]^+$. While not specifically used for water reduction, a number of other cationic, bis-terdentate Ir(III) luminophores have been published (Figure 2-3) including $[Ir(N^N^C)_2]^+$, $[Ir(N^C^N)(N^N^C)]^+$ and $[Ir(C^N^C)(N^N^N)]^+$.[5–8] These structures did offer some improvements including extended excited state lifetimes, but they also proved to be synthetically challenging Unfortunately, these complexes also suffered from a lack of tunability despite maintaining good separation of the frontier orbitals.

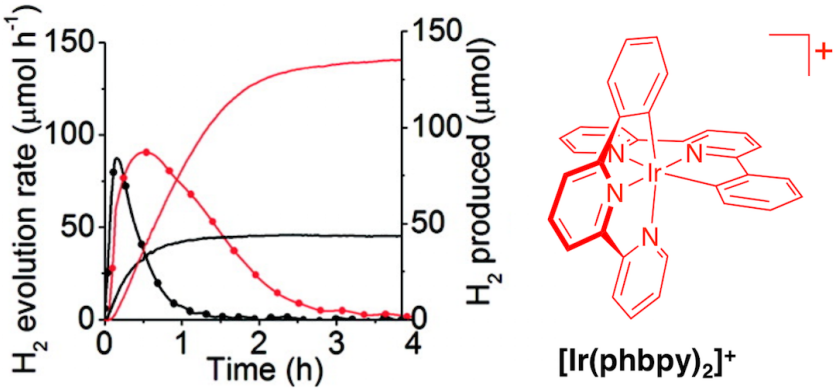

Figure 2-2. Photocatalytic H_2 evolution (solid lines, right axis) and rate of H_2 evolution (dotted lines, left axis) from $[Ir(phbpy)_2]^+$ (red) and $[Ir(ppy)_2(bpy)]^+$ (black) in 4:1 acetonitrile/water. Adapted from ref. [4] with permission. Copyright 2009 American Chemical Society.

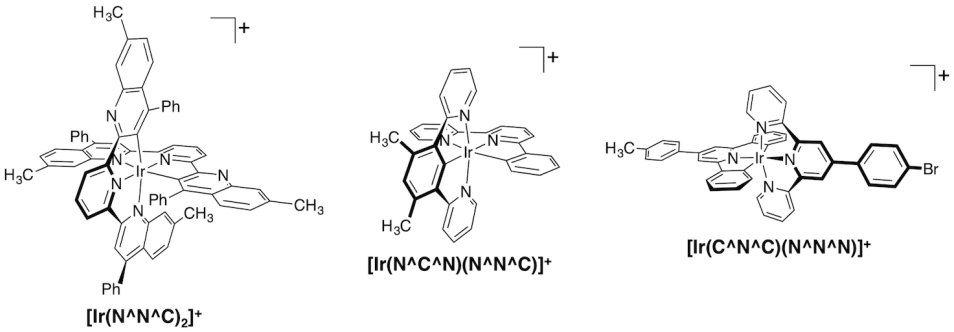

Figure 2-3. Cationic, bis-terdentate Ir(III) complexes which have previously been reported by Campagna *et. al*. $[Ir(N^N^C)_2]^+$,[5] Williams *et. al*. $[Ir(N^C^N)(N^N^C)]^+$,[6] and Scandola *et. al*. $[Ir(C^N^C)(N^N^N)]^+$.[7,8]

Work by Ishitani *et. al.* published a series of new cationic Ir(III) photocatalysts (Figure 2-4) for the reduction of CO_2.[9] The structures still contained one cyclometallating ppy ligand, but the labile diimine ligand was replaced by a more "substitution-inert" triimine ligand. The complex also features a third area of tuning with a readily exchangeable monodentate anionic ligand. Functionality of the ppy ligand was altered from electron-rich $[Ir(tpy)(4'\text{-}CH_3\text{-}ppy)Cl]^+$ to electron-poor $[Ir(tpy)(4'\text{-}CF_3\text{-}ppy)Cl]^+$, and when compared to the parent complex $[Ir(tpy)(ppy)Cl]^+$, changes in the TON_{CO} were observed. Furthermore, the oxidation potentials varied with functionality of the ppy

(+1.73 V for $[Ir(tpy)(ppy)Cl]^+$, +1.66 V for $[Ir(tpy)(4'\text{-}CH_3\text{-}ppy)Cl]^+$, and +1.73 V for $[Ir(tpy)(4'\text{-}CF_3\text{-}ppy)Cl]^+$), but the reductions remained constant (-1.04 V for $[Ir(tpy)(ppy)Cl]^+$, -1.05 V for $[Ir(tpy)(4'\text{-}CH_3\text{-}ppy)Cl]^+$, -1.05 V for $[Ir(tpy)(4'\text{-}CF_3\text{-}ppy)Cl]^+$). This demonstrated a high degree of frontier orbital separation in the complex and could lead to independent tuning of the HOMO and LUMO levels.

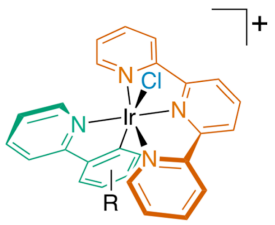

[Ir(tpy)(ppy)Cl]⁺, TON_{CO} = 40
[Ir(tpy)(4'-CH_3-ppy)Cl]⁺, TON_{CO} = 50
[Ir(tpy)(4'-CF_3-ppy)Cl]⁺, TON_{CO} = 25

Figure 2-4. $[Ir(tpy)(ppy)Cl]^+$ based photocatalysts investigated by Ishitani et. al.[9] for photocatalytic CO_2 reduction. Turnover numbers for CO after 300 min in MeCN are provided for each complex.

Work by Chirdon *et. al.*[10] further investigated this structure by altering the functionality of the terpyridine, phenylpyridine, and ancillary ligand. DFT results of the parent complex $[Ir(tpy)(ppy)Cl]^+$ confirmed that the HOMO was primarily on the ppy and ancillary ligand, and the LUMO was on the tpy (Figure 2-5). Tuning of the HOMO and LUMO levels of the complexes was readily achieved and structure-activity relationships were established. When evaluated for photocatalytic hydrogen generation using highly coordinating acetonitrile as the reaction solvent, the best performer [Ir(dMeO-phtpy)(4-Fmppy)Cl]+ was a complex with an electron-rich tpy, and an electron-poor ppy (Figure 2-6). This complex was also the most photophysically efficient of the family, with a quantum yield of 25.2 %, which is made more impressive given that it is a chloride complex, which were initially shown to be less stable than the cyanide analogues. These results lead to the exploration of this "push-pull" effect in an effort to further improve the photocatalytic properties of this highly stable structure.

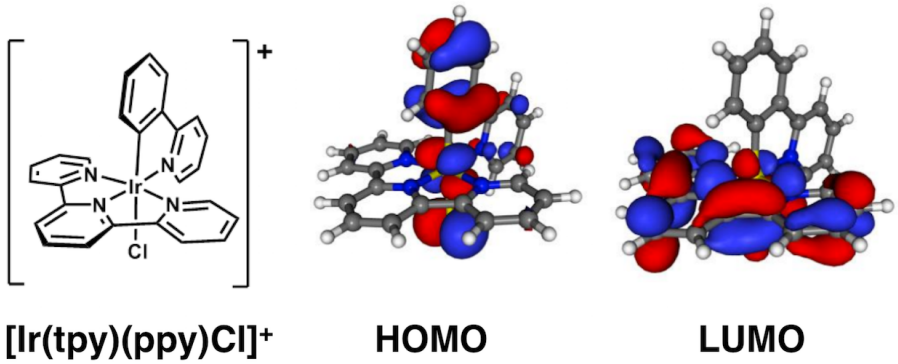

Figure 2-5. Singlet, ground state frontier orbitals of $[Ir(tpy)(ppy)Cl]^{+}$. Obtained with Gaussian '09 (B3LYP/LANL2DZ). Adapted with permission from ref [10] . Copyright 2014 American Chemical Society.

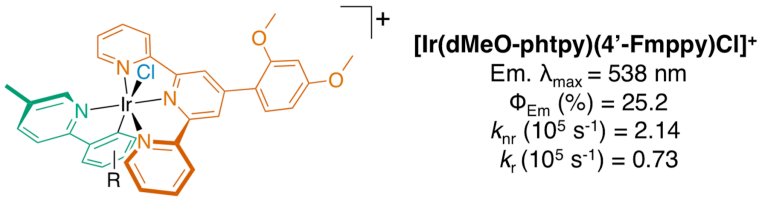

Figure 2-6. First Generation "Push-Pull" Complex with corresponding photophysical properties as reported by Chirdon et. al.[10]

In order to achieve the desired "push-pull" design, two components are required: increased energy of the LUMO with electron-donating substituents and decreased energy of the HOMO with electron-withdrawing substituents. In terms of electron-rich tpys, 4,4′,4″-tri-*tert*-butyl-2,2′:6′,2″-terpyridine (ttbutpy) is commercially available. For the ppy, several different electron-withdrawing functional groups have been used to tune Ir(III) complexes including sulfonyl,[11,12] trifluoromethyl,[13–19] pentafluorosulfur,[20] trifluoromethoxy,[21] nitrile,[22–24] and perfluorocarbonyls.[25] While these groups are excellent at modulating the HOMO of the corresponding Ir(III) complexes, the ability to install multiple on the same ligand limits their use. In contrast, fluorine is significantly simpler to introduce, allowing for multiple to be installed on the same ligand. This allows

for varying degrees of fluorination and extremes of the "push-pull" effect, and subsequently, generating strong structure-activity relationships.

This chapter presents a series of "Push-Pull" complexes that have varying degrees of fluorination on the ppy ligand, as well as exchange of the chloride ligand to a cyanide. A number of these complexes were synthetized through deliberate C-F insertion. This reaction was also analyzed to determine the fate of the fluorine. DFT calculations show the effect of fluorination on the electronic structure of the complexes, and shed light on the trends in photocatalytic activity of the complexes. Given the enhanced stability, the complexes were not only evaluated for photocatalytic hydrogen generation, but as photosensitizers for the photocatalytic decarboxylative fluorination of carboxylic acids, a dramatic photoredox transformation.

2.2 Experimental

2.2.1 General

The compounds 4,4′,4″-tri-*tert*-butyl-2,2′:6′,2″-terpyridine, $IrCl_3 \bullet 4H_2O$, and all solvents were used as received from commercial sources. The ligands mppy, 4-Fmppy, 2-Fmppy, 2,4-dFmppy, 2,6-dFmppy, and 2,4,6-tFmppy were prepared from the corresponding acyl-pyridinium salts as described by Lowry et. al.[26] The ligands PFmppy and PFMeOppy were prepared using the procedure described by Do et. al.[27] ^{1}H, ^{13}C, and ^{19}F NMR spectra were obtained using Bruker Avance 300 MHz and 500 MHz spectrometers. ^{1}H and ^{13}C NMR spectra were referenced to residual solvent signals. ^{19}F NMR spectra were referenced to $CFCl_3$ by using the PF_6 anion (-71.11 ppm, doublet) as an internal standard. ESI-MS was performed with 50 μM methanol solutions using a Thermo-Fisher LCQ instrument.

2.2.2 Synthetic Procedures

Synthesis of [Ir(ttbutpy)Cl$_3$]. In a 40 mL EPA vial, $IrCl_3 \bullet 4H_2O$ (321 mg, 0.800 mmol),4,4′,4″-tri-*tert*-butyl-2,2′:6′,2″-terpyridine (326 mg, 0.880 mmol, 1.10 eq.), and a stirbar were purged with argon for 15 minutes before injecting 13 mL of ethylene glycol. The vessel was purged with argon for an additional 10 minutes before stirring at 160 ^{o}C, in a pre-heated aluminum heating block, for 22 minutes, in the dark. Once cooled, the reaction was diluted with 25 mL of water and the red precipitate was collected on a Büchner funnel, after washing with water and diethyl ether. Yield: 86%. ^{1}H NMR (500 MHz, DMSO-d_6): δ. 9.06 (m, 2H), 8.86 (m, 2H), 8.79 (m, 2H), 7.96 (m, 2H), 1.79 (m, 9H), 1.47 (m, 18H). Concentrations necessary for ^{13}C NMR could not be attained due to poor solubility.

Synthesis of [Ir(ttbutpy)(mppy)Cl](PF$_6$) Complexes. Exploratory syntheses were initially conducted by Wesley J. Transue. In a typical reaction, a 40 mL EPA vial was charged with [Ir(ttbutpy)Cl_3] (50 mg, 0.071 mmol), cyclometallating ligand (0.213 mmol, 3.00 eq.), and a stirbar. The vessel was purged with argon for 15 minutes before 13 mL of ethylene glycol was injected, and the vessel was purged for an additional 10 minutes. The reaction was stirred at 183 ^{o}C in a pre-heated aluminum heating block, in the dark, for 18 hours. Once cooled, the reaction was diluted with 20 mL of water and sonicated. The reaction was filtered through a pad of Celite®, and the filtrate was poured into a 125 mL separatory funnel. The water-ethylene glycol mixture was extracted with 5 x 25 mL of diethyl ether. The aqueous phase was gently heated in a 40 ^{o}C water bath to remove residual diethyl ether before adding ~300 mg of KPF_6. The mixture was stirred for 1 hour

at room temperature before isolating the complex on a Büchner funnel, washing with water and diethyl ether. The complexes were then purified by evaporation of methanol from a methanol-water mixture.

[Ir(ttbutpy)(mppy)Cl](PF$_6$). Yield: 44%. ^{1}H NMR (500 MHz, acetone-*d$_6$*): *δ*. 9.96 (s, 1H), 8.97 (s, 2H), 8.79 (s, 2H), 8.35 (d, *J* = 8.36 Hz, 1H), 8.14 (d, *J* = 8.31 Hz, 1H), 7.88 (d, *J* = 7.77 Hz, 1H), 7.72 (d, *J* = 6.02 Hz, 2H), 7.55 (dd, *J* = 1.88, 6.02 Hz, 2H), 6.95 (t, *J* = 7.48 Hz, 1H), 6.74 (t, *J* = 7.42 Hz, 1H), 6.11 (d, *J* = 7.60 Hz, 1H), 2.63 (s, 3H), 1.65 (s, 9H), 1.40 (s, 18H). ^{19}F NMR (470.54 MHz, acetone-*d$_6$*): *δ*. -71.11 (d, *J* = 707.62, [PF_6^-]). ^{13}C NMR (125.77 MHz, acetone-*d$_6$*): δ 166.0, 165.6, 164.9, 159.4, 156.6, 152.3, 151.7, 145.3, 142.8, 141.6, 135.3, 131.6, 130.9, 126.4, 125.7, 124.9, 124.1, 122.6, 120.9, 37.6, 36.6, 31.1, 30.5, 18.7. MS (*m/z* ESI, CH_3OH) Calculated: 797.3 [M-PF_6^-]$^+$ Found: 797.4 [M-PF_6^-]$^+$. Elem. Anal. Calcd. For [$C_{39}H_{45}ClF_6IrN_4P$]·1/4 H_2O: C, 49.47; H, 4.84; N, 5.92. Found: C, 49.45; H, 4.87; N, 5.72.

[Ir(ttbutpy)(4-Fmppy)Cl](PF$_6$). Yield: 33%. ^{1}H NMR (500 MHz, acetone-*d$_6$*): *δ*. 9.92 (s, 1H), 8.98 (s, 2H), 8.81 (s, 2H), 8.32 (d, *J* = 8.36 Hz, 1H), 8.15 (d, *J* = 8.32 Hz, 1H), 7.97 (dd, *J* = 5.59, 8.56 Hz, 1H), 7.72 (d, *J* = 6.00 Hz, 2H), 7.56 (dd, *J* = 1.96, 6.01 Hz, 2H), 6.73 (td, *J* = 2.42, 8.86 Hz, 1H), 5.79 (dd, *J* = 2.38, 8.99 Hz, 1H), 2.62 (s, 3H), 1.66 (s, 9H), 1.40 (s, 18H). ^{19}F NMR (470.54 MHz, acetone-*d$_6$*): *δ*. -71.11 (d, *J* = 707.35, [PF_6^-]), -109.17 (s, 1F). ^{13}C NMR (125.77 MHz, acetone-*d$_6$*): *δ*.166.2, 165.7, 163.9, 163.4 (d, *J* = 252.9 Hz), 159.2, 156.4, 152.2, 151.5, 146.02 (d, *J* = 5.6 Hz), 141.7, 141.8 (d, *J* = 2.2 Hz), 135.1, 127.6 (d, *J* = 9.1 Hz), 126,4, 124.2, 122.8, 120.9, 117.8 (d, *J* = 18.3 Hz), 111.7 (d, *J* = 22.7 Hz), 37.6, 36.5, 31.0, 30.4, 18.6. MS (*m/z* ESI, CH_3OH) Calculated:

815.3 $[M\text{-}PF_6^-]^+$ Found: 815.5 $[M\text{-}PF_6^-]^+$. Elem. Anal. Calcd. For $[C_{39}H_{44}ClF_7IrN_4P]$: C, 48.77; H, 4.62; N, 5.83. Found: C, 49.53; H, 4.61; N, 5.80.

[Ir(ttbutpy)(2-Fmppy)Cl](PF$_6$). Yield: 61%. ^{1}H NMR (500 MHz, acetone-*d*$_6$): *δ*. 10.05 (s, 1H), 8.97 (s, 2H), 8.80 (m, 2H), 8.47 (d, *J* = 8.51 Hz, 1H), 8.18 (d, *J* = 8.37 Hz, 1H), 7.74 (d, *J* = 6.01 Hz, 2H), 7.55 (dd, *J* = 1.88, 6.00 Hz, 2H), 6.78 (m, 1H), 6.72 (dd, *J* = 8.18, 12.42 Hz, 1H), 5.95 (m, 1H), 2.64 (s, 3H), 1.64 (s, 9H), 1.39 (s, 18H). ^{19}F NMR (470.54 MHz, acetone-*d*$_6$): *δ*. -71.11(d, *J* = 707.35, $[PF_6^-]$), -112.54 (s, 1F). ^{13}C NMR (125.77 MHz, acetone-*d*$_6$): *δ*.166.2, 165.7, 162.0, 161.0 (d, *J* = 264.3 Hz), 159.2, 156.4, 152.3, 152.2, 145.1, 141.8, 135.6, 132.6 (d, *J* = 5.5 Hz), 132.1 (d, *J* = 8.9 Hz), 127.5 (d, *J* = 2.8 Hz), 126.4, 124.8 (d, *J* = 19.7 Hz), 124.2, 122.6, 112.1 (d, *J* = 22.7 Hz), 37.6, 36.5, 31.0, 30.4, 18.6. MS (*m/z* ESI, CH_3OH) Calculated: 815.3 $[M\text{-}PF_6^-]^+$ Found 815.4 $[M\text{-}PF_6^-]^+$. Elem. Anal. Calcd. For $[C_{39}H_{44}ClF_7IrN_4P]\cdot 1\ H_2O$: C, 47.87; H, 4.74; N, 5.73. Found: C, 47.27; H, 4.34; N, 5.52.

[Ir(ttbutpy)(2,4-dFmppy)Cl](PF$_6$). Yield: 39%. ^{1}H NMR (500 MHz, acetone-*d*$_6$): *δ*. 10.02 (d, *J* = 1.99 Hz, 1H), 8.99 (s, 2H), 8.82 (s, 2H), 8.43 (d, *J* = 9.17 Hz, 1H), 8.20 (d, *J* = 10.32 Hz, 1H), 7.74 (d, *J* = 6.01 Hz, 2H), 7.57 (dd, *J* = 2.12, 6.05 Hz, 2H), 6.65 (ddd, *J* = 2.32, 9.31, 11.81 Hz, 1H), 5.70 (dd, *J* = 2.30, 8.12 Hz, 1H), 2.64 (s, 3H), 1.65 (s, 9H), 1.40 (s, 18H). ^{19}F NMR (470.54 MHz, acetone-*d*$_6$): *δ*. -71.11 (d, *J* = 707.34, $[PF_6^-]$), -106.61 (d, *J* = 9.98 Hz, 1F), -108.82 (d, *J* = 10.00 Hz, 1F). ^{13}C NMR (125.77 MHz, acetone-*d*$_6$): *δ*.166.5, 165.9, 164.3 (d, *J* = 12.5 Hz), 161.8 (dd, *J* = 110.3, 9.7 Hz), 160.2 (d, *J* = 12.8 Hz), 159.2, 156.3, 152.3, 152.1, 147.5 (d, *J* = 6.6 Hz), 142.0, 135.6, 129.3 (dd, *J* = 5.3, 3.0 Hz), 126.5, 124.4, 124.2, 122.9, 114.3 (dd, *J* = 18.1, 3.0 Hz), 100.7 (t, *J*

= 27.0 Hz), 37.6, 36.6, 31.0, 30.5, 18.6. MS (*m/z* ESI, CH_3OH) Calculated: 833.3 [M-PF_6^-]$^+$ Found: 833.4 [M-PF_6^-]$^+$. Elem. Anal. Calcd. For [$C_{39}H_{43}ClF_8IrN_4P$]·1/2 H_2O: C, 47.44; H, 4.49; N, 5.67. Found: C, 47.35; H, 4.13; N, 5.60.

[Ir(ttbutpy)(PFmppy)Cl](PF$_6$). Yield: 36%. ^{1}H NMR (500 MHz, acetone-*d$_6$*): *δ*. 10.05 (s, 1H), 8.95 (s, 2H), 8.83 (s, 2H), 8.49 (d, *J* = 8.50 Hz, 1H), 8.27 (d, *J* = 8.47 Hz, 1H), 7.74 (d, *J* = 6.02 Hz, 2H), 7.59 (dd, *J* = 2.06, 6.02 Hz, 2H), 2.65 (s, 3H), 1.64 (s, 9H), 1.42 (s, 18H). ^{19}F NMR (470.54 MHz, acetone-*d$_6$*): *δ*. -71.11 (d, *J* = 707.39, [PF_6^-]), -134.11 (dd, *J* = 14.95, 25.13 Hz, 1F), -139.46 (ddd, *J* = 5.11, 15.09, 24.51 Hz, 1F), -153.34 (ddd, *J* = 5.05, 18.90, 24.51 Hz, 1F), -162.29 (t, *J* = 19.16 Hz, 1F). ^{13}C NMR (125.77 MHz, acetone-*d$_6$*): *δ*.166.5, 166.2, 161.1 (m), 159.7, 156.8, 152.3 (d, *J* = 17.3 Hz), 152.7, 152.4, 142.2, 136.9, 126.6, 126.5 (d, *J* = 3.0 Hz) 125.4 (d, *J* = 19.8 Hz), 124.2, 124.1, 124.0 (d, *J* = 8.0 Hz), 122.2, 122.1 (d, *J* = 5.48 Hz), 118.3 (d, *J* = 79.5 Hz), 37.5, 36.6, 31.0, 30.5, 18.7. MS (*m/z* ESI, CH_3OH) Calculated: 869.2 [M-PF_6^-]$^+$ Found: 869.5 [M-PF_6^-]$^+$. Elem. Anal. Calcd. For [$C_{39}H_{41}ClF_{10}IrN_4P$]·1/2 H_2O: C, 45.77; H, 4.14; N, 5.47. Found: C, 45.73; H, 3.93; N, 5.37.

[Ir(ttbutpy)(PFMeOppy)Cl](PF$_6$). Yield: 50%. ^{1}H NMR (500 MHz, acetone-*d$_6$*): *δ*. 9.99 (d, *J* = 2.83 Hz, 1H), 8.95 (s, 2H), 8.84 (d, *J* = 1.85 Hz, 2H), 8.52 (dd, *J* = 1.21, 9.28 Hz, 1H), 8.05 (dd, *J* = 2.77, 9.12 Hz, 1H), 7.80 (d, *J* = 5.97 Hz, 2H), 7.59 (dd, *J* = 2.13, 6.05 Hz, 2H), 4.14 (s, 3H), 1.64 (s, 9H), 1.42 (s, 18H). ^{19}F NMR (470.54 MHz, acetone-*d$_6$*): *δ*. -71.11 (d, *J* = 707.37, [PF_6^-]), -134.37 (dd, *J* = 14.84, 25.16 Hz, 1F), -141.04 (ddd, *J* = 4.34, 14.90, 19.33 Hz, 1F), -154.43 (ddd, *J* = 4.30, 18.86, 23.85 Hz, 1F), -162.37 (t, *J* =

19.14 Hz, 1F). ^{13}C NMR (125.77 MHz, acetone-d_6): δ.166.6, 166.3, 159.7, 157.5 (d, J = 0.4 Hz), 156.8, 156.2 (m), 152.5, 152.4 (d, J = 6.4 Hz), 146.7 (m), 144.8 (m), 140.7, 130.0 (m), 124.2 (d, J = 29.4 Hz), 126.6 (d, J = 19.8 Hz), 126.5, 126.0, 122.3 (d, J = 5.0 Hz), 122.2, 117.4 (d, J = 34 Hz), 57.2, 37.6, 36.5, 31.0, 30.5. MS (*m/z* ESI, CH_3OH) Calculated: 885.3 $[M\text{-}PF_6^-]^+$ Found: 885.4 $[M\text{-}PF_6^-]^+$. Elem. Anal. Calcd. For $[C_{39}H_{41}ClF_{10}IrN_4OP]\cdot 1/4\ H_2O$: C, 45.26; H, 4.04; N, 5.41. Found: C, 45.61; H, 3.93; N, 5.51.

Synthesis of [Ir(ttbutpy)(mppy)CN](PF$_6$) Complexes. In a typical reaction, a 40 mL EPA vial was charged with [Ir(ttbutpy)Cl_3] (60 mg, 0.086 mmol), cyclometallating ligand (0.255 mmol, 3.00 eq.), and a stirbar. The vessel was purged with argon for 15 minutes before 15 mL of ethylene glycol was injected, and the vessel was purged for an additional 10 minutes. The reaction was stirred at 183 ^oC in a pre-heated aluminum heating block, in the dark, for 18 hours. The vessel was cooled to room temperature, in the dark, and the heating block was cooled to 90 ^oC. The reaction was heated and an aqueous KCN solution (22 mg, 0.340 mmol, 4 eq. in 0.5 mL of water) was injected and left to stir for 2 hours at 90 ^oC. Once cooled, the reaction was diluted with 15 mL of water and 5 mL of ethanol, sonicated, and filtered through a pad of Celite®. The filtrate was poured into a 125 mL separatory funnel and extracted 5 x 25 mL with diethyl ether. The aqueous phase was gently heated in a 40 ^oC water bath to remove residual diethyl ether before adding ~ 500 mg of KPF_6. The mixture was stirred for 1 hour before isolating the complex on a Büchner funnel, washing with water and diethyl ether. The complexes were then purified by evaporation of methanol from a methanol-water mixture.

[Ir(ttbutpy)(4-Fmppy)CN](PF$_6$). Yield: 33%. ^{1}H NMR (500 MHz, acetone-*d*$_6$): *δ*. 9.82 (s, 1H), 9.07 (s, 2H), 8.89 (s, 2H), 8.34 (d, *J* = 8.41 Hz, 1H), 8.19 (d, *J* = 10.02 Hz, 1H), 7.99 (dd, *J* = 5.26, 8.63 Hz, 1H), 7.89 (d, *J* = 6.05 Hz, 2H), 7.60 (d, *J* = 8.17 Hz, 2H), 6.74 (td, *J* = 2.58, 8.84 Hz, 1H), 5.64 (dd, *J* = 2.56, 8.61 Hz, 1H), 2.65 (s, 3H), 1.68 (s, 9H), 1.42 (s, 18H). ^{19}F NMR (470.54 MHz, acetone-*d*$_6$): *δ*. -71.11 (d, *J* = 707.29, [PF_6^-]), -109.26 (s, 1F). ^{13}C NMR (125.77 MHz, acetone-*d*$_6$): *δ*.166.0, 165.7, 164.9, 164.0 (d, *J* = 253.3 Hz), 159.8 (d, *J* = 4.40 Hz), 158.8, 155.5, 154.3, 152.4, 142.4 (d, *J* = 2.13 Hz), 141.7, 136.1, 128.0 (d, *J* = 1.76 Hz), 127.8 (d, *J* = 8.6 Hz), 126.6, 124.6, 123.3, 121.4, 117.1 (d, *J* = 17.3 Hz), 112.2 (d, *J* = 23.1 Hz), 37.6, 36.6, 31.0, 30.4, 18.5. MS (*m/z* ESI, CH_3OH) Calculated 806.0 [M-PF_6^-]$^+$Found 806.5 [M-PF_6^-]$^+$. Elem. Anal. Calcd. For [$C_{40}H_{44}F_7IrN_5P$]·1/3 KPF_6: C, 47.47; H, 4.38; N, 6.92. Found: C, 47.56; H, 4.19; N, 6.89.

[Ir(ttbutpy)(2,4-dFmppy)CN](PF$_6$). Yield: 47%. ^{1}H NMR (500 MHz, acetone-*d*$_6$): *δ*. 9.92 (s, 1H), 9.08 (s, 2H), 8.90 (s, 2H), 8.47 (dd, *J* = 1.91, 8.53 Hz, 1H), 8.25 (dd, *J* = 1.85, 8.50 Hz, 1H), 7.91 (d, *J* = 9.03 Hz, 2H), 7.62 (dd, *J* = 2.14, 6.06 Hz, 2H), 6.65 (ddd, *J* = 2.33, 9.23, 12.66 Hz, 1H), 5.54 (dd, *J* = 2.34, 7.61 Hz, 1H), 2.67 (s, 3H), 1.67 (s, 9H), 1.42 (s, 18H). ^{19}F NMR (470.54 MHz, acetone-*d*$_6$): *δ*. -71.11 (d, *J* = 707.23, [PF_6^-]), -106.42 (d, *J* = 10.09 Hz, 1F), -108.30 (d, *J* = 10.10 Hz, 1F). ^{13}C NMR (125.77 MHz, acetone-*d*$_6$): *δ*.166.4, 165.9, 164.7 (d, *J* = 11.7 Hz), 162.7 (dd, *J* = 11.5, 3.5 Hz), 162.2 (d, *J* = 7.3 Hz), 161.6 (dd, *J* = 5.0, 1.3 Hz), 160.7 (d, *J* = 11.5 Hz), 158.8, 155.5, 155.3, 152.6, 142.0, 136.6, 126.7, 124.9, 124.8, 124.7, 123.5, 113.3 (dd, *J* = 2.9, 7.0 Hz), 101.2 (t, *J* = 27.6 Hz), 37.7, 36.6, 31.0, 30.5, 18.6. MS (*m/z* ESI, CH_3OH) Calculated: 824.3

$[M\text{-}PF_6^-]^+$ Found: 824.5 $[M\text{-}PF_6^-]^+$. Elem. Anal. Calcd. For $[C_{40}H_{43}F_8IrN_5P]\cdot 1/2\ KPF_6$: C, 45.28; H, 4.09; N, 6.60. Found: C, 46.40; H, 3.57; N, 6.55.

[Ir(ttbutpy)(PFMeOppy)CN](PF$_6$) (**3c**). Yield: 22%. ^{1}H NMR (500 MHz, acetone-d_6): δ. 9.81 (s, 1H), 9.00 (s, 2H), 8.90 (s, 2H), 8.55 (d, J = 9.15 Hz, 1H), 8.09 (d, J = 9.06 Hz, 1H), 7.96 (d, J = 5.70 Hz, 2H), 7.64 (d, J = 5.46 Hz, 2H), 4.16 (s, 3H), 1.65 (s, 9H), 1.43 (s, 18H). ^{19}F NMR (470.54 MHz, acetone-d_6): δ. -71.11 (d, J = 707.25, $[PF_6^-]$), -134.25 (dd, J = 16.29, 27.06 Hz, 1F), -140.23 (m,1F), -154.10 (ddd, J = 4.23, 18.80, 26.84 Hz, 1F), -161.63 (t, J = 18.98, 1F). ^{13}C NMR (125.77 MHz, acetone-d_6): δ.166.6, 166.3, 159.5, 159.5, 158.3 (d, J = 1.2 Hz), 156.1, 152.8, 152.7, 143.8, 143.4, 127.0 (d, J = 20.8 Hz), 126.8, 126.7 (d, J = 8.8 Hz), 126.0, 125.1 (d, J = 11.3 Hz), 124.8, 124.4, 123.6 (m), 122.7, 122.6 (d, J = 17.1 Hz), 57.2, 37.6, 36.7, 31.0, 30.5. MS (*m/z* ESI, CH_3OH) Calculated: 876.3 $[M\text{-}PF_6^-]^+$Found: 876.4 $[M\text{-}PF_6^-]^+$. Elem. Anal. Calcd. For $[C_{40}H_{41}F_{10}IrN_5OP]$: C, 47.06; H, 4.05; N, 6.86. Found: C, 46.72; H, 4.01; N, 6.67.

2.2.3 Electrochemical Characterization

Cyclic voltammetry experiments were performed using a CH-Instruments Electrochemical Analyzer 600C potentiostat with a three-electrode system consisting of a platinum coil counter electrode, a silver wire pseudo-reference, and a 1 mm^2 platinum disk working electrode. Scans were performed with positive scan polarity, at 0.10 V/S, under an atmosphere of argon, using argon-purged acetonitrile solutions that contained 0.10 M tetra-*n*-butylammonium hexafluorophosphate as the supporting electrolyte and 0.5 mM of the analyte. An internal standard of ferrocene was added to each solution, referencing potentials to SCE via the oxidation of ferrocene at 0.40 V.[28]

2.2.4 Computational Modeling

DFT Calculations were performed using the Gaussian '09 suite.[29] The triplet and singlet ground-state and excited-state were evaluated for the complexes using the B3LYP functional and the LANL2DZ basis set. No symmetry conditions were specified. For TD-DFT calculations, the optimized singlet ground-state geometry was used for the 150 lowest excitations and solvent (acetonitrile) was specified. Orbitals were visualized using Avogadro: an open-source molecular builder and visualization tool Version 1.1.1.[30] TD-DFT calculations of UV-Vis absorption spectra were visualized using Gaussum,[31] where transitions were expanded into Gaussian curves with a full-width at half-maximum (fwhm) set to 4000 cm^{-1}.

2.2.5 Photophysical Characterization

Room temperature photophysical measurements were conducted using argon-purged 10 μM acetonitrile solutions in screw-top, quartz cuvettes. UV-vis absorption spectra were collected with a Shimadzu UV-1800 spectrophotometer. Photoluminescence characterization experiments were performed using a Fluorolog-3 spectrophotometer equipped with dual monochromators and a photomultiplier tube (PMT) at a right-angle geometry. All compounds were excited at 380 nm. Excited state lifetimes were determined by pulsing samples at 266 nm using the fourth harmonic of a Nd:YAG (Continuum Minilite II) laser. Emission decays were monitored with an oscilloscope (Tektronix TDS 3032B) and converted into a linear regression using a Labview PC interface. Emission quantum yields were determined by comparison against a 10 μM $[Ru(bpy)_3]PF_6$ reference in acetonitrile, with an established quantum yield (Φ_{ref} = 0.062).[32] Quantum yields were calculated using the equation $\Phi_s = \Phi_{ref}$

$(I_s/I_{ref})(A_{ref}/A_s)(\eta_s/\eta_{ref})$, where Φ_s is the quantum yield of the sample, Φ_{ref} is the quantum yield of the reference, I_s and I_{ref} are the maximum emission intensities for the sample and the reference, A_s and A_{ref} are the absorbances of the sample and reference at the excitation wavelength, and η_{ref} and η_s are the refractive indices of the solvents. Radiative decay constants (k_r) were calculated using the equation $k_r = (\Phi_s/\tau_s)$ where τ_s is the excited state lifetime of the sample and subsequently nonradiative decay constants (k_{nr}) were calculated using the relationship $k_{nr} = (1/\tau_s) - kr$. Emission intensities were corrected for the detector's response over the spectral range.

2.2.6 Photocatalytic Hydrogen Generation

Photocatalytic generation and quantification of H_2 was carried out by Isaac N. Mills using the fixed protocol described by Cline et. Al.[33] Screw top EPA vials (40 mL) contained 10 mL of solvent (8 mL acetonitrile, 1 mL triethylamine, 1 mL water), 0.075 mM photosensitizer, and 300 nmol K_2PtCl_4. Control vials were prepared without the photosensitizer, the catalyst, or trimethylamine, or with all components present but without illumination. The vials were placed in a 16 well, temperature controlled photoreactor mounted on an orbital shaker. Each vial was equipped with a pressure transducer as well as a bottom LED for illumination (Luxeon V Dental blue LEDs, LXHL-LRD5 with collimating optics Fraen FHS-HNBI-LL01-H). The vials were sealed and subsequently degassed with 7 cycles of vacuum and argon, after which the vials were equilibrated to atmospheric pressure at 22 ^oC. The orbital shaker was started (100 rpm) and the samples were illuminated. Generation of H_2 was monitored over time by conversion of the pressure transducer readings into pressure traces via a Labview PC interface. Illumination ceased when no further increase in the traces was observed.

Following illumination, quantification of H_2 produced was accomplished by injecting 1 mL of the vial headspace in a GOW-MAC gas chromatograph (thermal conductivity detector, Ar carrier gas), pre-calibrated using 10% H_2/Ar gas mixtures.

2.2.7 Photoredox Catalysis

The photoredox catalysis studies were performed using reaction conditions reported by Ventre et. al.[34] Screw top EPA vials (20 mL) containing 4 mL of solvent (3 mL acetonitrile, 1 mL water), 400 μmol of diphenylacetic acid, 800 μmol of Na_2HPO_4, 1.2 mmol of Selectfluor®, and 0.2 μmol (0.05 mol %) of photosensitizer were equipped with pressure transducers in a 16 well, temperature controlled photoreactor on top of an orbital shaker. Samples were degassed with 7 cycles of vacuum and argon, after which the vials were equilibrated to atmospheric pressure. The orbital shaker was started (100 rpm) and the samples were illuminated from the bottom at 22 ^oC (Luxeon V Dental blue LEDs, LXHL-LRD5 with collimating optics Fraen FHS-HNBI-LL01-H). Generation of CO_2 was monitored over time by conversion of the pressure transducer readings into pressure traces via a Labview PC interface. Illumination ceased when no further increases in the pressure traces were observed. The crude reaction mixtures were directly analyzed by ^{19}F NMR using hexafluorobenzene as an internal standard.

2.3 Results and Discussion

2.3.1 Synthesis

To achieve the desired "push-pull" design, an [Ir(tpy)Cl_3] precursor with an electron rich terpyridine, **1a** was needed. Like previous tri-chloride precursors, reacting 4,4′,4″-tri-*tert*-butyl-2,2′:6′,2″-terpyridine with $IrCl_3$•$4H_2O$ in ethylene glycol gave **1a** in

high yield. Exclusion of light and air, extension of reaction time, increase of reaction temperature, and dilution of the reaction were necessary for optimal yields.

The chloro-complexes (**2a-2f**) were synthesized with the corresponding mppy derivative in ethylene glycol, as shown in Scheme 2-1. Optimal yields were achieved with higher reaction temperature, extended reaction time, and significant dilution for overcoming the poor solubility of **1a** in ethylene glycol. The corresponding cyano complexes (**3a-3c**) were synthesized via a one-pot reaction of the corresponding chloro complex with aqueous KCN after cyclometallation, as shown in Scheme 2-2. All complexes were isolated as the PF_6 salts after anion-metathesis with aqueous KPF_6.

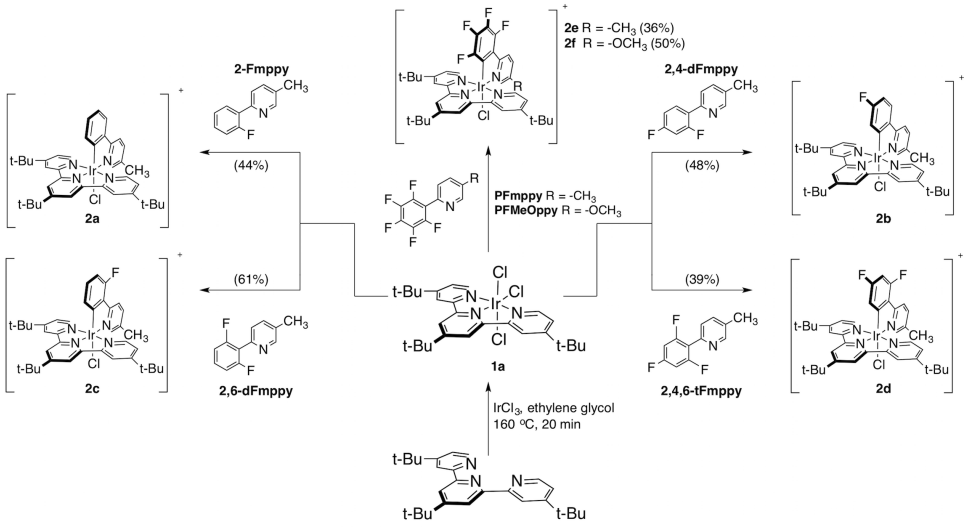

Scheme 2-1. Synthetic Pathways and Labels of Ir(III) Complexes. Isolated yields in parentheses. Reaction conditions as follows: a) mppy ligand, ethylene glycol, argon atmosphere, 182 ^{o}C, overnight. Adapted with permission from ref 1. Copyright 2016 American Chemical Society.

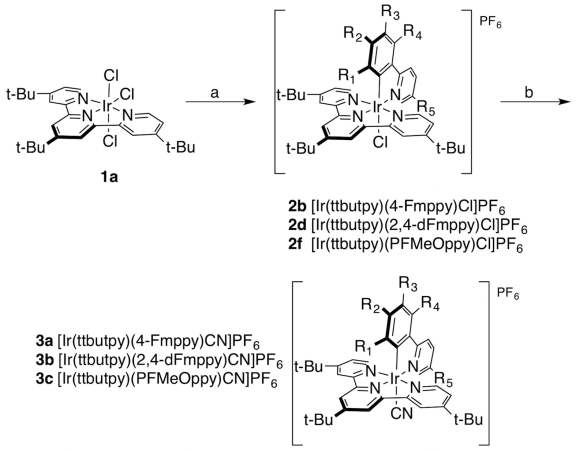

Scheme 2-2. Chloride-Cyanide Exchange of Ir(III) Complexes. Reprinted with permission from ref 1. Reaction conditions as follows: a) mppy ligand, ethylene glycol, argon atmosphere, 182 ^{o}C, overnight. b) KCN (aq), ethylene glycol, argon atmosphere, 90 ^{o}C, 2 h. Copyright 2016 American Chemical Society.

The mppy ligand derivatives were synthesized via Kröhnke condensation of the corresponding phenylacyl-pyridinium salt with methacrolein[26] or via a CuI catalyzed cross coupling of pentafluorobenzene with the corresponding 2-bromopyridine precursor (Scheme 2-3).[27]

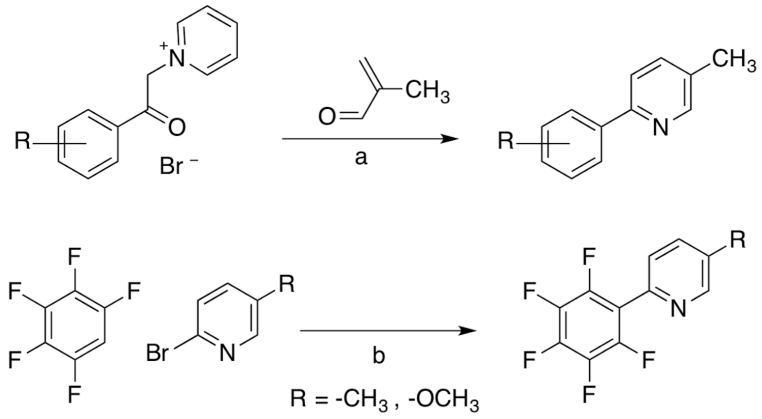

Scheme 2-3. Synthetic pathways for fluorinated phenylpyridine ligands. Reaction conditions as follows: a) NH_4OAc, MeOH, 65 ^{o}C overnight. b) K_3PO_4, 1,10-phenanthroline, CuI, DMF/Xylenes, overnight.

2.3.2 C-F Activation

Addition of fluorine atoms to the mppy ligand was necessary in order to achieve the desired "push-pull" design of the complexes by altering the HOMO energy levels. It was thought that cyclometallations of Ir(III) with mppy-type ligands have shown preference of C-H over C-F activation, specifically with *ortho*-fluorinated ligands. However, in the reaction of 2,4-dFmppy with **1a**, it was observed that the mono-fluorinated complex **2b** was the primary product, with small quantities of the di-fluorinated complex **2d** detected by analysis of the crude reaction mixture with ^{19}F NMR and ESI-MS (Figure 2-7 A, B). A similar behavior was observed in the reaction of **1a** with 2-Fmppy, whereby the C-F activation product **2a** was the reaction product, with small quantities of the monofluorinated **2c** detected by ^{19}F NMR and ESI-MS (Figure 2-7 C, D). Purification of these reactions by crystallization after precipitation of the PF_6 salt only produced the pure C-F activation products. Subsequently, to synthesize **2d**, 2,4,6-tFmppy was instead used as the cyclometallating ligand, whereas to synthesize **2c**, 2,6-dFmppy was used. C-F activation was also observed by the formation of the perfluorinated complexes when perfluorophenyl ligands were used (Scheme 2-1).

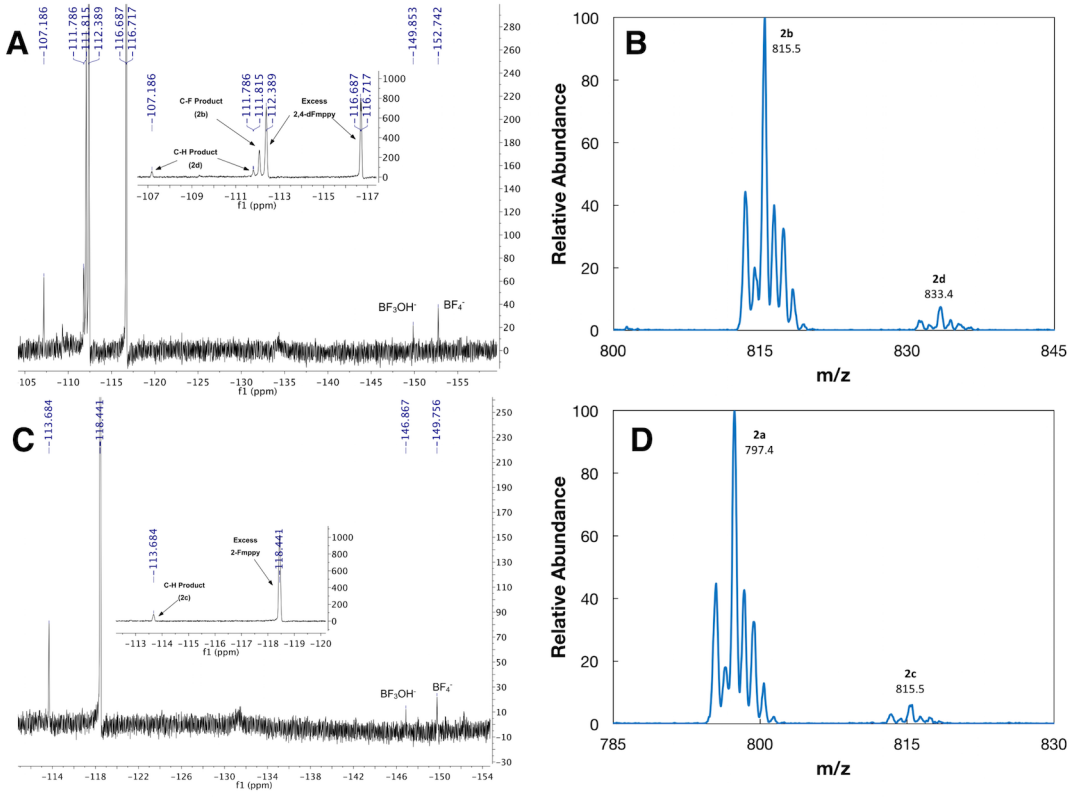

Figure 2-7. C-F insertion reaction analyses. ^{19}F (A) and ESI-MS (B) of reaction of **1a** with 2,4-dFmppy along with ^{19}F (C) and ESI-MS (D) of reaction of **1a** with 2-Fmppy.

Given the preference of C-F activation over C-H, it was then possible to synthesize complexes **2a** and **2b** using C-F or C-H activation, as shown in Scheme 2-4**.** It should be noted that yields of the reactions using C-F activation were comparable in the synthesis of **2a** (44% using 2-Fmppy, 40% using mppy), but were significantly higher in the synthesis of **2b** (48% using 2,4-dFmppy versus 33% for 4-Fmppy). In all cases, the ancillary ligand for the complexes synthesized via C-F activation remained a chloride and was not exchanged to fluoride, as confirmed by ^{19}F NMR and mass spectrometry. Over the course of the reaction, protons from the solvent or residual water reacted with the liberated fluorine, generating hydrofluoric acid, which then reacts with borosilicate glass reaction vessels. The appearance of BF_4^- and BF_3OH^- was detected via ^{19}F NMR of the crude reaction mixture (Figure 2-7) and corroborates observations made in similar C-F

insertion reactions[35]. Formation of SiF_6^{2-} was anticipated,[36] however it could not be detected by ^{19}F NMR.

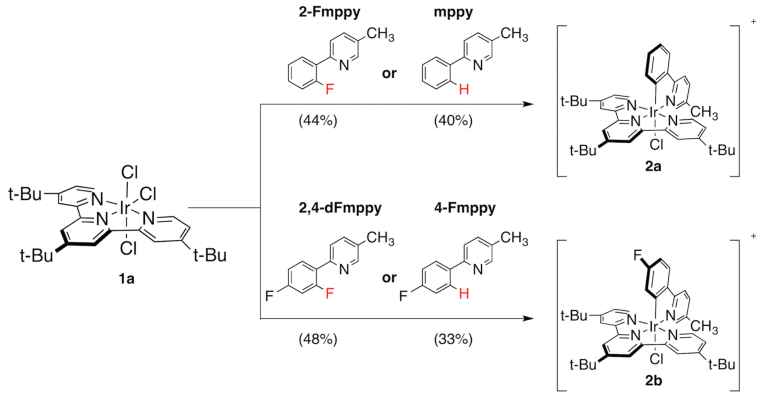

Scheme 2-4. Syntheses of **2a** and **2b** using C-F and C-H activation under identical reaction conditions. Isolated yields in parentheses. Note: The C-F activation products are the major product of the reactions, with trace amounts of the C-H products being detected by ^{19}F NMR and ESI-MS analysis of the crude reaction mixtures. Reprinted from ref 1 with permission. Copyright 2016 American Chemical Society.

The preferential C-F activation of the complexes over C-H is likely due to the formation Ir(I) species typically generated during cyclometallation reactions performed in oxidizable solvents and the elevated reaction temperatures favoring C-F activation over C-H. In the presence of oxidizable ethylene glycol, **1a** is likely reduced to a transient Ir(I) species, which upon oxidative addition to a fluorinated mppy ligand, is then re-oxidized to the final Ir(III) species. Given the elevated reaction temperatures, thermodynamic control of the products would produce more of the C-F activation product over the C-H product. To better understand the reaction, attempts to perform control reactions were made using solvents that are inert to oxidation including 2,3-dimethyl-2,3-butanediol, 2,5-dimethyl-2,5-hexanediol, and *tert*-butanol. These were inconclusive since the lower solubility of the starting materials could have prevented any C-F activation from occurring. Additionally, attempts to run the reactions at lower temperatures were made, however no reaction occurred which indicated an elevated energy barrier for the reaction.

2.3.3 Computational Modeling

The electronic structures of the complexes were modeled using static DFT calculations, using the B3LYP functional and the LANL2DZ basis set for both the singlet and triplet states. The frontier orbitals for the singlet and triplet states of the monofluorinated-chloro complex **2c** and the perfluorinated-cyano complex **3c** are depicted in Figure 2-8. Much like the previously published complexes,[10] the LUMO of each complex is located primarily on the terpyridine ligand with contributions from the d orbitals of the metal center, owing to the strongly electron-donating *tert*-butyl groups on the terpyridine. The HOMO of the complexes display contributions from the phenyl ring of mppy ligand, the iridium d orbitals, and the ancillary ligand.

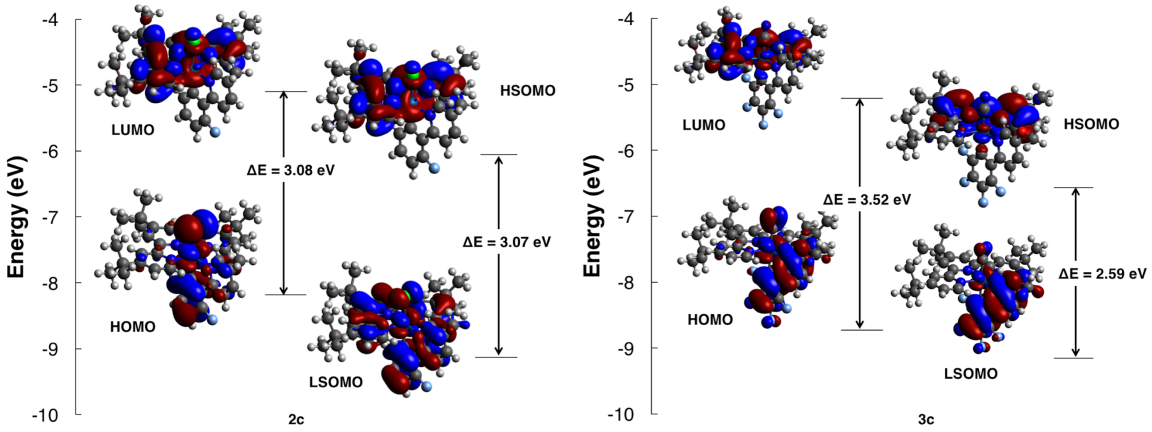

Figure 2-8. Singlet and triplet frontier orbitals of **2c** (left) and **3c** (right) from Gaussian '09 DFT Calculations. Reduction in LUMO metal character, HSOMO metal character, and LSOMO metal character is observed when going from monofluorinated chloride complex **2c** to perfluorinated cyanide complex **3c**. Transition from HSOMO to LSOMO is a mixed MLCT/ILCT for **2c**, whereas in **3c** it is primarily ILCT. Reprinted from ref 1 with permission. Copyright 2016 American Chemical Society.

For the chloro complexes, when the mppy ligands become increasingly fluorinated, the electronic structure of the LUMO remains unchanged. However, the LUMOs of the cyano complexes show a decrease in metal character as the complexes increase in fluorination. The electronic structure of the HOMO for the chloro complexes

has an increase in the electron density of the phenyl ring in the mppy ligand as you increase fluorination. A similar trend is observed in the cyano complexes. The addition of a methoxy group to the pyridine ring in chloro complex **2f** and cyano complex **3c** results in an increase in the contribution of the entire pyridine ring to the HOMO.

As the chloro complexes become more fluorinated, the HOMO energy levels of the complexes are reduced compared to the unsubstituted **2a**. Fluorination also results in a broadening of the HOMO-LUMO gap within a 0.36 eV range for the chloro complexes. Both of these trends are also seen in the corresponding cyano complexes. Exchange of the chloride to a stronger field cyanide ligand results in a decrease in the HOMO levels by 0.26 eV, as well as broadening of the HOMO-LUMO gaps.

2.3.4 UV-Vis Absorption Spectroscopy & TD-DFT

The absorption spectra of complexes **2b**, **2f**, and **3c** are shown in Figure 2-9, with key absorption maxima and extinction coefficients shown in Table 2-1. Complex **2b**'s spectrum is representative of the chloride complexes **2a**-**2d**, whereas **2f** is representative of the perfluorinated, chloride complexes. The spectrum of **3c** is representative of the cyanide complexes **3a**-**3c**. The spectra of chromophores with a $[Ir(tpy)(ppy)X]^+$ ligand structure, and the origins of the observed transitions are similar to published spectra[10] as indicated by TD-DFT calculations (Figure 2-10). A weak feature near 475 nm (HOMO→LUMO, mixed MLCT/ILCT) is present in all of the chloro complexes **2a-2f** which is adjacent to stronger transition at 390 nm (HOMO-1→LUMO and HOMO→LUMO+1, mixed MLCT/ILCT). Upon exchange of the chloride to a cyanide, these features subsequently disappear. TD-DFT calculations of **3c** indicate that these transitions, albeit weaker, are instead blue-shifted to 402 nm (HOMO→LUMO, mixed

MLCT/ILCT) and 343 nm (HOMO-2→LUMO and HOMO→LUMO+2, mixed MLCT/ILCT) respectively. Subsequently, the region between 280 nm and 320 nm lacks any strong absorption bands for the chloride complexes with the exception of the perfluorinated complexes **2e** and **2f**. Two bands near 280 nm (HOMO-7→LUMO and HOMO-6→LUMO+1, mixed MLCT/ILCT) and 320 nm (HOMO-4→LUMO and HOMO-5→LUMO, mixed MLCT/ILCT) are prominent in these complexes, and is contrary to the spectra observed from previously published chloride analogues. Instead, this region bears similarities to that of the cyano complexes **3a** – **3c**, which are characterized by mixed MLCT/ILCT transitions at 280 nm (HOMO-4→LUMO+1 and HOMO-3→LUMO+1) and 320 nm (HOMO-4→LUMO and HOMO-3→LUMO). The emergence of these features in **2e** and **2f** is likely due to the strong electron-withdrawing nature of the perfluorophenyl moiety. Finally, a strong feature at 240 nm is present in all complexes originating from an ILCT (ancillary ligand p orbitals, π orbitals of the central ring of the terpyridine, and π orbitals of the phenyl ring of the mppy to π * orbitals of the terpyridine and π * orbitals of the pyridine ring of the mppy). This feature is blue shifted as complexes increase in fluorination, as well as upon exchange of a chloride to a cyanide due to increasing stabilization of the frontier orbitals.

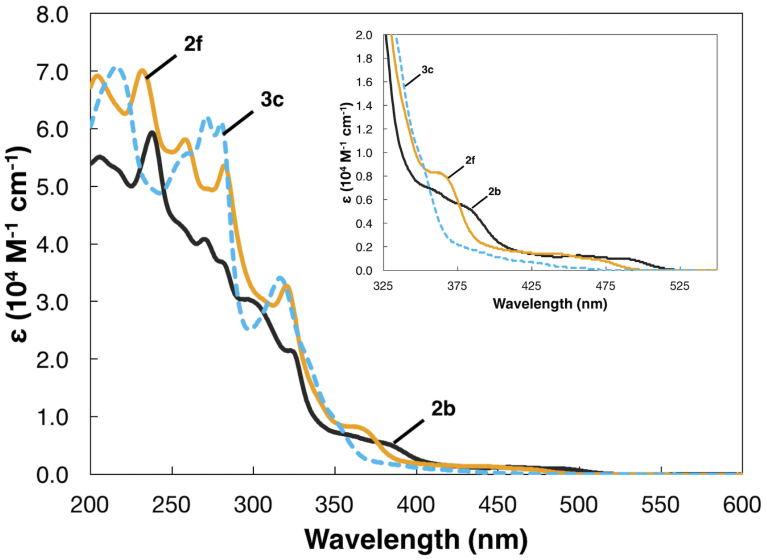

Figure 2-9. UV-vis absorption spectra for **2b** (solid black), **2f** (solid orange), and **3c** (dashed blue). Spectra were collected in MeCN (10 micromolar) at room temperature. The region from 325 nm to 550 nm is enlarged in the inset to show details of the weakest, low energy transitions. Reprinted from ref 1 with permission. Copyright 2016 American Chemical Society.

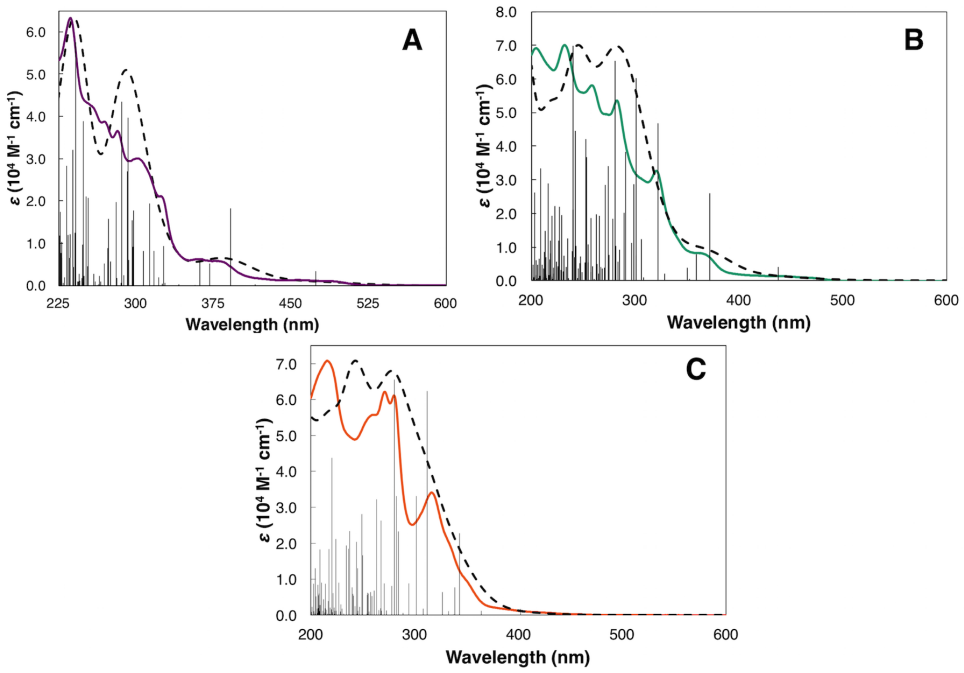

Figure 2-10. Experimental. (solid, colored) and calculated (black dashed) UV-Vis absorption spectra of **2c** (A), **2f** (B), **3c** (C). Calculated spectra were determined using Gaussian '09 TD-DFT calculations and Gaussum software with a fwhm = 4000 cm^{-1}. Oscillator strengths are included as vertical lines. Reprinted from ref 1 with permission. Copyright 2016 American Chemical Society.

Table 2-1. Photophysical Properties of "Push-Pull" Ir(III) Complexes.

complex	**absorption** λ_{max}/ nm (intensity/10^4 M^{-1} cm^{-1})	**Emission** λ_{max}/ nm	τ/ μs	Φ/ %	k_{nr} (10^5) / s^{-1}	k_r (10^5) / s^{-1}
2a	237 (5.37), 256sh (3.75), 270 (3.55), 280sh (3.34), 303 (2.74), 326sh (1.71), 361 (0.61), 382sh (0.54), 465 (0.14)	537	3.02	60.7 ± 5.2	1.30	2.01
2b	205 (5.50), 238 (5.93), 256sh (4.31), 269 (4.08), 277sh (3.74), 296sh (3.04), 323 (2.15), 381 (0.54), 450 (0.13)	525	3.17	64.6 ± 5.5	1.12	2.04
2c	204 (5.41), 236 (6.32), 256sh (4.26), 269 (3.87), 282 (3.65), 302 (3.00), 323sh (2.10), 358 (0.62), 382 (0.57), 455 (0.13)	525	3.77	69.3 ± 5.9	0.81	1.84
2d	206 (5.28), 237 (6.01), 257 (4.22), 268sh (3.81), 280 (3.40), 304sh (2.59), 323 (2.17), 375sh (0.57), 450 (0.14)	515	3.87	58.6 ± 5.0	1.07	1.51
2e	203 (6.46), 232 (6.35), 252sh (5.05), 282 (4.34), 320sh (2.61), 366 (0.74), 436 (0.14)	498	3.05	50.0 ± 4.3	1.64	1.64
2f	204 (6.91), 232 (7.01), 258 (5.81), 280 (5.27), 320 (3.27), 365 (0.81), 435 (0.14)	498	3.15	47.5 ± 4.1	1.67	1.51
3a	216 (6.72), 238 (5.28), 271 (5.41), 280 (5.26), 316 (2.89), 430 (0.01)	488	3.35	55.8 ± 5.1	1.32	1.67
3b	216 (6.69), 270 (5.28), 280 (4.89), 317 (3.02), 428 (0.01)	480	3.50	61.8 ± 5.9	1.09	1.77
3c	216 (7.08), 255sh (5.49), 271 (6.21), 280 (6.11), 316 (3.40), 337sh (1.72),	470	9.93	41.4 ± 4.2	0.59	0.42

2.3.5 Emission Spectroscopy

All of the complexes were strongly emissive in degassed, room temperature acetonitrile, with emission colors ranging from yellow to blue-green (Figure 2-11). Complexes **2a-2d** have broad, structureless emissions that are consistent with a mixed metal to ligand charge transfer (MLCT) and intraligand charge transfer (ILCT) that is characteristic of cyclometallated iridium complexes. Conversely, complexes **2e-2f** and

3a-3c have increasingly greater vibrational substructure in their emission, indicating a greater degree of ILCT emission than MLCT, as the complexes are fluorinated, as corroborated with DFT calculations (Figure 2-8). This increase in vibrational substructure is also observed when the chloride ligand is switched to a cyanide.

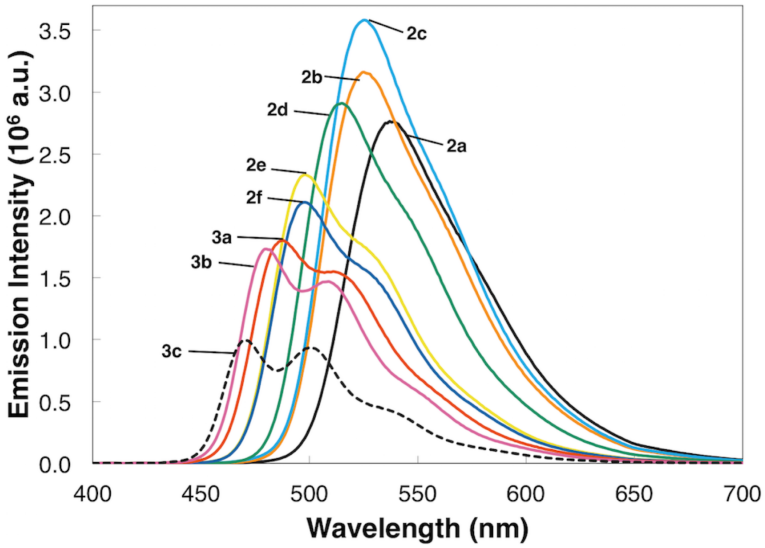

Figure 2-11. Room temperature emission spectra of degassed 10 μM solutions in acetonitrile. Complexes were excited at 380 nm. Vibrational substructure is visible in the spectra of complexes with predominantly ILCT transitions (**2e-2f**, **3a-3c**). Reprinted from ref 1 with permission. Copyright 2016 American Chemical Society.

As the mppy ligand becomes more fluorinated, the emission maxima of the complexes blue-shifts, owing to an increase in the stabilization of the HOMO (Table 2-1). When comparing **2e** and **2f**, the emission maxima of the complexes is unaffected despite the addition of the methoxy group to **2f**. Exchange of the chloride ligand to a cyanide blue-shifts the emission maxima when compared to the corresponding chloride analogues. It is worth noting that despite **2b** and **2c** having a single fluorine, they both have higher quantum yields than the unsubstituted **2a**. When compared to other iridium complexes,[26] the excited state lifetimes of the complexes are notably high, averaging 3.3 μs, with the exception of **3c** which is three times as long. The k_{nr} rate constants of **2a-3c**

are lower than other published Ir(III) complexes with the $[Ir(tpy)(ppy)X]^+$ ligand structure, [10] indicating that the complexes have more desirable photophysical properties (Figure 2-12). In addition, excluding **2e** and **2f**, all complexes have lower k_{nr} rate constants compared to the most popular "push-pull" derivative of the $[Ir(ppy)_2(bpy)]^+$ family, $[Ir(dF(CF_3)ppy)_2(dtbbpy)]PF_6$ (k_{nr} = 1.39 x 10^5 s^{-1}).[37] The complexes also have high k_r rate constants, but are lower relative to $[Ir(dF(CF_3)ppy)_2(dtbbpy)]PF_6$ (k_r = 2.96 x 10^5 s^{-1}). The increased quantum efficiency of these complexes can be attributed to their "push-pull" design.

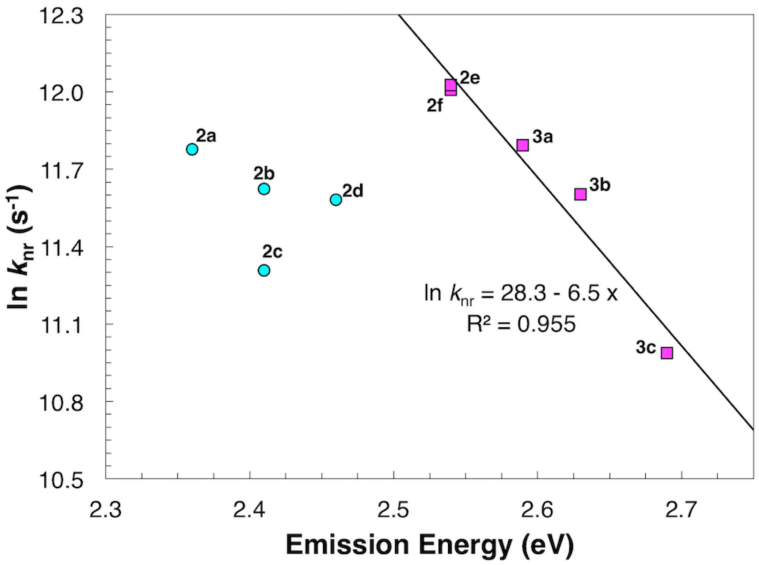

Figure 2-12. Energy gap law correlation of complexes **2a-3c**. Cyan circles indicate complexes with emissions from a mixed MLCT/ILCT. Magenta squares indicate complexes with emissions having higher ILCT character. Differences in excited state character are evident from the vibrational substructure of the luminescence spectra (Figure 2-11) as well as the grouping of these data points. Reprinted from ref 1 with permission. Copyright 2016 American Chemical Society.

Analyzing the electronic structure of the singly occupied molecular orbitals (SOMOs) explains the change in the emission structure and photophysical properties as the complexes increase in fluorination, as well as exchange the chloro ligand to a cyano. As shown in Figure 2-8, **2c** has strong contribution of the iridium center in the electronic

structures of its SOMOs. This high metal character and greater degree of spin-orbit coupling results in an emission from a primarily MLCT, which is also seen in complexes **2b-2d**. In contrast, **3c** has significantly less metal character in the SOMOs, resulting in the emission of **3c** from a predominantly ILCT. The presence of the corresponding transitions in the UV-Vis spectra of the perfluorinated chloro complexes **2e** and **2f,** which are identical to that of the cyano complexes, also supports a similarity in their excited states. The significantly longer excited state lifetime and lower quantum yields in comparison to the other complexes is indicative of this switch in the nature of the excited state. It should also be noted that when the perfluorinated chloride complexes **2e** and **2f** are analyzed their excited states are more in line with the cyanide complexes **3a**-**3c** instead of the other chloride complexes **2a**-**2d**, an observation that is highlighted in Figure 2-12.

DFT calculations have been previously utilized to predict the emission energy of Ir(III) complexes.[26,38,39]One method involves calculating the energy difference of the singlet and triplet excited states at the optimized triplet geometry.[26,39] This method has been successful with structurally diverse sets of iridium (III) complexes, but the dramatic differences in the character of the excited states of **2a-3c** tremendously diminished the accuracy of these predictions (Figure 2-13-B). Instead, if the energy difference between the singlet ground states and triplet excited states at their respective optimized geometries is used, a significant improvement is made in modeling the emission energies, especially given the diversity of excited states within this family of complexes (Figure 2-13-A).[38,39]

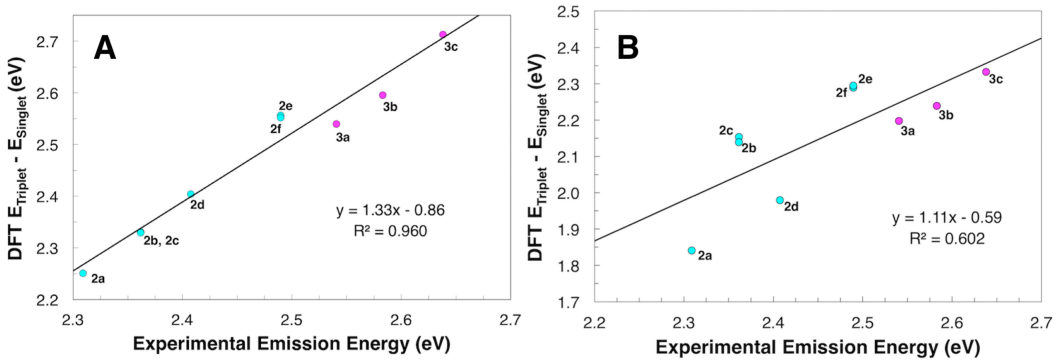

Figure 2-13. DFT prediction of emission energy using (A) the energy difference between the singlet ground and triplet excited states at their respective optimized geometries or (B) the energy difference between the total energies of singlet and triplet excited states at the optimized triplet geometry. Cyan circles indicate the chloro complexes **2a**-**2f** and magenta circles indicate cyano complexes **3a**-**3c**. Reprinted from ref 1 with permission. Copyright 2016 American Chemical Society.

2.3.6 Electrochemical Characterization

To continue to probe the tunability of the complexes, cyclic voltammetry experiments for the complexes were performed in acetonitrile (Table 2-2). All complexes show one oxidation that can be attributed to a metal-centered process with some involvement of the mppy ligand and the ancillary ligand. In the chloride complexes, the oxidation is quasi-reversible (Figure 2-14A), whereas in the cyanide complexes the oxidation is irreversible (Figure 2-14B). Previous complexes from the $[Ir(tpy)(ppy)X]^+$ family have shown up to two oxidations,[9,10,40,41] however none had such a strong of a "push-pull" design as the complexes in this work, which results in increased electron density in the mppy and ancillary ligands. As the complexes become more fluorinated in both the chloride and cyanide complexes, the oxidation potential shifts positively due to stabilization of the HOMO on the mppy and ancillary ligands. In the cases of **2f** and **3c**, the addition of a methoxy group to the pyridine ring of the cyclometallating ligand results in a decrease in the oxidation potential, given its strongly electron donating nature and

participation in the HOMO. The oxidation potential is also shifted positively when the chloride ligand is exchanged for a cyanide, owing to its stronger ligand-field character.

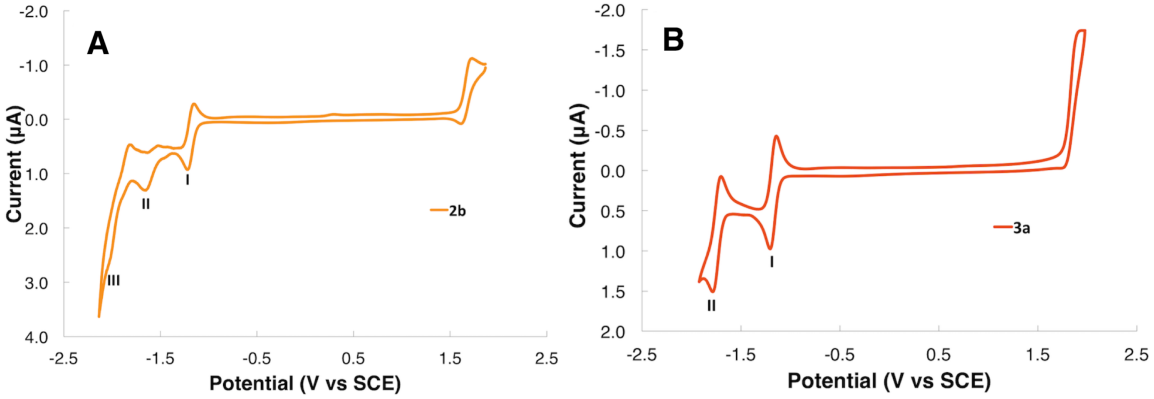

Figure 2-14. Cyclic voltammograms of **2b** (A) and **3a** (B). Roman numerals indicate the unique reductions seen in the complexes. Voltammograms were recorded using argon-degassed 0.10 M tetra-n-butylammonium hexafluorophosphate (acetonitrile) solutions containing 0.5 mM of analyte, at 0.10 V/s with a three-electrode system. All potentials are referenced to SCE using ferrocene as an internal standard (fc/fc^+ = 0.40 V).[28] Adapted from ref. 1 with permission. Copyright 2016 American Chemical Society.

Table 2-2. Electrochemical Properties of "Push-Pull" Complexes.

compound	oxidation E_{pa}/V	reduction **I**: $E_{1/2}$/V (ΔE/mV)	**II:** E_{pc}/V	**III:** E_{red}/V
2a	1.61	-1.23 (45)	-1.69	-2.11
2b	1.70	-1.17 (65)	-1.63	-2.13
2c	1.69	-1.21 (69)	-1.68	-2.17
2d	1.87	-1.18 (38)	-1.62	-1.80
2e	1.88	-1.19 (51)	-1.65	-1.93
2f	1.83	-1.14 (97)	-1.63	-1.91

compound	oxidation E_{pa}/V	reduction **I**: $E_{1/2}$/V (ΔE/mV)	**II**: $E_{1/2}$/V (ΔE/mV)
3a	1.95	-1.17 (68)	-1.74 (83)
3b	1.73 (sh), 2.01	-1.17 (66)	-1.74 (86)
3c	2.00	-1.17 (55)	-1.75 (81)

The first reduction for all complexes occurs on the terpyridine ligand of complexes with the $[Ir(tpy)(ppy)X]^+$ configuration. This reduction is completely

reversible in all complexes studied. While the complexes have the same tri-*tert*-butyl-terpyridine ligand, differences in the first reduction potentials are observed based on changes to the mppy and ancillary ligands. The absence of fluorine atoms in **2a** results in a slightly lower reduction potential compared to the fluorinated analogues. In addition, the position of the fluorine atoms leads to differences in the reduction potential. Complex **2c**, despite having the same degree of fluorination as **2b,** has a noticeably lower reduction potential. This deviation is likely due to the meta- position of the fluorine atom to the cyclometallating carbon in **2c** compared to **2b**. Meanwhile the methoxy group in **2f** increases the first reduction compared to the methyl analogue **2e**, despite both being highly fluorinated. In contrast, the first reduction remains unchanged within the structurally different cyanide complexes **3a-c**.

The second reduction was assigned to the cyclometallating ligand of the Ir complexes. In the chloride complexes **2a-2f**, this reduction is found to be irreversible, whereas it is fully reversible in the cyanide complexes **3a-3c**. Much like the first reduction, the second reduction of **2a** is lower than that of the other complexes within the chloro series. Subsequently **2c**'s second reduction, much like the first reduction, is also lower than its isomer **2b**, despite the same degree of fluorination. The methoxy group of **2f** is responsible for the higher second reduction compared to the methyl analogue **2e**. To contrast, the second reduction observed in the cyanide complexes is nearly unaffected by fluorination. Given that the cyanide ligand has stronger back bonding to the Ir(III) center, dissociation is unlikely. This results in not only making this reduction reversible in the cyano complexes, but also unaffected by mppy fluorination.

A third reduction is only observed in the chloro complexes **2a-2f**, and is related to the dissociation of the chloride ligand. This reduction is irreversible much like the second reduction in the chloro complexes. The loss of the chloride is more difficult as the complexes are substituted by one fluorine, and a small change is again observable in the different mono-fluorinated complexes **2b** and **2c**. However, the complexes with 2 or more fluorine atoms show the loss of the chloride to be significantly easier. Perfluorination seems to increase the third redox potential regardless of the substitution of the pyridine ring. Overall, difluorinated analogue **2d** shows it is the most susceptible to chloride loss.

By using the redox potentials obtained from cyclic voltammetry and the emission maxima of each complex, excited state redox potentials can be determined to better evaluate the photosensitization properties of the complexes (
Table 2-3).[42] While the complexes' excited states are not as strongly reducing as $[Ir(dF(CF_3)ppy)_2(dtbbpy)]PF_6$, a known water reducing catalyst[37] and "push-pull" photosensitizer, or the unsubstituted $[Ir(ppy)_2(bpy)]PF_6$,[43] the complexes are stronger oxidants when excited.

Table 2-3. Calculated Excited State Redox Potentials of "Push-Pull Complexes".

compound	E ($[M^*]^+/[M]^{2+}$)/V[a,b]	E ($[M^*]^+/[M]^0$)/V[a,c]
2a	-0.70	1.07
2b	-0.66	1.19
2c	-0.67	1.15
2d	-0.54	1.22
2e	-0.61	1.30
2f	-0.66	1.35
3a	-0.59	1.37
3b	-0.57	1.42
3c	-0.64	1.47
$[Ir(ppy)_2(bpy)]PF_6$[43]	-0.85	0.68
$[Ir(dF(CF_3)ppy)_2(dtbbpy)]PF_6$[37]	-0.89	1.21

Potentials are given in V vs SCE. [b] $E([M^*]^+/[M]^{2+}) = E_{ox} - E_{\lambda em}$. [c] $E([M^*]^+/[M]^0) = E_{red} + E_{\lambda em}$.[42]

2.3.7 Photocatalytic Hydrogen Evolution

With the enhanced electrochemical stability of the complexes and the enhanced photophysical properties, the complexes were subsequently evaluated as photosensitizers for photocatalytic hydrogen evolution from water. The reactions were carried out in a mixed acetonitrile/water solvent using K_2PtCl_4 as the water reducing catalyst and triethylamine as the sacrificial donor based upon established protocols.[33] Photocatalytic activity was also determined against the original "push-pull" complex developed in our lab, [Ir(dMeO-phtpy)(4'-Fmppy)Cl]PF_6 [10].

Based on the hydrogen evolution traces in Figure 2-15, the new complexes had a wide range of photosensitizing ability. Complex **3b** was the best performer, outperforming [Ir(dMeOphtpy)(4-Fmppy)Cl]PF_6. Complex **3b**'s more dramatic push-pull structure, higher luminescence quantum yield over [Ir(dMeO-phtpy)(4'-Fmppy)Cl]PF_6 (25.2 % vs 61.8 % for **3b**), and possession of the stronger field, less labile cyanide ligand are contributing factors to this enhanced performance. The trends for the chloride compounds (**2a**-**2f**) indicates increasing fluorination leads to decreasing photosensitizing ability. This can be rationalized as complexes with less electron-withdrawing cyclometalating ligands had increased metal character in their excited states. The cyano complexes **3a**-**3c** followed a similar trend where metal character in the excited state as well as higher k_{nr}/k_r ratio and consequently luminescence quantum yield, correlated to increased hydrogen production. Comparisons between the chloride and cyanide series of complexes are complicated given the changing nature of the excited state from a mixed MLCT/ILCT in the chloride series to an almost purely ILCT in the cyanide series. It

should be noted that compounds **2e**, **2f**, and **3a** all had very similar excited state properties and performed comparably in photocatalytic hydrogen evolution studies.

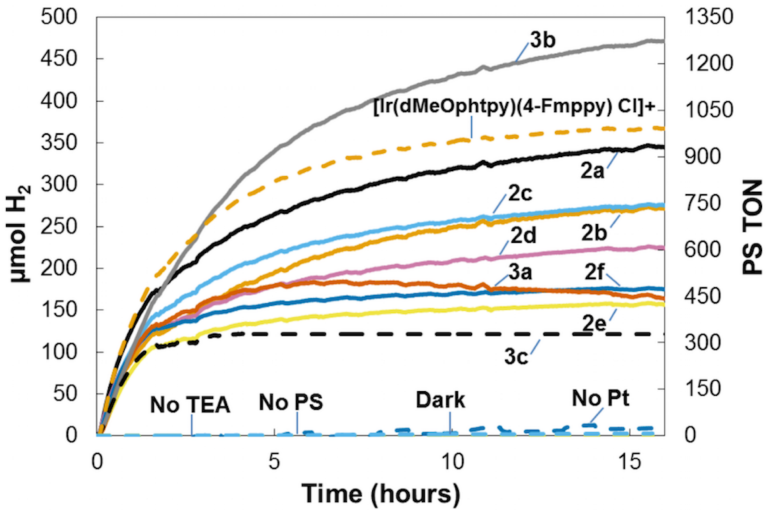

Figure 2-15. Photocatalytic hydrogen evolution traces of complexes **2a-3c**. Quantities of hydrogen evolved are noted along with the TON of the Ir(III) photosensitizers. Figure produced by Isaac Mills and reprinted from ref. 1 with permission. Copyright 2016 American Chemical Society.

2.3.8 Photoredox Catalysis

Complexes **2b** and **3a** were evaluated as photosensitizers for the photocatalytic decarboxylative fluorination of carboxylic acids (Scheme 2-5). Previous studies have shown that $[Ir(ppy)_2(bpy)]^+$ based complexes can serve as photosensitizers for several organic transformations.[44-48] Mechanistically, the photocatalytic decarboxylative fluorination reaction is similar to photocatalytic hydrogen evolution (Figure 2-16). Much like photocatalytic water reduction, photocatalytic decarboxylative fluorination relies on the photogeneration of a highly reducing *Ir(III) species, which upon oxidative quenching with an electron acceptor, produces a transient Ir(IV) species. This can go on to react with a deprotonated carboxylic acid to generate CO_2 , the now regenerated Ir(III) photocatalyst, and a radical species that proceeds to react with the fluorine source Selectfluor.[34] Given that **2a** and **3b** were proven to generate hydrogen from water

photocatalytically, their use as photosensitizers for the photocatalytic decarboxylative fluorination was a logical direction to pursue.

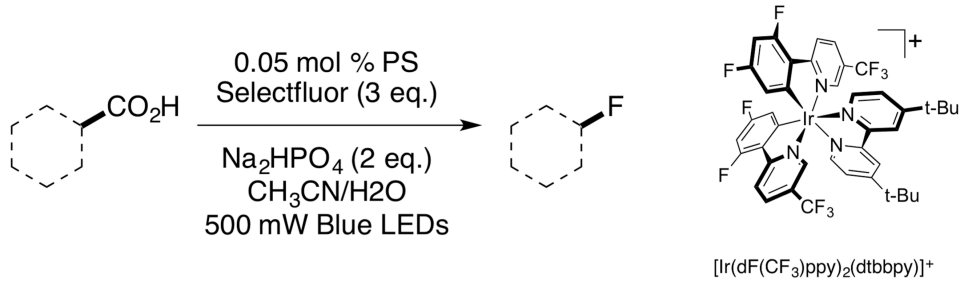

Scheme 2-5. Decarboxylative Fluorination of Carboxylic Acids and structure of $[Ir(dF(CF_3)ppy)_2(dtbbpy)]^+$.

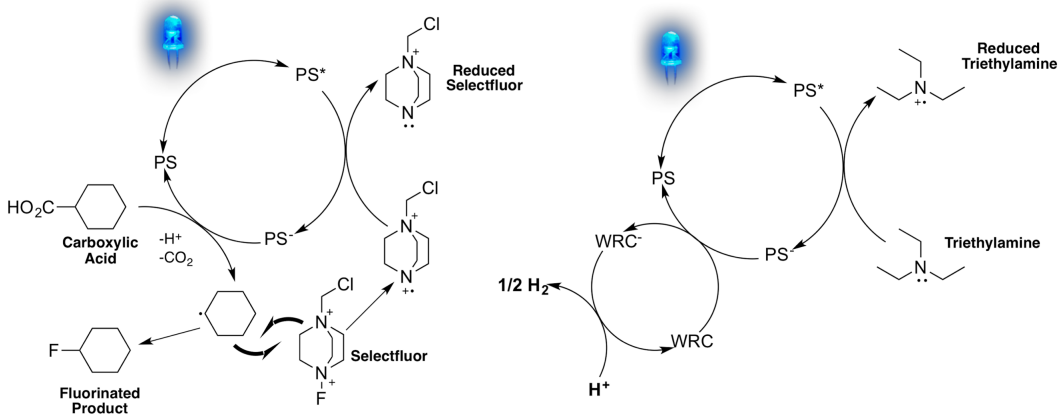

Figure 2-16. Mechanistic similarities between decarboxylative fluorination (proposed by Ventre et. al.[34]) and photocatalytic hydrogen evolution (proposed by Tinker et. al.[2]).

The performances of **2b**, **3a**, and the cited best photosensitizer for the transformation, $[Ir(dF(CF_3)ppy)_2(dtbbpy)]PF_6$,[34] were evaluated using the five carboxylic acids shown in Table 2-4. MacMillan's original protocol called for a 1 mol % photosensitizer loading. However, to better evaluate if **2b** and **3a** were more stable in the highly coordinating solvent of the reaction (3:1 acetonitrile/water), a concentration study with **2b** was performed (Figure 2-17). Up to a 100-fold reduction of photosensitizer still gave comparable performance based on CO_2 evolution. For the subsequent evaluation of the substrates, a twenty-fold reduced photosensitizer loading of 0.05 mol % for all three

complexes was used. Reaction yields were determined by ^{19}F NMR using hexafluorobenzene as an internal standard. NMR signals of the products matched those reported in the literature (fluorodiphenylmethane,[45] 1-(fluoromethyl)-naphthalene,[46] fluorocyclohexane,[47] 4-(fluoromethyl)-1,1'-biphenyl and 2-fluoroethane-1,1,1-triyl)tribenzene[34]). Control reactions which omitted catalyst, base, and light did not generate the fluorinated products.

Table 2-4. Photosensitizer and Substrate Studies of the Decarboxylative Fluorination Reaction. Yields determined by ^{19}F NMR with C_6F_6 as an internal standard.

		yield (%)		
R-CO_2H	R-F	**2b**	**3a**	[Ir(dF(CF_3)ppy)$_2$ (dtbbpy)]PF_6
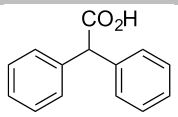	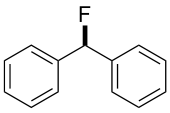	58	57	44
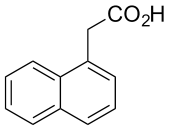	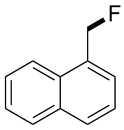	37	41	40
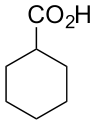	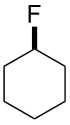	10	13	3
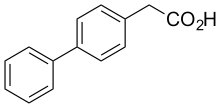	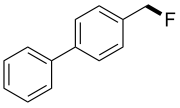	99	63	4
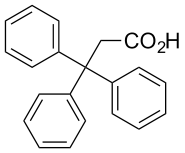	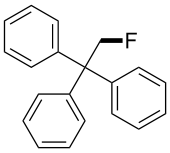	61	57	23

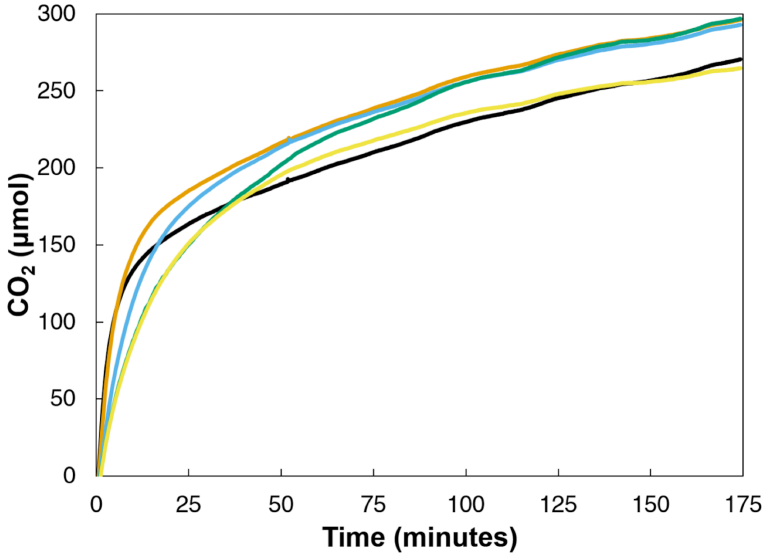

Figure 2-17. CO_2 evolution traces using **2b** with diphenylacetic acid at varying catalyst concentrations. 0.1 mol % (black), 0.05 mol % (orange), 0.025 mol % (blue), 0.0125 mol % (green), 0.010 mol % (yellow). Reprinted from ref. 1 with permission. Copyright 2016 American Chemical Society.

The yields for the reactions with **2b** and **3a** were comparable to each other in most cases, while the yields of $[Ir(dF(CF_3)ppy)_2(dtbbpy)]PF_6$ under the same reaction conditions were noticeably lower. In most cases, complexes **2b** and **3a** were shown to outperform the reaction yields of $[Ir(dF(CF_3)ppy)_2(dtbbpy)]PF_6$ at the new loadings. It would appear that the decrease in loading from 1 mol % to 0.05 mol % had a more dramatic effect on the performance of the reactions with $[Ir(dF(CF_3)ppy)_2(dtbbpy)]PF_6$. This can be rationalized by the differences in the ligand structures. The terpyridine-phenylpyridine structure imparted significantly greater stability than the traditional $[Ir(ppy)_2(bpy)]^+$ design, which is known to be degrade in highly coordinating solvents including acetonitrile over extended periods of time.[2,3] It's also worth noting the excited state lifetimes of **2b** and **3a** (3.17 µs and 3.35 µs respectively) are both longer than $[Ir(dF(CF_3)ppy)_2(dtbbpy)]PF_6$ (2.3 µs),[37] which allows greater time for the photoinduced transfer of electrons necessary for the transformation. While it has been shown through

electrochemical experiments that the cyano complexes are more stable than the chloro analogues, this does not account for instances where the performances of **2b** are significantly greater than that of **3a** specifically, 4-biphenylacetic acid. Instead, the difference in the excited state oxidation potentials of the complexes could explain the difference in reactivity, specifically **2b** being less oxidizing than **3a**. A future optimization strategy could involve analysis of the electrochemistry of the carboxylates to optimize the redox potentials of the photosensitizer to that of the carboxylic acid.

2.4 Conclusions

A series of new Ir(III) luminophores using the $[Ir(tpy)(ppy)X]^+$ ligand framework were synthesized using C-F to generate a family of "push-pull" complexes. The synthesis was accomplished using symmetrical, fluorinated phenylpyridine ligands which preferentially activated C-F bonds, with trace formation of the C-H activation products. The addition of strongly electron-donating *tert*-butyl groups to the terpyridine ligand tuned the LUMO of the complexes, whereas variation in the degree of fluorination of the cyclometallating ligand and exchange of the ancillary ligand successfully tuned the HOMO, as made evident by computational, photophysical, and electrochemical studies. This combination resulted in significant improvements in the photochemical performances of the complexes, marked by higher quantum yields and longer excited state lifetimes. A change in the nature of the excited state was observed, gradually increasing in ILCT character and decreasing the MLCT character as more fluorine was used on the mppy ligand. This resulted in mixed performances of the complexes as photosensitizers for the photocatalytic hydrogen evolution reaction compared to previous compounds, but nonetheless still impressive given the highly coordinating conditions.

When used as a photosensitizer for the decarboxylative fluorination of several carboxylic acids, two of the complexes outperformed the state of the art photosensitizer for the reaction. Given the improvements imparted by the "push-pull" design of the complexes, future work in implementing these compounds into applications where characteristics such as high quantum efficiencies and photochemical stability are highly desirable should be explored. Furthermore, given the C-F insertion preference, additional reactions using other halogens (Cl, Br, I) could be performed. These reactions could determine if ancillary ligand exchange can be possible through C-X insertion or by using a mixed halogen mppy ligand, establish preferences of one halogen over another for the C-X insertion process.

2.5 References

(1) Porras, J. A.; Mills, I. N.; Transue, W. J.; Bernhard, S. *J. Am. Chem. Soc.* **2016**, *138*, 9460–9472.
(2) Tinker, L. L.; McDaniel, N. D.; Curtin, P. N.; Smith, C. K.; Ireland, M. J.; Bernhard, S. *Chem. Eur. J.* **2007**, *13*, 8726–8732.
(3) Curtin, P. N.; Tinker, L. L.; Burgess, C. M.; Cline, E. D.; Bernhard, S. *Inorg. Chem.* **2009**, *48*, 10498–10506.
(4) Tinker, L. L.; Bernhard, S. *Inorg. Chem.* **2009**, *48*, 10507–10511.
(5) Mamo, A.; Stefio, I.; Parisi, M. F.; Credi, A.; Venturi, M.; Di Pietro, C.; Campagna, S. *Inorg. Chem.* **1997**, *36*, 5947–5950.
(6) Whittle, V. L.; Williams, J. A. G. *Inorg. Chem.* **2008**, *47*, 6596–6607.
(7) Polson, M.; Fracasso, S.; Bertolasi, V.; Ravaglia, M.; Scandola, F. *Inorg. Chem.* **2004**, *43*, 1950–1956.
(8) Polson, M.; Ravaglia, M.; Fracasso, S.; Garavelli, M.; Scandola, F. *Inorg. Chem.* **2005**, *44*, 1282–1289.
(9) Sato, S.; Morikawa, T.; Kajino, T.; Ishitani, O. *Angew. Chem. Int. Ed.* **2013**, *52*, 988–992.
(10) Chirdon, D. N.; Transue, W. J.; Kagalwala, H. N.; Kaur, A.; Maurer, A. B.; Pintauer, T.; Bernhard, S. *Inorg. Chem.* **2014**, *53*, 1487–1499.
(11) Tordera, D.; Bunzli, A. M.; Pertegas, A.; Junquera-Hernandez, J. M.; Constable, E. C.; Zampese, J. A.; Housecroft, C. E.; Orti, E.; Bolink, H. J. *Chem. Eur. J.* **2013**, *19*, 8597–8609.
(12) Constable, E. C.; Ertl, C. D.; Housecroft, C. E.; Zampese, J. A. *Dalt. Trans.* **2014**, *43*, 5343–5356.
(13) Coppo, P.; Plummer, A.; Cola, L. De. *Chem Comm* **2004**, 1774–1775.

(14) Grushin, V. V; Herron, N.; LeCloux, D. D.; Marshall, W. J.; Petrov, V. a; Wang, Y. *Chem. Commun.* **2001**, 1494–1495.
(15) Takizawa, S. Y.; Nishida, J. I.; Tsuzuki, T.; Tokito, S.; Yamashita, Y. *Inorg. Chem.* **2007**, *46*, 4308–4310.
(16) Xu, M.; Zhou, R.; Wang, G.; Xiao, Q.; Du, W.; Che, G. *Inorg. Chim. Acta* **2008**, *361*, 2407–2412.
(17) Liu, C.; Lv, X.; Xing, Y.; Qui, J. *J. Mater. Chem. C* **2015**, *3*, 8010–8017.
(18) Li, H.-Y.; Li, T.; Teng, M.; Xu, Q.; Zhang, S.; Jin, Y.; Liu, X.; Zheng, Y.-X.; Zuo, J.-L. *J. Mater. Chem. C* **2014**, *2*, 1116–1124.
(19) Li, H.; Zhou, L.; Teng, M.; Xu, Q.; Lin, C.; Zheng, Y.; Zuo, J.; Zhang, H.; You, X. *J. Mater. Chem. C* **2013**, *1*, 560–565.
(20) Shavaleev, N. M.; Xie, G.; Varghese, S.; Cordes, D. B.; Slawin, A. M. Z.; Momblona, C.; Ort, E.; Bolink, H. J.; Samuel, I. D. W.; Zysman-colman, E. *Inorg. Chem.* **2015**, *54*, 5907–5914.
(21) Shavaleev, N. M.; Monti, F.; Scopelliti, R.; Armaroli, N.; Grätzel, M.; Nazeeruddin, M. K. *Organometallics* **2012**, *31*, 6288−6296.
(22) Mills, I. N.; Kagalwala, H. N.; Chirdon, D. N.; Brooks, A. C.; Bernhard, S. *Polyhedron* **2014**, *82*, 104–108.
(23) Mills, I. N.; Kagalwala, H. N.; Bernhard, S. *Dalton Trans.* **2016**, *45*, 10411–10419.
(24) Niu, Z. G.; Liu, D.; Li, D. C.; Zuo, J.; Yang, J. M.; Su, Y. H.; Yang, Y. D.; Li, G. N. *Inorg. Chem. Commun.* **2014**, *43*, 146–150.
(25) Lee, S.; Kim, S.-O.; Shin, H.; Yun, H.-J.; Yang, K.; Kwon, S.-K.; Kim, J.-J.; Kim, Y.-H. *J. Am. Chem. Soc.* **2013**, *135*, 14321–14328.
(26) Lowry, M. S.; Hudson, W. R.; Pascal, R. A.; Bernhard, S. *J. Am. Chem. Soc.* **2004**, *126*, 14129–14135.
(27) Do, H.-Q.; Daugulis, O. *J. Am. Chem. Soc.* **2008**, *130*, 1128–1129.
(28) Connelly, N. G.; Geiger, W. E. *Chem. Rev.* **1996**, *96*, 877–910.
(29) Gaussian 09, Revision D.01, M. J. Frisch, G. W. Trucks, H. B. Schlegel, G. E. Scuseria, M. A. Robb, J. R. Cheeseman, G. Scalmani, V. Barone, G. A. Petersson, H. Nakatsuji, X. Li, M. Caricato, A. Marenich, J. Bloino, B. G. Janesko, R. Gomperts, B. Mennucci, H. P. Hratchian, J. V. Ortiz, A. F. Izmaylov, J. L. Sonnenberg, D. Williams-Young, F. Ding, F. Lipparini, F. Egidi, J. Goings, B. Peng, A. Petrone, T. Henderson, D. Ranasinghe, V. G. Zakrzewski, J. Gao, N. Rega, G. Zheng, W. Liang, M. Hada, M. Ehara, K. Toyota, R. Fukuda, J. Hasegawa, M. Ishida, T. Nakajima, Y. Honda, O. Kitao, H. Nakai, T. Vreven, K. Throssell, J. A. Montgomery, Jr., J. E. Peralta, F. Ogliaro, M. Bearpark, J. J. Heyd, E. Brothers, K. N. Kudin, V. N. Staroverov, T. Keith, R. Kobayashi, J. Normand, K. Raghavachari, A. Rendell, J. C. Burant, S. S. Iyengar, J. Tomasi, M. Cossi, J. M. Millam, M. Klene, C. Adamo, R. Cammi, J. W. Ochterski, R. L. Martin, K. Morokuma, O. Farkas, J. B. Foresman, and D. J. Fox, Gaussian, Inc., Wallingford CT, 2016.
(30) Hanwell, M. D.; Curtis, D. E.; Lonie, D. C.; Vandermeersch, T.; Zurek, E.; Hutchison, G. R. *J. Cheminform.* **2012**, *4*, 17.
(31) O'Boyle, N. M.; Tenderholt, A. L.; Langner, K. M. *J. Comp. Chem.* **2008**, *29*, 839–845.
(32) Caspar, J. V; Meyer, T. J. *J. Am. Chem. Soc.* **1983**, *105*, 5583–5590.

(33) Cline, E. D.; Adamson, S. E.; Bernhard, S. *Inorg. Chem.* **2008**, *47*, 10378–10388.
(34) Ventre, S.; Petronijevic, F. R.; Macmillan, D. W. C. *J. Am. Chem. Soc.* **2015**, *137*, 5654–5657.
(35) Hartman, J. S.; Shoemaker, J. A. W.; Janzen, A. F.; Ragogna, P. J.; Szerminski, W. R. R. *J. Fluor. Chem.* **2003**, *119*.
(36) Hartmeyer, G.; Marichal, C.; Lebeau, B.; Caullet, P.; Hernandez, J. *J. Phys. Chem. C* **2007**, *111*, 6634–6644.
(37) Lowry, M. S.; Goldsmith, J. I.; Slinker, J. D.; Pascal, R. A.; Malliaras, G. G.; Bernhard, S.; Rohl, R. *Chem Mater* **2005**, *17*, 5712–5719.
(38) Ladouceur, S.; Fortin, D.; Zysman-colman, E. *Inorg. Chem.* **2011**, *50*, 11514–11526.
(39) Donato, L.; Abel, P.; Zysman-Colman, E. *Dalton Trans.* **2013**, *42*, 8402–8412.
(40) Reithmeier, R. O.; Meister, S.; Rieger, B.; Siebel, A.; Tschurl, M.; Heiz, U.; Herdtweck, E. *Dalton Trans.* **2014**, *43*, 13259–13269.
(41) Reithmeier, R. O.; Meister, S.; Siebel, A.; Rieger, B. *Dalton Trans.* **2015**, *44*, 6466–6472.
(42) Kalyanasundaram, K. *Photochemistry of Polypyridine and Porphyrin Complexes*; Academic Press: New York, 1992.
(43) Goldsmith, J. I.; Hudson, W. R.; Lowry, M. S.; Anderson, T. H.; Bernhard, S. *J. Am. Chem. Soc.* **2005**, *127*, 7502–7510.
(44) Prier, C. K.; Rankic, D. A.; MacMillan, D. W. C. *Chem. Rev.* **2013**, *113*, 5322–5363.
(45) Johnson, A. L. *J. Org. Chem.* **1982**, *47*, 5220–5222.
(46) Blessley, G.; Holden, P.; Walker, M.; Brown, J. M.; Gouverneur, V. *Org. Lett.* **2012**, *14*, 2754–2757.
(47) Xia, J.-B.; Zhu, C.; Chen, C. *Chem. Commun.* **2014**, *50*, 11701–11704.

Chapter 3. Long Lived $[Ir(tbudqp)(ppy)X]^+$ Photosensitizers

This chapter will be adapted into a manuscript for publication. Additional synthetic data forthcoming.

3.1 Introduction

As highlighted in Chapter 2, while $[Ir(ppy)_2(bpy)]^+$ based complexes are highly versatile given their ease of tunability and functionalization of their ligand framework, but still suffer from photodegradation regardless of the application. Improved stability has been achieved with switching the labile bipyridine ligand with a more stable terpyridine ligand to generate the $[Ir(tpy)(ppy)X]^+$ structure, allowing the complexes to have higher turnover numbers for water reduction,[1,2] as well as have a vacant site for photocatalytic CO_2 reduction.[3–6] While great success has been achieved using terpyridine ligands, there is little exploration into other tridentate ligands that could be used with the $[Ir(N^N^N)(C^N)X]^+$ ligand structure to further diversify the applications of the complexes. To date, only work by Obara *et. al.* has used bis(N-methyl-2-benzimidazolyl)pyridine (Mebip) to generate $[Ir(Mebip)(ppy)Cl]^+$.[7] However, the photophysical tunability was not explored and there were complications with the ligand synthesis whereby binding sites on the imidazole required blocking to minimize isomer formation (Figure 3-1).

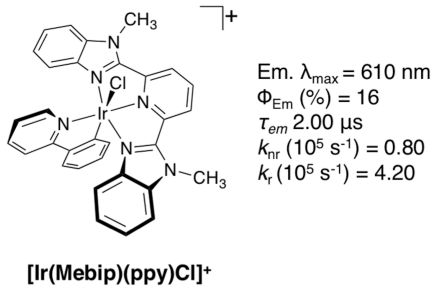

Figure 3-1. Structure and photophysical properties of $[Ir(Mebip)(ppy)Cl]^+$ generated by Obara *et. al*.[7]

Upon review of the literature, a promising strategy for generating a new tridentate ligand was found when Ru(II) complexes were the target. $[Ru(bpy)_3]^{2+}$, much like $[Ir(ppy)_2(bpy)]^+$ has also been shown to suffer from photodegradation by loss of a bipyridine ligand. It was hypothesized that by making the switch to $[Ru(tpy)_2]^{2+}$, enhancement of the complex's stability could be achieved. However, the performance actually drops dramatically due to the ease of deactivation of short-lived metal-centered states that were thermally populated from a ^{3}MLCT state.[8] As such, efforts to improve the photophysical properties are of value. One strategy involved increasing the ligand field energy of the complex to prevent access to the metal-centered states by making the complex octahedral. Work by Abrahamsson et. al. added a methylene bridge to generate $[Ru(pbpy)_2]^{2+}$,[9] along with other bridges,[10] to the terpyridine which allows coordination in a more optimal octahedral arrangement, and modestly improved their photophysical properties. This strategy was taken a step further by Abrahamsson *et. al.* when they added additional rigidity to the ligand by using bis(quinolyl)pyridine (bqp), which resulted in a 3.0 μs excited state lifetime (Figure 3-2)![11] Further work demonstrated that the 4-position of the pyridine ring could be functionalized to modulate the electrochemical and photophysical properties of the complexes.[12–14] Given the success of the bqp ligand with Ru(II), it was envisioned that it's use with the already promising $[Ir(N^N^N)(C^N)X]^+$ structure would only further improve the properties of the corresponding Ir(III) complexes.

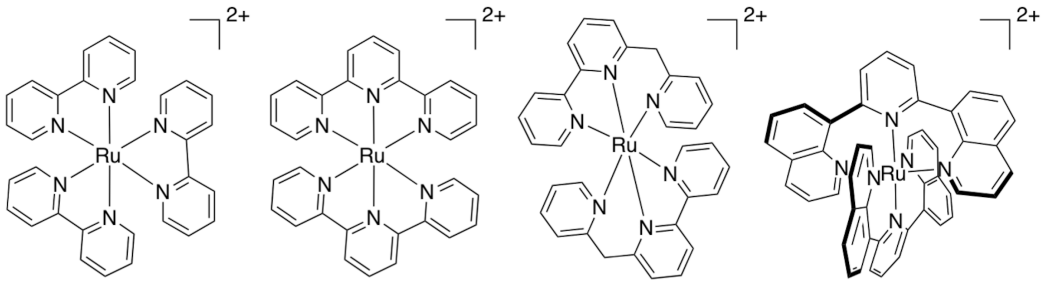

Figure 3-2. Ru(II) polypyridyl complexes and their photophysical properties.[9,11]

This chapter presents a series of Ir(III) complexes that utilize the established $[Ir(N^N^N)(C^N)X]^+$ structure with a newly synthesized tbudqp ligand. The complexes have varying degrees of fluorination on the cyclometallating ligand, as well as a chloride or cyanide ancillary ligand to assess their impacts of the ligands on the photophysical, electrochemical, and catalytic properties of the complexes. DFT calculations further corroborate the effects of the ligands on the electronic structure of the complexes. Subsequently, evaluation for a variety of photocatalytic applications was performed including photocatalytic hydrogen generation from water, photosensitizers for the decarboxylative fluorination of carboxylic acids, and for the photogeneration of singlet oxygen.

3.2 Experimental

3.2.1 General

The Ir(III) precursor $IrCl_3 \cdot 4H_2O$, and all solvents were used as received from commercial sources. Ligand precursor 8-acetylquinoline was synthesized according to the procedure from Wang et. al.[15] The ligands mppy, 4-Fmppy, and 2,4,6-tFmppy were prepared from the corresponding acyl-pyridinium salts as described by Lowry et. al.[16] The ligand

PFmppy was prepared using the procedure described by Do et. al.[17] ^{1}H, ^{13}C, and ^{19}F NMR spectra were obtained using Bruker Avance 300 MHz and 500 MHz spectrometers. ^{1}H and ^{13}C NMR spectra were referenced to residual solvent signals. ^{19}F NMR spectra were referenced to $CFCl_3$ by using the PF_6 anion (-71.11 ppm, doublet) as an internal standard. ESI-MS was performed with 50 μM methanol solutions using a Thermo-Fisher LCQ instrument.

3.2.2 Synthetic Procedures

Synthesis of tbudqp. To an oven dried 200 mL, one-neck, round-bottom flask sealed with a rubber septa and purged with argon was added dry THF (100 mL) followed by a solution of $KO^{t}Bu$ in THF (16 mL of a 1.66 M soln., 26.66 mmol). A solution of 8-acetylquinoline (4.561 g, 26.66 mmol) in THF (25 mL) was added via syringe and the solution became cloudy and yellow. After 5 minutes of stirring, pivaldehyde (1.481 g, 13.33 mmol) was added and the solution became bright orange. The solution was left to stir overnight under a positive pressure of argon. The following day, a 500 mL, one-neck, round bottom flask was charged with acetic acid (130 mL) and ammonium acetate (20.554 g, 266.66 mmol). The THF solution was poured into the 500-mL flask. A condenser was fitted and the reaction was purged under argon before refluxing for 6 hours, at which point the reaction became dark brown. After cooling, the solvents were removed and the reaction was suspended in 6M HCl, which was extracted five times with dichloromethane. The aqueous phase was neutralized with solid sodium carbonate and subsequently extracted 4 times with dichloromethane. After removal of the solvents, the crude product was passed through a short silica gel plug using 40% ethyl acetate in dichloromethane to provide 1.403 g of product as a brown oil (27 % yield). ^{1}H NMR (300

MHz, $CDCl_3$) δ 8.92 (dd, *J* = 4.1, 1.8 Hz, 2H), 8.21 – 8.09 (m, 4H), 8.02 (s, 2H), 7.78 (dd, *J* = 8.1, 1.3 Hz, 2H), 7.64 – 7.53 (m, 2H), 7.35 (dd, *J* = 8.3, 4.2 Hz, 2H), 1.40 (s, 9H). ^{13}C NMR (75 MHz, $CDCl_3$) δ 158.46, 156.63, 150.22, 146.12, 139.86, 136.47, 131.59, 128.76, 128.43, 126.66, 123.07, 121.02, 77.36, 35.13, 30.86. MS (*m/z* ESI, MeOH) Calculated: 390.2 $[M+H]^+$ Found: 390.3.

*Synthesis of Ir(tbudqp)Cl₃ (**1a**).* In a 40 mL EPA vial, $IrCl_3 \bullet 4H_2O$ (386 mg, 1.04 mmol), tbudqp (386 mg, 0.99 mmol) and a stirbar were purged with argon for 15 minutes before injecting 13 mL of ethylene glycol. The vessel was purged with argon for an additional 10 minutes before stirring at 170 °C, in a pre-heated aluminum heating block, for 22 minutes, in the dark. Once cooled, an orange precipitate was collected on a Büchner funnel, after washing with water, ethanol, and diethyl ether. The filtrates were then extracted five times with chloroform, dried with sodium sulfate, and reduced to a quarter of the original volume. An excess of diethyl ether was added to further precipitate product, which was isolated via vacuum filtration and washed with diethyl ether. Combined yield: 432 mg (63%). Concentrations necessary for ^1H NMR and ^{13}C NMR could not be obtained due to poor solubility in DMSO-d_6.

*Synthesis of [Ir(tbudqp)(mppy)Cl]PF₆ complexes **2a-2d**.* In a typical reaction, [Ir(tBudqp)Cl_3] (50 mg, 0.073 mmol), cyclometallating ligand (0.219 mmol, 3.00 eq.), and a stirbar were placed together in a 40 mL EPA vial. The vessel was degassed with argon for 15 minutes before injecting 13 mL of ethylene glycol, and the vessel was degassed for another 10 minutes with argon. The vessel was heated to 183 °C in a preheated aluminum block, in the dark, for 16-20 hours. Once cooled to room temperature, the reaction was diluted with 15 mL of water and filtered through Celite®,

and it was rinsed with another 10 mL of water. The filtrate was poured into a 125 mL separatory funnel and the water/ethylene glycol mixture was extracted 5 x 25 mL with diethyl ether, using ethanol to combat the formation of emulsions in certain cases. The water/glycol layer was transferred to a 125 mL Erlenmeyer flask and placed in a 40 ^{o}C water bath to evaporate any residual ether. The water/glycol layer was stirred with 300 mg of KPF_6 for 1 hour before isolating the complex on a Büchner funnel, washing with water and diethyl ether. The complexes were then dissolved in acetonitrile and purified by vapor diffusion with diethyl ether.

[Ir(tbudqp)(mppy)Cl](PF$_6$) (**2a**). Yield: 50%. ^{1}H NMR (500 MHz, Acetone-d_6) δ 9.27 (s, 1H), 8.87 (d, J = 7.4 Hz, 2H), 8.57 (d, J = 8.1 Hz, 2H), 8.39 (s, 2H), 8.23 (d, J = 8.0 Hz, 2H), 8.15 – 8.02 (m, Hz, 2H), 7.98 (d, J = 8.3 Hz, 1H), 7.96 – 7.86 (m, 3H), 7.54 (d, J = 7.6 Hz, 1H), 7.28 (dd, J = 8.1, 5.5 Hz, 2H), 7.01 (d, J = 7.5 Hz, 1H), 6.79 (dt, J = 31.4, 7.2 Hz, 2H), 2.43 (s, 3H), 1.62 (s, 9H). ^{19}F NMR (470.54 MHz, acetone-d_6): δ -71.11 (d, J = 707.65 Hz, [PF_6^-]). MS (*m/z* ESI, MeOH) Calculated: 785.4 [M-PF_6^-]$^+$ Found: 785.1.

[Ir(tBudqp)(4-Fmppy)Cl](PF$_6$) **(2b)**. Yield: 29%. δ ^{1}H NMR (500 MHz, Acetone-d_6) δ 9.22 (s, 1H), 8.94 – 8.86 (m, 2H), 8.58 (d, J = 8.0 Hz, 2H), 8.40 (s, 2H), 8.24 (d, J = 8.1 Hz, 2H), 8.20 – 7.96 (br m, 2H), 7.97 – 7.86 (m, 4H), 7.62 (dd, J = 8.6, 5.6 Hz, 1H), 7.28 (dd, J = 8.2, 5.4 Hz, 2H), 6.66 – 6.57 (m, 2H), 2.41 (s, 3H), 1.61 (s, 9H). ^{19}F NMR (470.54 MHz, acetone-d_6): δ -71.11 (d, J = 707.50 Hz, [PF_6^-]), -109.54 (s, 1F). MS (*m/z* ESI, MeOH) Calculated: 803.4 [M-PF_6^-]$^+$ Found: 803.1.

[Ir(tBudqp)(2,4-dFmppy)Cl](PF$_6$) **(2c)**. Yield: 20%. ^{1}H NMR (500 MHz, Acetone-d_6) δ 9.31 (s, 1H), 8.89 (d, J = 6.6 Hz, 2H), 8.61 (d, J = 7.6 Hz, 2H), 8.41 (s, 2H), 8.26 (d, J = 8.1 Hz, 2H), 8.22 – 8.00 (br m, 3H), 8.00 – 7.91 (m, 3H), 7.41 (dd, J = 8.2, 5.5 Hz, 1H), 7.30 (dd, J = 8.2, 5.4 Hz, 2H), 6.59 – 6.47 (m, 2H), 2.43 (s, 3H), 1.61 (s, 10H). ^{19}F NMR (470.54 MHz, acetone-d_6): δ -71.11 (d, J = 707.79 Hz, [PF_6^-]), -107.00 (d, J = 10.02 Hz, 1F), -108.55 (d, J = 10.02 Hz, 1F). MS (*m/z* ESI, MeOH) Calculated: 821.4 [M-PF_6^-]$^+$ Found: 821.1.

[Ir(tBudqp)(PFmppy)Cl](PF$_6$) **(2d)**. Yield: 47%. ^{1}H NMR (500 MHz, Acetone-d_6) δ 9.29 (s, 1H), 8.87 (d, J = 7.3 Hz, 2H), 8.66 (d, J = 8.1 Hz, 2H), 8.37 – 8.26 (m, 4H), 8.25 – 8.01 (br m, 4H), 7.97 (t, J = 7.6 Hz, 2H), 7.31 (dd, J = 8.2, 5.4 Hz, 2H), 2.45 (s, 3H), 1.59 (s, 9H). ^{19}F NMR (470.54 MHz, acetone- d_6): δ -71.11 (d, J = 707.50 Hz, [PF_6^-]), -128.42 (dd, J = 25.2, 14.8 Hz, 1F), -138.48 (ddd, J = 20.0, 15.0, 5.3 Hz, 1F), -153.00 (ddd, J = 24.5, 18.8, 5.3 Hz, 1F), -162.26 (t, J = 19.2 Hz, 1F). MS (*m/z* ESI, MeOH) Calculated: 857.4 [M-PF_6^-]$^+$ Found: 857.1.

*Synthesis of [Ir(tbudqp)(mppy)CN]PF$_6$ complexes **3a-3d**.* In a typical reaction, [Ir(tbudqp)Cl_3] (50 mg, 0.073 mmol), cyclometallating ligand (0.219 mmol, 3.00 eq.), and a stirbar were placed together in a 40 mL EPA vial. The vessel was degassed with argon for 15 minutes before injecting 13 mL of ethylene glycol, and the vessel was degassed for another 10 minutes with argon. The vessel was heated to 183 ^{o}C in a preheated aluminum block, in the dark, for 16-20 hours. The vessel was cooled to room temperature in the dark, and the heating block was cooled to 90 ^{o}C. The vessel was

heated to 90 ^{o}C in the aluminum block and an aqueous solution of KCN (19 mg, 0.292 mmol, 4 eq. in 1 mL of water) was injected and left to stir for 2 hours. Once cooled to room temperature, the reaction was diluted with 10 mL of water and 5 mL of ethanol and filtered through Celite®, and it was rinsed with 5 mL of water and 5 mL of ethanol. The filtrate was poured into a 125 mL separatory funnel and the water/ethylene glycol mixture was extracted 5 x 25 mL with diethyl ether, using ethanol to combat the formation of emulsions in certain cases. The water/glycol layer was transferred to a 125 mL Erlenmeyer flask and placed in a 40 ^{o}C water bath to evaporate any residual ether. The water/glycol layer was stirred with 300 mg of KPF_6 for 1 hour before isolating the complex on a Büchner funnel, washing with water and diethyl ether. The complexes were then dissolved in acetonitrile and purified by vapor diffusion with diethyl ether.

[Ir(tBudqp)(mppy)CN](PF$_6$) **(3a)**. Yield: 44%. ^{1}H NMR (500 MHz, Acetone-d_6) δ 9.17 – 9.10 (m, 1H), 8.90 (d, J = 7.4 Hz, 2H), 8.59 (d, J = 8.1 Hz, 2H), 8.38 (s, 2H), 8.34 – 8.01 (br m, 4H), 7.99 (d, J = 8.4 Hz, 1H), 7.97 – 7.88 (m, 3H), 7.61 – 7.53 (m, 1H), 7.29 (dd, J = 8.2, 5.4 Hz, 2H), 7.08 (dd, J = 7.4, 1.0 Hz, 1H), 6.82 (dtd, J = 26.4, 7.3, 1.2 Hz, 2H), 2.43 (s, 3H), 1.60 (s, 9H). ^{19}F NMR (470.54 MHz, acetone-d_6): δ -71.11 (d, J = 707.50 Hz, [PF_6^-]). MS (*m/z* ESI, MeOH) Calculated: 776.0 [M-PF_6^-]$^+$ Found: 776.1.

[Ir(tBudqp)(4-Fmppy)CN](PF$_6$) **(3b)**. Yield: 16%. ^{1}H NMR (500 MHz, Acetone-d_6) δ 9.12 (s, 1H), 8.95 (d, J = 7.4 Hz, 2H), 8.61 (d, J = 8.0 Hz, 2H), 8.40 (s, 2H), 8.34 – 8.01 (br m, 4H), 7.97 (m, 4H), 7.67 (dd, J = 8.7, 5.3 Hz, 1H), 7.32 (dd, J = 8.2, 5.4 Hz, 2H), 6.72 (dd, J = 9.2, 2.6 Hz, 1H), 6.61 (td, J = 8.8, 2.6 Hz, 1H), 2.43 (s, 3H), 1.61 (s, 9H).

^{19}F NMR (470.54 MHz, acetone-d_6): δ -71.11 (d, J = 707.41 Hz, [PF_6^-]), -110.21 (s, 1F). MS (*m/z* ESI, MeOH) Calculated: 794.0 [M-PF_6^-]$^+$ Found: 794.1.

[Ir(tBudqp)(2,4-dFmppy)Cl](PF$_6$) **(3c)**. Yield: 42%. ^{1}H NMR (300 MHz, methanol-d_4): d. 9.22 (s, 1H), 8.97 (d, J = 7.44 Hz, 2H), 8.66 (d, J = 8.03 Hz, 2H), 8.43 (s, 2H), 8.31 (d, J = 7.88 Hz, 3H), 8.13 (m, 2H), 8.01 (m, 3H), 7.35 (m, 2H), 6.63 (dd, J = 8.04, 2.31, 1H), 6.52 (m, 1H), 2.46 (s, 3H), 1.62 (s, 9H). ^{19}F NMR (470.54 MHz, acetone-d_6): δ -71.11 (d, J = 707.50 Hz, [PF_6^-]), -107.28 (d, J = 9.8 Hz, 1F), -107.94 (d, J = 9.9 Hz, 1F). MS (*m/z* ESI, MeOH) Calculated: 811.9 [M-PF_6^-]$^+$ Found: 812.1.

[Ir(tBudqp)(PFmppy)CN](PF$_6$) **(3d)**. Yield: 38%. ^{1}H NMR (300 MHz, methanol-d_4): d. 9.03 (s, 1H), 8.81 (m, 2H), 8.62 (m, 2H), 8.22 (m, 5H), 8.02 (m, 5H), 7.29 (m, 2H), 2.45 (s, 3H), 1.59 (s, 9H). ^{19}F NMR (282.37 MHz, methanol-d_4): -74.88 (d, J = 707.59, [PF_6^-]), -128.33 (m, 1F), - 139.47 (m, 1F), -154.40 (m, 1F), -163.16 (m, 1F). MS (*m/z* ESI, MeOH) Calculated: 847.9 [M-PF_6^-]$^+$ Found: 848.1.

3.2.3 Computational Modeling

DFT Calculations were performed using the Gaussian '09 suite.[18] The triplet and singlet ground-state and excited-state were evaluated for the complexes using the B3LYP functional and the LANL2DZ basis set. No symmetry conditions were specified. For TD-DFT calculations, the optimized singlet ground-state geometry was used for the 150 lowest excitations and an acetonitrile solvent model was specified. Orbitals were visualized using Avogadro: an open-source molecular builder and visualization tool Version 1.1.1.[19] TD-DFT calculations of UV-Vis absorption spectra were visualized

using Gaussum,[20] where transitions were expanded into Gaussian curves with a full-width at half-maximum (fwhm) set to 4000 cm^{-1}.

3.2.4 Electrochemical Characterization

Cyclic voltammetry data was collected with the assistance of Joshua J. Zak, using a CH-Instruments Electrochemical Analyzer 600C potentiostat with a three-electrode system consisting of a platinum coil counter electrode, a silver wire pseudo-reference, and a 1 mm^2 platinum disk working electrode. Scans were performed with positive scan polarity, at 0.10 V/S, under an atmosphere of argon, using argon-purged acetonitrile solutions that contained 0.10 M tetra-*n*-butylammonium hexafluorophosphate as the supporting electrolyte and 0.5 mM of the analyte. An internal standard of ferrocene was added to each solution, referencing potentials to SCE via the oxidation of ferrocene at 0.40 V.[21]

3.2.5 Photophysical Characterization

Room temperature photophysical measurements were conducted with the assistance of Joshua J. Zak, using argon-purged 10 μM acetonitrile solutions in screw-top, quartz cuvettes. UV-vis absorption spectra were collected with a Shimadzu UV-1800 spectrophotometer. Photoluminescence characterization experiments were performed using a Fluorolog-3 spectrophotometer equipped with dual monochromators and a photomultiplier tube (PMT) at a right-angle geometry. All compounds were excited at 380 nm. Excited state lifetimes were determined by pulsing samples at 266 nm using the fourth harmonic of a Nd:YAG (Continuum Minilite II) laser. Emission decays were monitored with an oscilloscope (Tektronix TDS 3032B) and converted into a linear regression using a Labview PC interface. Emission quantum yields were determined by comparison against a 10 μM $[Ru(bpy)_3]PF_6$ reference in acetonitrile, with an established

quantum yield (Φ_{ref} = 0.062).[22] Quantum yields were calculated using the equation $\Phi_s = \Phi_{ref}\ (I_s/I_{ref})(A_{ref}/A_s)(\eta_s/\eta_{ref})$, where Φ_s is the quantum yield of the sample, Φ_{ref} is the quantum yield of the reference, I_s and I_{ref} are the maximum emission intensities for the sample and the reference, A_s and A_{ref} are the absorbances of the sample and reference at the excitation wavelength, and η_{ref} and η_s are the refractive indices of the solvents. Radiative decay constants (k_r) were calculated using the equation $k_r = (\Phi_s/\tau_s)$ where τ_s is the excited state lifetime of the sample and subsequently nonradiative decay constants (k_{nr}) were calculated using the relationship $k_{nr} = (1/\tau_s) - kr$. Emission intensities were corrected for the detector's response over the spectral range. Stern-Volmer analysis was performed by measuring the emission intensity from solutions that were purged and blanketed with 10%, 30.2%, and 100% O_2 as well as 100% Argon, at ambient pressures. Slopes of the generated Stern-Volmer plots gave pressure-based Stern-Volmer constants (K_{SVP}).

3.2.6 Photocatalytic Hydrogen Generation

Photocatalytic generation and quantification of H_2 was carried with the assistance of Joshua J. Zak out using the fixed protocol described by Cline et. Al.[23] Screw top EPA vials (40 mL) contained 10 mL of solvent (8 mL acetonitrile, 1 mL triethylamine, 1 mL water), 0.075 mM photosensitizer, and 300 nmol K_2PtCl_4. Control vials were prepared without the photosensitizer, the catalyst, or trimethylamine, or with all components present but without illumination. The vials were placed in a 16 well, temperature controlled photoreactor mounted on an orbital shaker. Each vial was equipped with a pressure transducer as well as a bottom LED for illumination (Luxeon V Dental blue LEDs, LXHL-LRD5 with collimating optics Fraen FHS-HNBI-LL01-H). The vials were

sealed and subsequently degassed with 7 cycles of vacuum and argon, after which the vials were equilibrated to atmospheric pressure at 22 ^{o}C. The orbital shaker was started (100 rpm) and the samples were illuminated. Generation of H_2 was monitored over time by conversion of the pressure transducer readings into pressure traces via a Labview PC interface. Illumination ceased when no further increase in the traces was observed. Following illumination, quantification of H_2 produced was accomplished by injecting 1 mL of the vial headspace in a GOW-MAC gas chromatograph (thermal conductivity detector, Ar carrier gas), pre-calibrated using 10% H_2/Ar gas mixtures.

3.2.7 Photoredox Catalysis

The photoredox catalysis studies were performed with the assistance of Joshua J. Zak, using reaction conditions reported by Ventre et. al.[24] Screw top EPA vials (20 mL) containing 4 mL of solvent (3 mL acetonitrile, 1 mL water), 400 μmol of diphenylacetic acid, 800 μmol of Na_2HPO_4, 1.2 mmol of Selectfluor®, and 0.2 μmol (0.05 mol %) of photosensitizer were equipped with pressure transducers in a 16 well, temperature controlled photoreactor on top of an orbital shaker. Samples were degassed with 7 cycles of vacuum and argon, after which the vials were equilibrated to atmospheric pressure. The orbital shaker was started (100 rpm) and the samples were illuminated from the bottom at 22 ^{o}C (Luxeon V Dental blue LEDs, LXHL-LRD5 with collimating optics Fraen FHS-HNBI-LL01-H). Generation of CO_2 was monitored over time by conversion of the pressure transducer readings into pressure traces via a Labview PC interface. Illumination ceased after 18 hours. The crude reaction mixtures were directly analyzed by ^{19}F NMR using hexafluorobenzene as an internal standard.

3.2.8 Singlet Oxygen Generation

Evaluation of the complexes for singlet oxygen generation was performed with the assistance of Joshua J. Zak, using a protocol adapted from Sun *et. al.*[25] Using an acetonitrile/isopropanol (4:1, v/v) mixed solvent, 1,5-dihydroxynaphthalene (DHN) (1.5×10^{-4} M) and the photosensitizer (5 mol %) were combined in a screw top quartz cuvette and O_2 was bubbled for 15 minutes. The cuvette was placed in the center of a custom fabricated photoreactor that utilized blue-LEDs.[26] UV-vis absorption spectra were recorded at intervals of 2-10 min. Smaller intervals were used for kinetic experiments. The consumption of DHN was monitored by the absorption at 301 nm, and the concentration was determined using the corresponding molar extinction coefficient (ε = 7664 M^{-1} cm^{-1}). The production of Juglone was monitored by the absorption at 427 nm and the concentration of Juglone was determined by using the molar extinction coefficient (ε = 3811 M^{-1} cm^{-1}). Pseudo-first-order rate constant k_{obs} were determined using the equation $\ln(C_t/C_0) = -k_{obs}t$, where C_0 is the starting concentration of DHN, C_t is the concentration at a specific time t. Initial consumption rates of DHN were determined using the equation $v_i = k_{obs}$ [DHN] for the first 30 minutes of illumination. The yield of Juglone was obtained by dividing the concentration of Juglone with the initial concentration of DHN. Control experiments were also performed in the absence of light and photosensitizer.

3.3 Results and Discussion

3.3.1 Synthesis

The addition of a *tert*-butyl group to the tridentate ligand served to not only improve the solubility of the complexes and impart steric bulk, but also to create an

electron rich tridentate ligand to compliment the electron-poor mppy ligands, creating a slight "push-pull" effect. As shown in Scheme 3-1 , initial attempts to prepare the tbudqp ligand via a modified Kröhnke condensation of 8-acetylquinoline and pivaldehyde with KOH and aqueous NH_4OH showed poor conversion, likely due to the poor solubility of the reactants in an aqueous solvent. Neither dilution of the reaction nor increases in reaction temperature were able to produce the desired product. Instead, it was found that changing the base to potassium *tert*-butoxide, the solvent to a THF/AcOH mixture, and the nitrogen source to NH_4OAc successfully gave the desired tbudqp ligand in good yields. This procedure was previously used by Constable *et*. *al*. to prepare 4′-tert-butyl-2,2′:6′,2″-terpyridine in high yields.[27]

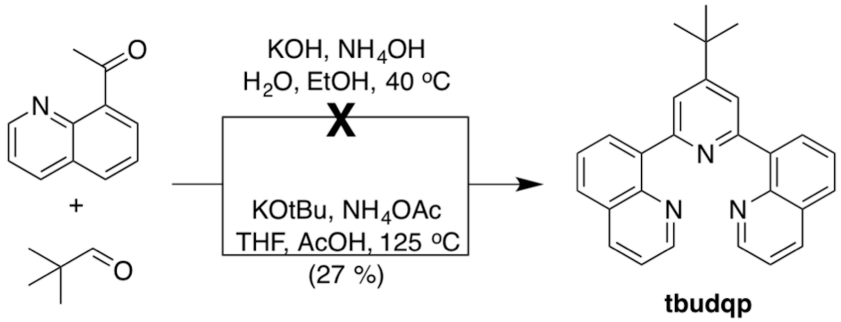

Scheme 3-1. Synthesis of tbudqp. Isolated yields in parentheses.

Subsequently, the [Ir(tbudqp)Cl_3] precursor **1a** was synthesized in good yields by reacting tbudqp and $IrCl_3$•$4H_2O$ in ethylene glycol (Scheme 3-2). Optimal yields were achieved with elevated temperatures, extended reaction times, dilution of the reaction mixture, and omission of light and air. The chloride complexes **2a**-**2d** were synthesized by reaction with mppy ligands in ethylene glycol overnight, followed by dilution with water, extraction with an organic solvent, and precipitation with aqueous KPF_6. To achieve varying degrees of fluorination, both C-H and C-F activation were used. To generate the corresponding cyanide complexes **3a**-**3d**, a one-pot reaction of the

corresponding chloride complex and aqueous KCN produced the cyanide analogue after precipitation with aqueous KPF_6 (Scheme 3-3).

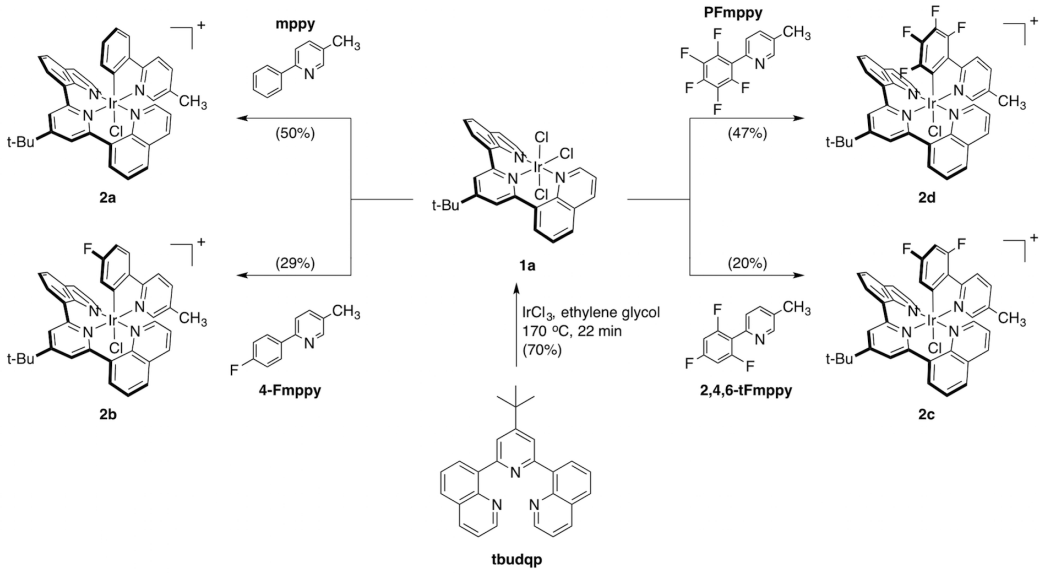

Scheme 3-2. Synthesis of Ir(III) complexes **1a**, **2a**-**2d**. Isolated yields in parentheses. Reaction conditions as follows: a) $IrCl_3 \bullet 4H_2O$, ethylene glycol, argon atmosphere 170 ^oC, 22 min. b) mppy ligand, ethylene glycol, argon atmosphere, 183 ^oC, overnight.

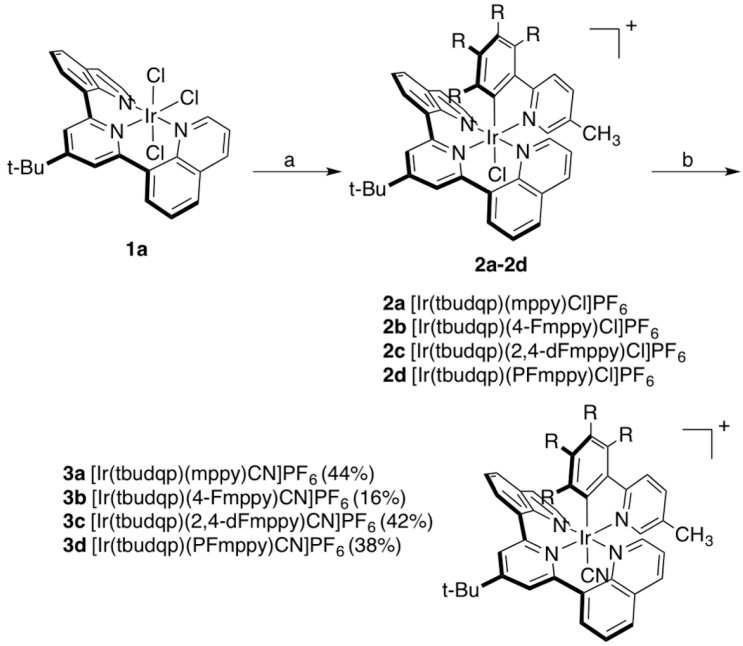

Scheme 3-3. Chloride-Cyanide Exchange of Ir(III) Complexes. Isolated yields in parentheses. Reaction conditions as follows: a) mppy ligand, ethylene glycol, argon

atmosphere, 183 ^{o}C, overnight. b) KCN (aq), ethylene glycol, argon atmosphere, 90 ^{o}C, 2 hr.

3.3.2 Computational Modeling

The electronic structures of the complexes were modeled using static DFT calculations in Gaussian '09, specifically with the B3LPY functional and LANL2DZ basis set. Frontier orbital diagrams for the unsubstituted chloride complex **2a** (Figure 3-3) and perfluorinated cyanide complex **3d** (Figure 3-4) are shown below. The HOMO of the chloride complexes has contributions from the phenyl ring of the mppy ligand, the d orbital of the Ir, and the ancillary ligand. The LUMO of the chloride complexes is primarily located on the tridentate ligand and the iridium d orbitals, as well as increasing contributions of the mppy ligand as the complexes become more fluorinated. In contrast, the HOMO of cyanide complexes **3a-3d** is primarily on the phenyl ring of the mppy ligand, the d orbital of the Ir, and the ancillary ligand like the chloride complexes **2a-2d**, but as fluorination increases the tridentate ligand begins to become involved as well. The LUMO of the cyanide complexes is a mixture of the tridentate ligand's π^* orbitals and the Ir d orbitals, but consistently has a small contribution from the mppy ligand as well.

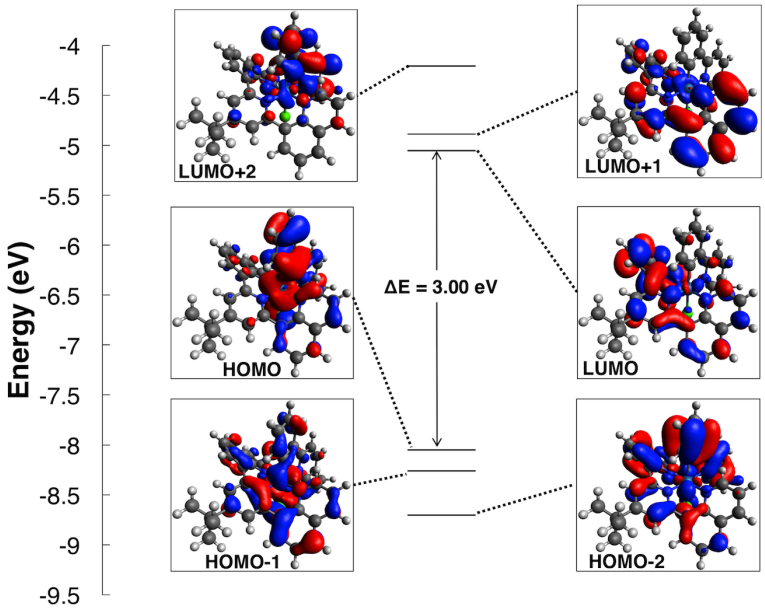

Figure 3-3. Singlet frontier orbital diagram of **2a**. Orbitals were calculated using Gaussian '09 DFT (B3LYP/LANL2DZ).

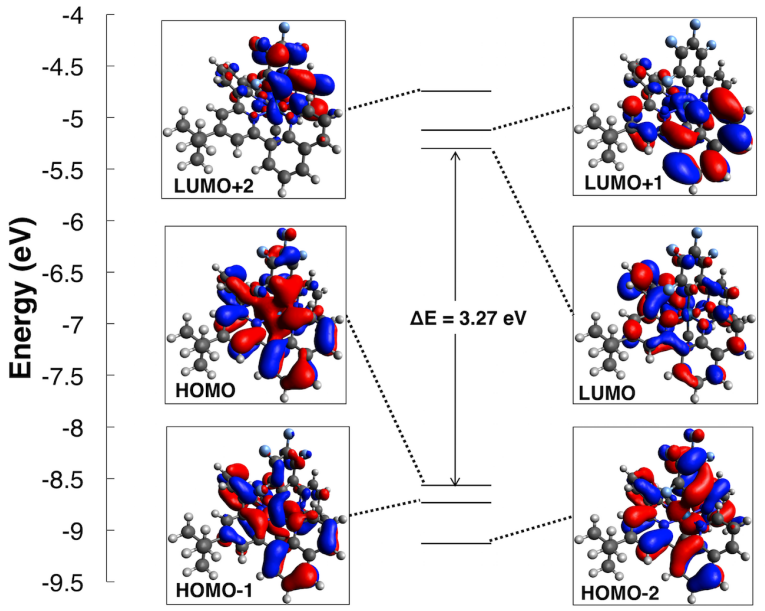

Figure 3-4. Singlet frontier orbital diagram of **3d**. Orbitals were calculated using Gaussian '09 DFT (B3LYP/LANL2DZ).

As the chloride complexes increase in fluorination, the HOMO energy levels are reduced. Unsubstituted **2a** is calculated at -8.05 eV whereas perfluorinated **2d** sits at -8.57 eV. A similar trend is observed for the cyanide complexes, whereby unsubstituted

3a is found at -8.26 eV compared to perfluorinated **3d** which is at -8.88 eV. The LUMO levels of the chloride complexes also see a change based on fluorination, with **2a** at -5.05 eV compared to **2d** at -5.30 eV. The cyanide complexes LUMOs are also changed with fluorination, with **3a** at -5.11 eV and **3d** at -5.36 eV. Increasing fluorination for both the chloride and cyanide complexes broadens the HOMO-LUMO gap, with **2a** having a 3.00 eV gap compared to 3.27 eV for **2d**, and a 3.15 eV gap for **3a** compared to 3.52 eV for **3d**. Exchange of the chloride ligand to the stronger field cyanide significantly decreases the HOMO, slightly impacts the LUMO, and broadens the HOMO-LUMO gaps. When compared to previously established [Ir(N^N^N)(C^N)X]+ complexes such as $[Ir(tpy)(ppy)Cl]^+$ (2.88 eV) and $[Ir(tpy)(ppy)CN]^+$ (3.05 eV), the new complexes have significantly wider band gaps.[1] Furthermore, the band gaps are wider than the parent bis-cyclometallated $[Ir(ppy)_2(bpy)]^+$ complex (2.63 eV).

3.3.3 UV-Vis Absorption Spectroscopy

The absorption spectra of complexes **2a**, **2d**, **3a**, and **3d** are shown in Figure 3-5. While the origins of the transitions for previous families of $[Ir(N^N^N)(C^N)X]^+$ have been established,[1,2] TD-DFT modeling was necessary to determine the origins of the observed transitions for this new ligand structure (Figure 3-6). It is worth noting that the new complexes are nearly twice as absorptive as previously established $[Ir(N^N^N)(C^N)X]^+$ complexes, owing to the extended π system of the tbudqp ligand.[1,2] A weak feature near 475 nm (HOMO→LUMO, mixed MLCT/ILCT) is present in **2a**, and as the complexes increase in fluorination, a blue shift is measured such that the same transition in **2d** is observed at 427 nm. In the cyanide complex **3a**, the same transition is blue shifted from the chloride analogue **2a** to 450 nm, and even more blue-shifted in **3d**

where the same transition is found at 396 nm. Another feature at 383 nm in **2a** (HOMO-2→LUMO, mixed MLCT/ILCT), is blue shifted to 364 nm in **2d**, 378 nm in **3a**, and 356 nm in **3d**. All of the complexes share several transitions centered around 330 nm, which all correspond to mixed MLCT/ILCT transitions that are unaffected by the fluorination of the mppy ligand or changes in the ancillary ligand. Between 240 nm and 300 nm, **2a** and **3a** lack any strong transitions whereas **2d** and **3d** for two bands centered around 291 nm and 289 nm, which correspond to transitions primarily on the mppy (HOMO-4→LUMO+2) and the tbudqp ligand (HOMO-2→LUMO+3) respectively. All of the complexes share a strong transition centered around 230 nm, which is predominantly an centered around the π and π* orbitals of the phenyl ring from the cyclometallating ligand and the tridentate ligand. This transition is also unaffected by ligand fluorination and ancillary ligand, likely due to the significantly larger π system of the tbudqp ligand. Other relevant photophysical properties including measured emission properties are included in Table 3-1.

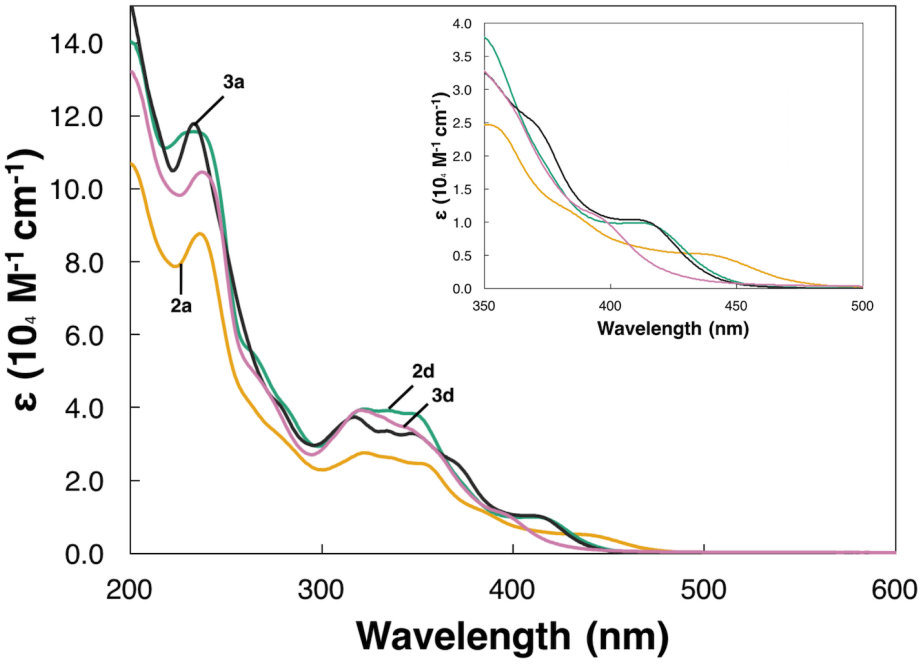

Figure 3-5. UV-Vis absorption spectra of **2a**, **2d**, **3a**, and **3d**. The portion of the spectrum from 350 nm to 500 nm is enlarged in the inset to show details of the weaker transitions. All spectra were collected at room temperature using 10 µM solutions.

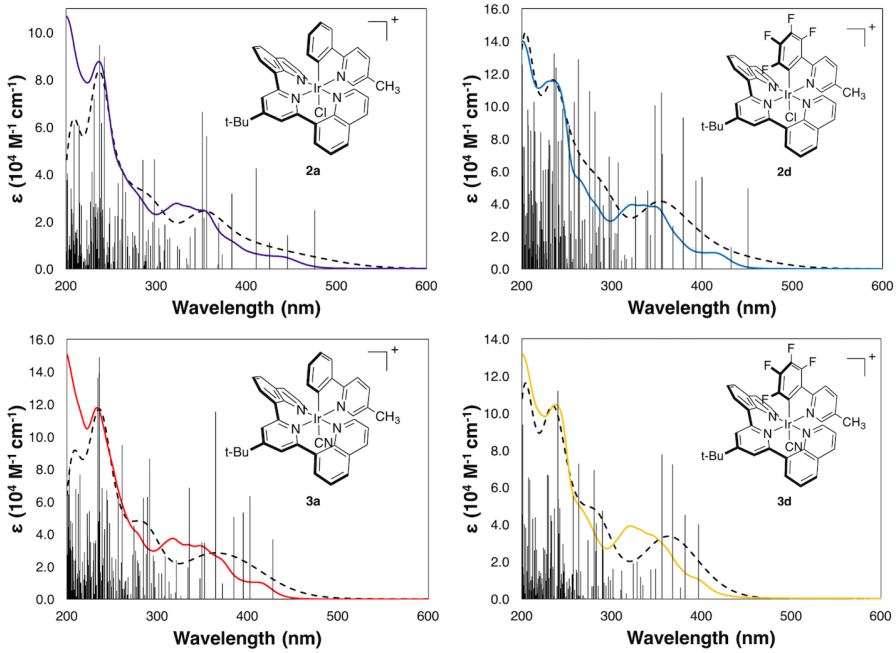

Figure 3-6. Experimental (solid, colored) and calcuated (black dashed) UV-Vis absorption spectra of 2a, 2d, 3a, and 3d. Calculated spectra were determined using Gaussian '09 TD-DFT calculations and Gaussum software with a fwhm = 4000 cm^{-1}. Oscillator strengths are included as vertical lines.

Table 3-1. Photophysical Properties of tbudqp Ir(III) Complexes. Samples were analyzed as 10 μM solutions in acetonitrile after purging and blanketing with argon.

		emission				
complex	absorption λ_{max}/ nm (intensity/10^4 M^{-1} cm^{-1})	λ_{max} / nm	τ/ μs	Φ/ %	k_{nr} (10^4) / s^{-1}	k_r (10^4) / s^{-1}
2a	236 (8.77), 274sh (3.45), 322 (2.76), 336 (2.63), 352 (2.47), 440 (0.48), 460 (0.25)	587	14.18	35.7	4.54	2.52
2b	236 (10.31), 278sh (4.07), 321 (3.04), 335 (3.05), 350 (2.96), 433 (0.56), 460 (0.14)	584	18.66	38.2	3.33	2.05
2c	232 (11.76) 279sh (4.00), 317 (3.49), 335 (3.35), 351 (3.23), 428 (0.65), 460 (0.09)	581	20.42	30.8	3.39	1.51
2d	233 (11.79) 276sh (4.18), 317 (3.74), 334 (3.37), 348 (3.29), 414 (1.02), 460 (0.03)	578	22.03	25.4	3.39	1.15
3a	229 (11.65), 264 (5.65), 321 (3.92), 333 (3.99), 348 (3.88), 417 (0.96), 460 (0.04)	581	22.97	17.8	3.58	0.77
3b	236 (11.94), 264 (5.81), 319 (3.70), 334 (4.01), 348 (3.88), 408 (1.04), 460 (0.02)	573	27.86	24.2	2.72	0.87
3c	236 (11.06), 266 (4.87), 318 (3.44), 333 (3.53), 346 (3.41), 405 (0.95), 460 (0.01)	573	29.82	24.8	2.52	0.83
3d	238 (10.45), 265 (4.93), 320 (3.92), 333 (3.71), 348 (3.36), 397 (1.05), 460 (0.06)	572	30.91	18.7	2.63	0.60

3.3.4 Emission Spectroscopy

The complexes were weakly photoluminescent in argon-degassed, room temperature acetonitrile (Figure 3-7), with emission intensities an order of magnitude weaker than traditional Ir(III) photosensitizers at the same concentrations and quantum yields less than 40%. Despite modulation of the HOMO by fluorination and exchange of the chloride to a cyanide, an orange emission was observed for all complexes.

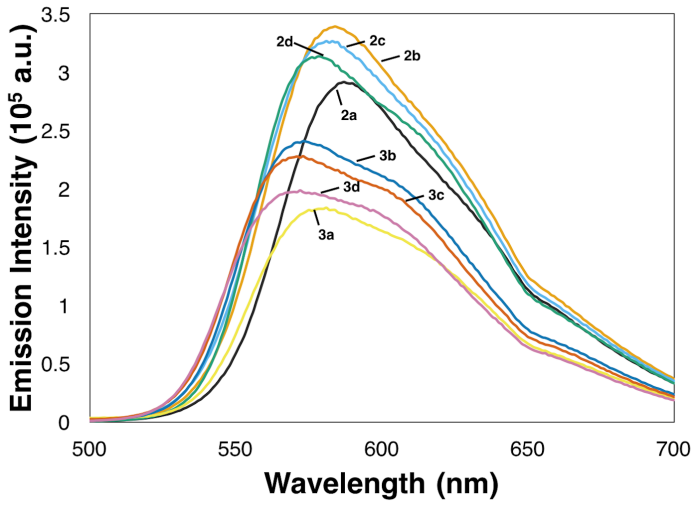

Figure 3-7. Room temperature emission spectra of degassed 10 μM solutions of **2a-3d** in acetonitrile. Complexes were excited at 380 nm.

The chloride complexes had broad, structureless emissions that correspond to a mixed MLCT/ILCT character that is typical of cyclometallated Ir(III) complexes. In contrast, the cyanide complexes appeared slightly more structured, which can be attributed to an increase of ILCT character of the emission observed in these complexes. The emission maxima of the chloride and cyanide complexes is slightly blue-shifted as the complexes increase in degree of fluorination. Likewise, exchange of the chloride to a cyanide results in a small blue shift of the emission maximum when compared to the corresponding chloride analogue.

The complexes have notably high excited state lifetimes (Table 3-1) despite the lack of any organic dyes tethered to the complexes, which has previously been a strategy used to produced long-lived Ir(III) complexes. Increasing fluorination and exchange of the chloride to a cyanide result in a significant increase in the excited state lifetime, with **3d** exhibiting the longest lifetime of nearly 31 μs. However, the extended excited state lifetimes and changes in ligand structure do result in an order of magnitude decrease in the k_r and k_{nr} values compared to traditional $[Ir(ppy)_2(bpy)]^+$ complexes. Similarly, the

quantum yields of the complexes don't quite reach those of traditional $[Ir(ppy)_2(bpy)]^+$, but are similarly influenced by the ligand structure. Increasing fluorination from zero to one fluorine results in an increase in quantum yield, for both the chloride and cyanide complexes. Interestingly, any additional fluorine atoms decrease the quantum yield of the complexes. Overall, the chloride complexes exhibit higher quantum efficiencies than those observed in the cyanide complexes.

The extension of the excited lifetimes of the complexes can be ascribed to the change in coordination of the tbudqp ligand compared to that of a terpyridine. Previous studies have shown that the increase in bite-angle of dqp based ligands allows for a coordination with a more optimal octahedral geometry than that of terpyridine complexes, and this in turn leads to a higher ligand field splitting of the complex.[11–14] For example, the published terpyridine analogue to **2a**, $[Ir(tpy)(ppy)Cl]^+$ has an excited state lifetime of only 1.67 μs, nearly an order of magnitude shorter than **2a** which decays with a 14.17 μs lifetime.[1] The quantum yield of emission of **2a** is also double that of $[Ir(tpy)(ppy)Cl]^+$ (15.0 % vs 35.7 % for **2a**). While the k_{nr} of **2a** is an order of magnitude lower than that of $[Ir(tpy)(ppy)Cl]^+$ (5.07×10^5 vs 4.54×10^4 for **2a**), there is a diminished return on the k_r (9.0×10^4 vs 2.52×10^4 for **2a**). These dramatic changes in photophysical properties by simply changing of the tridentate ligand are certainly noteworthy and could make the dqp ligand framework of use to other Ir(III) based luminophores.

3.3.5 Electrochemical Characterization

To further evaluate the complexes and understand their respective tunability, cyclic voltammetry experiments were performed in acetonitrile (Table 3-2). The complexes all showed a single, metal centered oxidation that was found to be reversible

in the chloride complexes and irreversible in the cyanide complexes (Figure 3-8). It's worth noting that previous complexes with the $[Ir(N^N^N)(C^N)X]^+$ ligand framework have shown up to two metal centered oxidations. For both the chloride and cyanide complexes, as the mppy ligands increase in fluorination, the oxidation potential shifts positively due to the increased HOMO stabilization caused by the mppy and ancillary ligands. Exchange of the chloride to a cyanide also positively shifts the oxidation potential due to the increased ligand-field character of the cyanide compared to the chloride.

With the exception of **2c**, all complexes have one reversible reduction feature and one quasi-reversible reduction potential. For complexes **2a** and **2b**, the first reduction is reversible whereas the second is quasi-reversible. For complex **2c**, both the first and second reduction are irreversible. For complexes **2d** and **3a-3d** the first reduction is quasi-reversible and the second is reversible.

Previously, the first reduction of Ir(III) complexes with the $[Ir(N^N^N)(C^N)X]^+$ structure have been assigned to the tridentate ligand, given the involvement of the ligand in the LUMO. While the complexes all have the same tridentate ligand, slight differences in the potentials are still observed based on changes to the cyclometallating ligand and the ancillary ligand. The gradual change in reversibility of the first reduction can be corroborated with the changes in the electronic structure of the LUMO. As the chloride complexes become increasingly fluorinated, the LUMO sees greater contributions from the pyridine ring of the cyclometallating ligand in addition to the tridentate ligand. Complexes **2a** and **2b** have little to no involvement of the pyridine ring, therefore the first reduction is purely located on the tridentate ligand, and thus reversible. As more and

more of the pyridine ring is involved in the LUMO, the ability for the pyridyl nitrogen to dissociate is reflected in the reduction features, thereby increasingly making it more irreversible. Complexes **2c** and **2d** had the most involvement of the pyridine ring to the LUMO, thereby making their first reductions most irreversible. The cyanide complexes all had involvement of the pyridine rings in their LUMOs and all of their first reductions became electrochemically irreversible.

The second reductions observed in these Ir(III) tbudqp complexes were ascribed to the Ir center, phenyl ring of the cyclometallating ligand and the ancillary ligand. The second reduction in the chloride complexes became more reversible as the complexes were fluorinated, likely owing to the more negative potentials that would have corresponded to chloride dissociation. With no dissociation of the chloride possible within the solvent window of acetonitrile, the second reductions were observed as quasi-reversible in **2a**-**2c**, and fully reversible in **2d**. Since the cyanide is a much stronger field ligand, dissociation is unlikely and the second reduction in the cyanide complexes **3a**-**3d** was always observed to be reversible. In the chloride complexes, the fluorination of the cyclometallating ligand shift the second reduction more and more negative, whereas all of the cyanide complexes remained fairly unchanged by the degree of fluorination, owing to the greater backbonding and stability of the cyanide ligand.

The only complex to have a third reduction is the chloride complex **2a**. Previously studied $[Ir(N^N^N)(C^N)Cl]^+$ complexes had a third, irreversible reduction that was ascribed to the dissociation of the chloride ligand.[1,2,28] When the other chloride complexes **2b**-**2d** were analyzed by cyclic voltammetry, the third reduction could not be observed and is believed to be beyond the solvent window for acetonitrile. This is

especially true given that the potential for **2a** was already at 2.11 V, which is adjacent to the solvent window for acetonitrile.

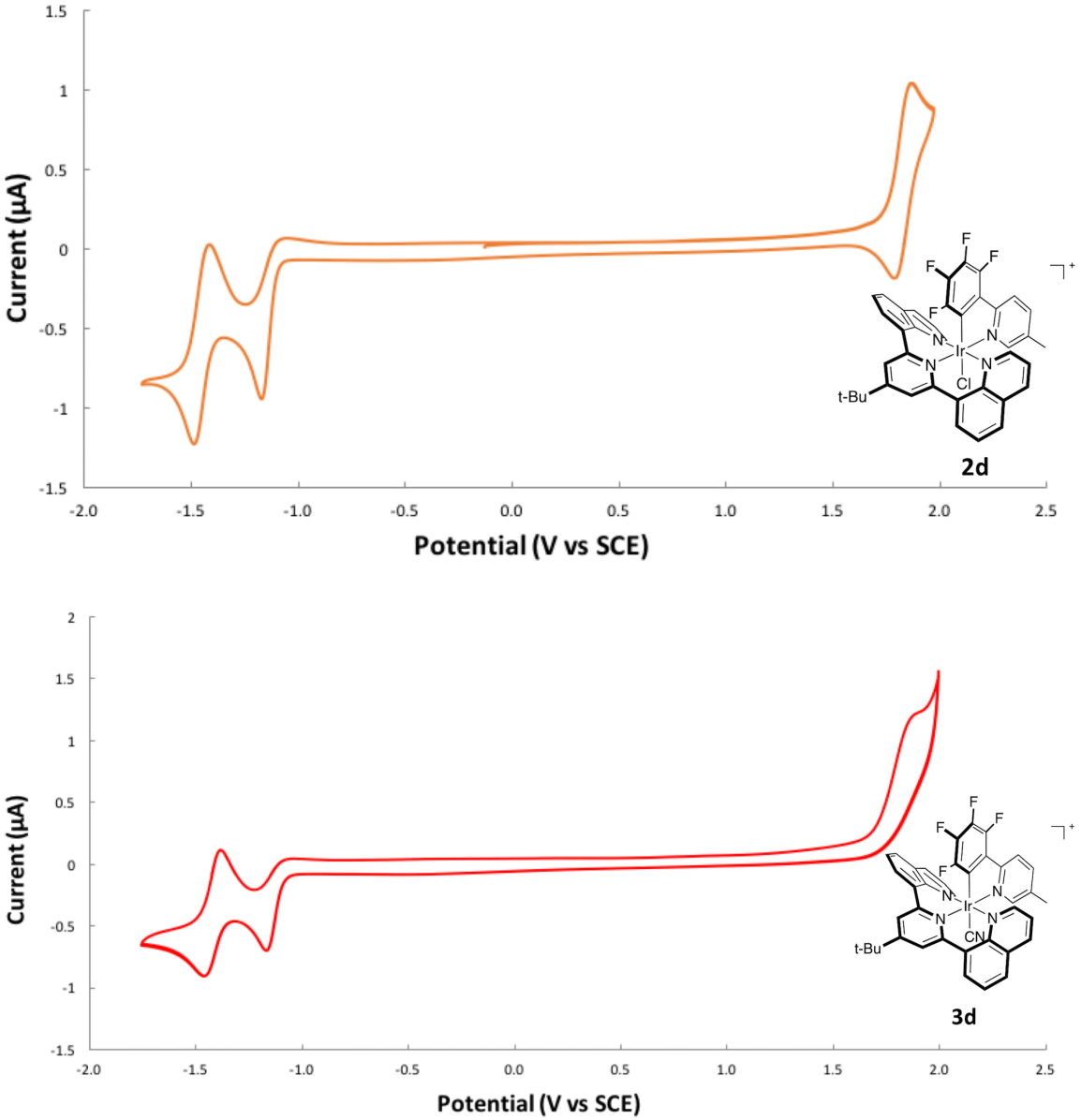

Figure 3-8. Cyclic voltammograms of **2d** and **3d**. Voltammograms were recorded using argon-degassed 0.10 M tetra-n-butylammonium hexafluorophosphate (acetonitrile) solutions containing 0.5 mM of analyte, at 0.10 V/s with a three-electrode system. All potentials are referenced to SCE using ferrocene as an internal standard (fc/fc^+ = 0.40 V).[21]

Table 3-2. Electrochemical Properties of tbudqp Complexes. ΔE values reported in mV for reductions that are fully reversible.

compound	oxidation	reduction		
	E_{pa}/V	**I**: E_{pc}/V	**II:** E_{pc}/V	**III:** E_{red}/V
2a	1.51	-1.20 (112)	-1.29	-2.11
2b	1.63	-1.20 (46)	-1.51	-
2c	1.72	-1.16	-1.49	-
2d	1.83	-1.12	-1.45 (78)	-
compound	oxidation	reduction		
	E_{pa}/V	**I**: E_{pc}/V	**II**: E_{pc}/V	
3a	1.67	-1.16	-1.45 (78)	
3b	1.80	-1.15	-1.44 (90)	
3c	1.91	-1.13	-1.43 (55)	
3d	1.80	-1.11	-1.42 (62)	

Excited state redox potentials were determined for the complexes using the potentials from cyclic voltammetry and the emission maxima of each complex (Table 3-3). These potentials are useful for evaluating the excited state redox behavior, and thereby photosensitization properties, of the complexes. All of the complexes were found to be weakly reducing compared to the established water reducing catalyst $[Ir(ppy)_2(bpy)]^+$, and all but **2a** were less reducing than $[Ir(tpy)(ppy)Cl]^+$, which is an example of an $[Ir(N^N^N)(C^N)X]^+$ complex also used for photocatalytic water reduction. However, the excited states of the complexes are more strongly oxidizing than $[Ir(ppy)_2(bpy)]^+$, but not as oxidizing as $[Ir(tpy)(ppy)Cl]^+$.

Table 3-3. Calculated Excited State Redox Potentials of tbudqp Complexes.

compound	E ($[M^*]^+/[M]^{2+}$)/V[a,b]	E ($[M^*]^+/[M]^0$)/V[a,c]
2a	-0.61	0.92
2b	-0.49	0.92
2c	-0.42	0.97
2d	-0.32	1.03
3a	-0.46	0.98
3b	-0.32	0.97
3c	-0.25	1.04
3d	-0.37	1.05
$[Ir(tpy)(ppy)Cl]^+$ [1]	-0.57	1.20
$[Ir(ppy)_2(bpy)]^+$ [29]	-0.85	0.68

Potentials are given in V vs SCE. [b] $E([M^*]^+/[M]^{2+}) = E_{ox} - E_{\lambda em}$. [c] $E([M^*]^+/[M]^0) = E_{red} + E_{\lambda em}$.[30]

3.3.6 Photocatalytic Hydrogen Evolution

Given the extended excited state lifetimes and enhanced electrochemical stability observed in the chloride complexes, the complexes were subsequently evaluated as photosensitizers for the photocatalytic generation of hydrogen from water. The reactions used an established procedure that involved a mixed acetonitrile/water solvent mixture, K_2PtCl_4 as the water reduction catalyst, and triethylamine as the sacrificial donor.[23]

Based on the hydrogen evolution traces in Figure 3-9 , the new complexes were able to function as photosensitizers for the reaction, but were not nearly as effective as previously established complexes with a similar $[Ir(N^N^N)(C^N)X]^+$ structure.[1,2] Overall, the cyanide complexes **3a**, **3b**, and **3d** were shown to be the best performers, likely due to the stronger field, less labile cyanide ligand compared to the corresponding chloride analogues. The trends for the chloride complexes **2a**-**2d** would indicate that increasing fluorination improves photocatalytic performance until a switch occurs for the perfluorinated **2d**, which exhibits a decrease in TON compared to the rest of series. The poorer performance of **2a** compared to the other chloride complexes is due to the fact that according to its electrochemistry, the chloride ligand is most easily dissociated in **2a**

despite it having the highest extinction coefficient at the emission maxima of the blue LEDs (460 nm). Complexes **2b** and **2c** have the next highest extinction coefficients and would be envisioned as being more stable than **2a** in terms of chloride dissociation. The poorest performance of **2**d is likely due to the significantly weaker absorption at 460 nm when compared to the rest of the chloride series. The cyanide complexes follow a similar trend, however the performance of perfluorinated **3d** is higher than that of difluorinated **3c**. Upon analysis of their UV-Vis spectra of the complexes, it was determined that the best performing complexes **3a**, **3b**, and **3d** had the highest extinction coefficients at the illumination wavelength of the LED source used. This coupled with the less labile cyanide ligand as the ancillary ligand would account for the improved performance of the complexes compared to the chloride analogues. Overall, this reaction could be further optimized with different sacrificial reductants and water reducing catalysts that could be better suited for these photosensitizers.

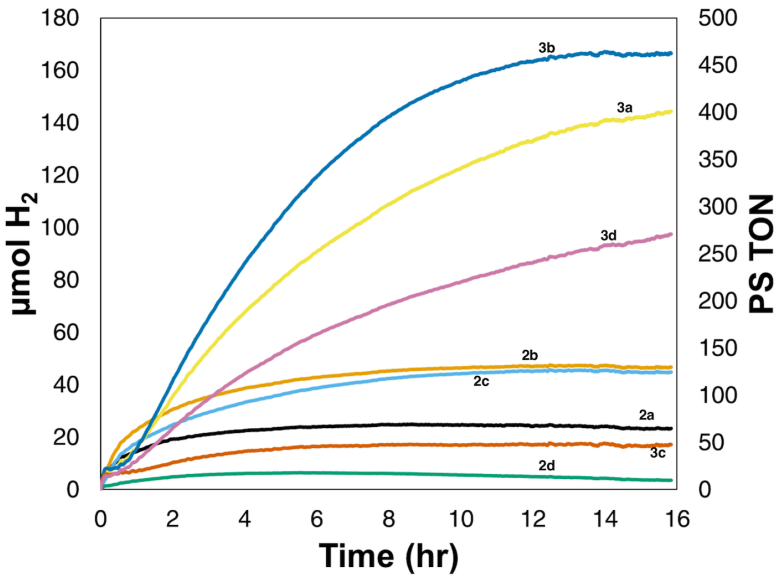

Figure 3-9. Photocatalytic hydrogen evolution traces of **2a-3d**. Quantities of hydrogen evolved are noted along with the TON of the Ir(III) photosensitizers.

3.3.7 Photoredox Catalysis

Photosensitizers **2a** and **3a** were evaluated for the decarboxylative fluorination of several carboxylic acids (Scheme 3-4). Previous studies have shown that $[Ir(ppy)_2(bpy)]^+$ based complexes can serve as photosensitizers for several organic transformations, [31] but also complexes with the $[Ir(N^N^N)(C^N)X]^+$ structure.[2] As such, evaluation as photosensitizers for photoredox catalysis is a logical progression. The complexes were also evaluated against the published "best performer" for this specific transformation, $[Ir(dF(CF_3)ppy)_2(dtbbpy)]^+$.[24] Reaction yields were determined by ^{19}F NMR using hexafluorobenzene as an internal standard. NMR signals of the products matched those reported in the literature (fluorodiphenylmethane,[32] fluorocyclohexane,[33] 4-(fluoromethyl)-1,1'-biphenyl and 2-fluoroethane-1,1,1-triyl)tribenzene[24]). Control reactions which omitted catalyst, base, and light did not generate the fluorinated products.

The yields of the reactions driven with **2a** and **3a** were found to be comparable not just to each other, but also to $[Ir(dF(CF_3)ppy)_2(dtbbpy)]^+$ (Table 3-4). It should be noted that while previous studies showed better performances from the $[Ir(N^N^N)(C^N)X]^+$ structure[2] after 2 hours of illumination, the rate of reaction for **2a** and **3a** were too slow to show reaction completion within that timeframe, and thus the reaction time was extended to 18 hours. These results indicate that despite the lower emission quantum yield compared to $[Ir(dF(CF_3)ppy)_2(dtbbpy)]^+$, the complexes can overcome that with their enhanced stability in the coordinating reaction solvent. $[Ir(ppy)_2(bpy)]^+$ based complexes are known to degrade in coordinating solvents,[34,35] and the fact that more stable complexes **2a** and **3a** were still able to outperform the less stable $[Ir(dF(CF_3)ppy)_2(dtbbpy)]^+$ speaks to their utility as a photosensitizer.

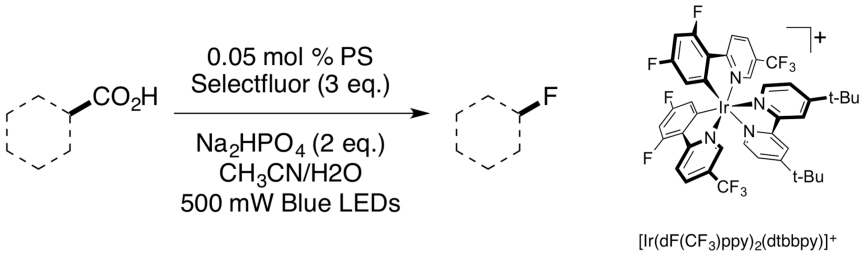

Scheme 3-4. Decarboxylative Fluorination of Carboxylic Acids and the structure of $[Ir(dF(CF_3)ppy)_2(dtbbpy)]^+$.

Table 3-4. Photosensitizer and substrate studies of the Decarboxylative Fluorination Reaction. Yields determined by ^{19}F NMR after 18 hours of illumination with C_6F_6 as an internal standard.

		yield (%)		
R-CO_2H	R-F	**2a**	**3a**	$[Ir(dF(CF_3)ppy)_2(dtbbpy)]^+$
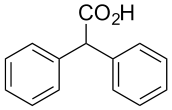	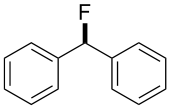	82	91	88
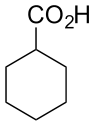	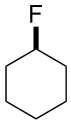	67	73	68
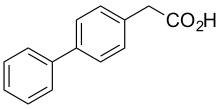	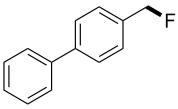	93	100	100
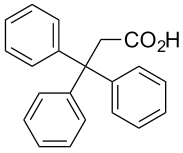	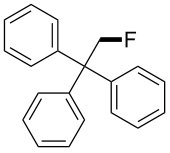	98	100	95

3.3.8 Oxygen Quenching and Singlet Oxygen Generation

With such long excited state lifetimes, the sensitivity of the complexes to quenching by oxygen is an interesting avenue to pursue. Previously, several Ir(III) photosensitizers with long excited state lifetimes showed high sensitivity to quenching by oxygen, however the extended lifetimes were due to the addition of dye molecules to the

ligands.[25,36–42] Given the simpler structure of complexes **2a-3d**, they show potential as suitable alternatives. Solutions of the complexes were sparged with varying concentrations of O_2, and the changes in excited state lifetimes were used to perform a Sterm-Volmer analysis. The complexes were also compared to established singlet oxygen photosensitizer $[Ir(ppy)_2(phen)]^+$ (Table 3-5). Based on analysis of the slopes of Stern-Volmer plots, the complexes **2a-3d** are in fact more sensitive to quenching by oxygen than $[Ir(ppy)_2(phen)]^+$.This increased sensitivity to oxygen would limit the ability for the complexes to serve as photosensitizers for total water splitting, where O_2 would be generated and subsequently quench the excited photosensitizer. Instead these complexes could easily serve as emissive oxygen sensors and replace the more complicated, dye-substituted complexes.

Table 3-5. Emission quenching of Ir(III) complexes by O_2, measured in MeCN at room temperature.

compound	K_{SVP} /mbar $^{-1}$
2a	0.1144
2b	0.1029
2c	0.1429
2d	0.1902
3a	0.0882
3b	0.1046
3c	0.2295
3d	0.2398
$[Ir(ppy)_2(phen)]^+$	0.0694

With this increased sensitivity towards molecular oxygen, the complexes could also serve as photosensitizers for the photogeneration of singlet oxygen. To evaluate the complexes, an established protocol that utilizes the photooxidation of 1,5-dihydroxynaphthalene to Juglone by in-situ generated singlet oxygen was used (Scheme 3-5). The progression of the reaction, as well as overall yield, could be monitored using

UV-Vis spectroscopy (Figure 3-10). After bubbling 100% O_2 gas into a screw top cuvette with the photosensitizer and DHN in a MeCN/isopropanol mixture, the cuvette was illuminated using blue LEDs and UV-Vis measurements were recorded over time. Percent yields for the reactions, as well as pseudo-first-order rate constants and initial rates were collected (Table 3-6). A control reaction in the absence of light did not generate Juglone however a control reaction without a photosensitizer did have a 20 % conversion, which corroborates with previous observations that indicate another photooxidation pathway is possible.[25]

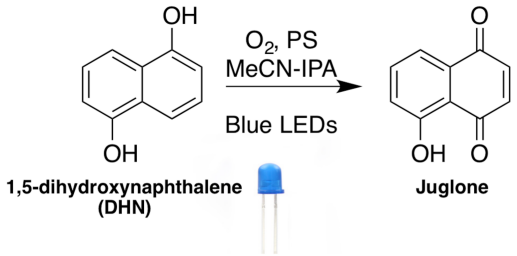

Scheme 3-5. Photooxidation of DHN to Juglone.

Three of the new complexes were shown to outperform the established $[Ir(ppy)_2(phen)]^+$, specifically **2a**, **2b**, and **2c**. The complexes were shown to have higher rate constants, initial rates, and % yields. Trends in the performance of the complexes can be ascribed to an increasingly electron-poor mppy ligand, as well as change in the ancillary ligand from a chloride to a cyanide all lessen the performance. This change impacts the observed transitions in the complexes, and increasingly fluorination actually weakens the absorption of the complexes at 460 nm (emission maxima of the blue LEDs). Complexes **2a**-**2c** all have the highest absorbances at 460 nm of the series as well as the shortest excited state lifetimes.

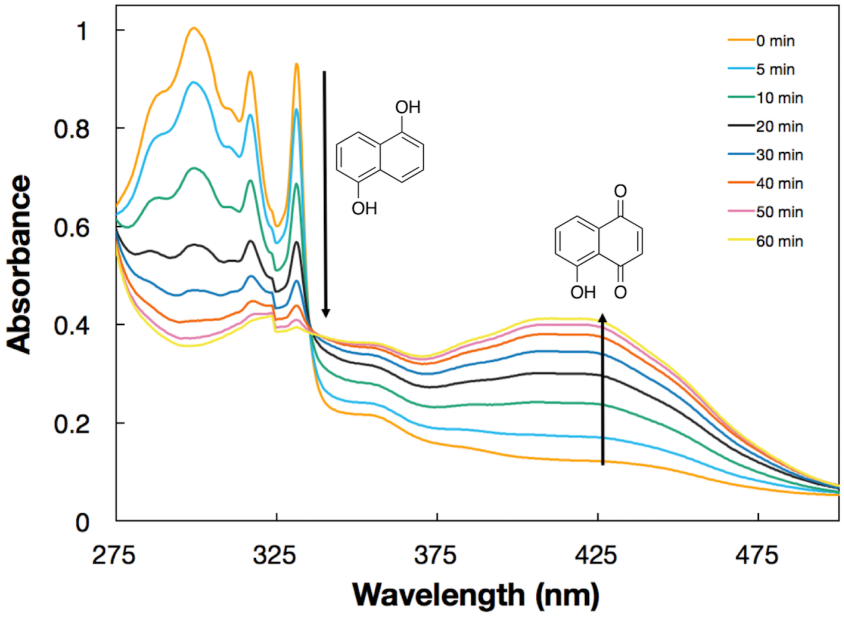

Figure 3-10. UV-Vis spectral changes in the photooxidation of DHN to Juglone using **2a** as the photosensitizer, with illumination using blue LEDs.

Table 3-6. Photooxidation of DHN related parameters of Ir(III) complexes, measured in MeCN/isopropanol mixed solvent, at room temperature.

compound	k_{obs} /x 10^{-3} min^{-1}	v_i /x 10^{-7} M min^{-1}	% yield
2a	19.5	23.6	60.2
2b	14.8	18.2	55.2
2c	13.1	16.6	52.9
2d	6.1	8.0	42.2
3a	6.6	8.5	44.2
3b	4.4	5.8	39.4
3c	4.1	5.3	37.3
3d	2.7	3.4	30.5
$[Ir(ppy)_2(phen)]PF_6$	8.0	10.7	50.1

3.4 Conclusions

A new family of Ir(III) photosensitizers using the $[Ir(N^N^N)(C^N)X]^+$ framework were synthesized using tbudqp as the tridentate ligand. The quinoline rings allowed for the ligand to have improved coordination ability to the Ir(III) center, which resulted in key enhancements to some photophysical properties including some of the longest

reported excited state lifetimes for an Ir(III) complex free of any dye molecules. The HOMO of complexes was still tunable through the use of different mppy ligands as well as changing the chloride ligand to a stronger field cyanide. These changes modified the photophysical, electrochemical, and catalytic properties of the complexes. The complexes performed well as photosensitizers for photocatalytic hydrogen generation as well as for the decarboxylative fluorination of carboxylic acids. The complexes also functioned excellently as sensitizers for photogeneration of singlet oxygen for the photooxidation of 1,5-dihydroxynaphthalene to juglone, outperforming previously established, dye-free Ir(III) complexes. Given some of the improvements made by switching from a terpyridine to a bis-quinolylpyridine, further investigations into this ligand structure have to be pursued. The ease of ligand synthesis could allow for installation of aromatic groups with different functionalities to better modulate the LUMO, as well as to allow for further reactions including couplings to other complexes or molecules to continue to diversify the applications of these complexes.

3.5 References

(1) Chirdon, D. N.; Transue, W. J.; Kagalwala, H. N.; Kaur, A.; Maurer, A. B.; Pintauer, T.; Bernhard, S. *Inorg. Chem.* **2014**, *53*, 1487–1499.
(2) Porras, J. A.; Mills, I. N.; Transue, W. J.; Bernhard, S. *J. Am. Chem. Soc.* **2016**, *138*, 9460–9472.
(3) Genoni, A.; Chirdon, D. N.; Boniolo, M.; Sartorel, A.; Bernhard, S.; Bonchio, M. *ACS Catal.* **2017**, *7*, 154–160.
(4) Sato, T.; Awano, H.; Haba, O.; Katagiri, H.; Pu, Y.-J.; Takahashi, T.; Yonetake, K. *Dalton Trans.* **2012**, *41*, 8379–8389.
(5) Reithmeier, R. O.; Meister, S.; Rieger, B.; Siebel, A.; Tschurl, M.; Heiz, U.; Herdtweck, E. *Dalton. Trans.* **2014**, *43*, 13259–13269.
(6) Reithmeier, R. O.; Meister, S.; Siebel, A.; Rieger, B. *Dalton Trans.* **2015**, *44*, 6466–6472.
(7) Obara, S.; Itabashi, M.; Okuda, F.; Tamaki, S.; Tanabe, Y.; Ishii, Y. *Inorg. Chem.* **2006**, *45*, 8907–8921.
(8) Juris, A.; Valzani, V.; Barigelletti, F.; Campagna, S.; Belser, P.; von Zelewsky, A. *Coord. Chem. Rev.* **1988**, *84*, 85–277.

(9) Wolpher, H.; Johansson, O.; Abrahamsson, M.; Kritikos, M.; Sun, L.; Åkermark, B. *Inorg. Chem. Commun.* **2004**, *7*, 337–340.
(10) Abrahamsson, M.; Wolpher, H.; Johansson, O.; Larsson, J.; Kritikos, M.; Eriksson, L.; Norrby, P. O.; Bergquist, J.; Sun, L.; Åkermark, B.; Hammarström, L. *Inorg. Chem.* **2005**, *44*, 3215–3225.
(11) Abrahamsson, M.; Jager, M.; Osterman, T.; Eriksson, L.; Persson, P.; Becker, H.-C.; Johansson, O.; Hammarstrom, L. *J. Am. Chem. Soc.* **2006**, *128*, 12616–12617.
(12) Jager, M.; Kumar, R. J.; Gorls, H.; Bergquist, J.; Johansson, O. *Inorg. Chem.* **2009**, *48*, 3228–3238.
(13) Jager, M.; Eriksson, L.; Bergquist, J.; Johansson, O. *J. Org. Chem.* **2007**, *72*, 10227–10230.
(14) Abrahamsson, M.; Jager, M.; Kumar, R. J.; Osterman, T.; Persson, P.; Becker, H. C.; Johansson, O.; Hammarstrom, L. *J. Am. Chem. Soc.* **2008**, *130*, 15533–15542.
(15) Wang, J.; Chen, W.; Zuo, S.; Liu, L.; Zhang, X.; Wang, J. *Angew. Chem. Int. Ed.* **2012**, *51*, 12334–12338.
(16) Lowry, M. S.; Hudson, W. R.; Pascal, R. A.; Bernhard, S. *J. Am. Chem. Soc.* **2004**, *126*, 14129–14135.
(17) Do, H.-Q.; Daugulis, O. *J. Am. Chem. Soc.* **2008**, *130*, 1128–1129.
(18) Gaussian 09, Revision D.01, M. J. Frisch, G. W. Trucks, H. B. Schlegel, G. E. Scuseria, M. A. Robb, J. R. Cheeseman, G. Scalmani, V. Barone, G. A. Petersson, H. Nakatsuji, X. Li, M. Caricato, A. Marenich, J. Bloino, B. G. Janesko, R. Gomperts, B. Mennucci, H. P. Hratchian, J. V. Ortiz, A. F. Izmaylov, J. L. Sonnenberg, D. Williams-Young, F. Ding, F. Lipparini, F. Egidi, J. Goings, B. Peng, A. Petrone, T. Henderson, D. Ranasinghe, V. G. Zakrzewski, J. Gao, N. Rega, G. Zheng, W. Liang, M. Hada, M. Ehara, K. Toyota, R. Fukuda, J. Hasegawa, M. Ishida, T. Nakajima, Y. Honda, O. Kitao, H. Nakai, T. Vreven, K. Throssell, J. A. Montgomery, Jr., J. E. Peralta, F. Ogliaro, M. Bearpark, J. J. Heyd, E. Brothers, K. N. Kudin, V. N. Staroverov, T. Keith, R. Kobayashi, J. Normand, K. Raghavachari, A. Rendell, J. C. Burant, S. S. Iyengar, J. Tomasi, M. Cossi, J. M. Millam, M. Klene, C. Adamo, R. Cammi, J. W. Ochterski, R. L. Martin, K. Morokuma, O. Farkas, J. B. Foresman, and D. J. Fox, Gaussian, Inc., Wallingford CT, 2016.
(19) Hanwell, M. D.; Curtis, D. E.; Lonie, D. C.; Vandermeersch, T.; Zurek, E.; Hutchison, G. R. *J. Cheminform.* **2012**, *4*, 17.
(20) O'Boyle, N. M.; Tenderholt, A. L.; Langner, K. M. *J. Comp. Chem.* **2008**, *29*, 839–845.
(21) Connelly, N. G.; Geiger, W. E. *Chem. Rev.* **1996**, *96*, 877–910.
(22) Caspar, J. V; Meyer, T. J. *J. Am. Chem. Soc.* **1983**, *105*, 5583–5590.
(23) Cline, E. D.; Adamson, S. E.; Bernhard, S. *Inorg. Chem.* **2008**, *47*, 10378–10388.
(24) Ventre, S.; Petronijevic, F. R.; Macmillan, D. W. C. *J. Am. Chem. Soc.* **2015**, *137*, 5654–5657.
(25) Sun, J.; Zhao, J.; Guo, H.; Wu, W. *Chem. Commun.* **2012**, *48*, 4169.
(26) Brooks, A. C.; Basore, K.; Bernhard, S. *Inorg. Chem.* **2013**, *52*, 5794–5800.
(27) Constable, E. C.; Hostettler, N.; Housecroft, C. E.; Kopecky, P.; Neuburger, M.; Zampese, J. A. *Dalt. Trans.* **2012**, *41*, 2890.
(28) Sato, S.; Morikawa, T.; Kajino, T.; Ishitani, O. *Angew. Chemie - Int. Ed.* **2013**, *52*,

988–992.
(29) Goldsmith, J. I.; Hudson, W. R.; Lowry, M. S.; Anderson, T. H.; Bernhard, S. *J. Am. Chem. Soc.* **2005**, *127*, 7502–7510.
(30) Kalyanasundaram, K. *Photochemistry of Polypyridine and Porphyrin Complexes*; Academic Press: New York, 1992.
(31) Prier, C. K.; Rankic, D. A.; MacMillan, D. W. C. *Chem. Rev.* **2013**, *113*, 5322–5363.
(32) Johnson, A. L. *J. Org. Chem.* **1982**, *47*, 5220–5222.
(33) Xia, J.-B.; Zhu, C.; Chen, C. *Chem. Commun.* **2014**, *50*, 11701–11704.
(34) Tinker, L. L.; McDaniel, N. D.; Curtin, P. N.; Smith, C. K.; Ireland, M. J.; Bernhard, S. *Chem. Eur. J.* **2007**, *13*, 8726–8732.
(35) Curtin, P. N.; Tinker, L. L.; Burgess, C. M.; Cline, E. D.; Bernhard, S. *Inorg. Chem.* **2009**, *48*, 10498–10506.
(36) Zhou, J.; Gai, L.; Zhou, Z.; Mack, J.; Xu, K.; Zhao, J.; Qiu, H.; Chan, K. S.; Shen, Z. *RSC Adv.* **2016**, *6*, 72115–72120.
(37) Wang, J.; Lu, Y.; McGoldrick, N.; Zhang, C.; Yang, W.; Zhao, J.; Draper, S. M. *J. Mater. Chem. C.* **2016**, *4*, 6131–6139.
(38) Jiang, X.; Peng, J.; Wang, J.; Guo, X.; Zhao, D.; Ma, Y. *ACS Appl. Mater. Inter.* **2016**, *8*, 3591–3600.
(39) Maggioni, D.; Galli, M.; D'Alfonso, L.; Inverso, D.; Dozzi, M. V.; Sironi, L.; Iannacone, M.; Collini, M.; Ferruti, P.; Ranucci, E.; D'Alfonso, G. *Inorg. Chem.* **2015**, *54*, 544–553.
(40) Colombo, A.; Dragonetti, C.; Roberto, D.; Valore, A.; Ferrante, C.; Fortunati, I.; Picone, a. L.; Todescato, F.; Williams, J. a. G. *Dalton Trans.* **2015**, *44*, 15712–15720.
(41) Ashen-Garry, D.; Selke, M. *Photochem. Photobiol.* **2014**, *90*, 257–274.
(42) Sun, J.; Zhong, F.; Zhao, J. *Dalton Trans.* **2013**, *42*, 9595–9605.

Chapter 4. Phenanthroline Hemicage Metal Complexes

4.1 Introduction

In order for platinum-group metals like Ru and Ir to continue to find uses in a wide array of applications, they need to be able to surmount their increasingly high costs and low abundance compared to the more earth-abundant metals like Fe and Zn (Figure 4-1).[1] While properties like tunability of their photophysical, electrochemical, and catalytic properties make them continue to be useful, issues such as thermal, electrochemical, and environmental stability are continuing to make their large-scale implementation seem less and less worthwhile.

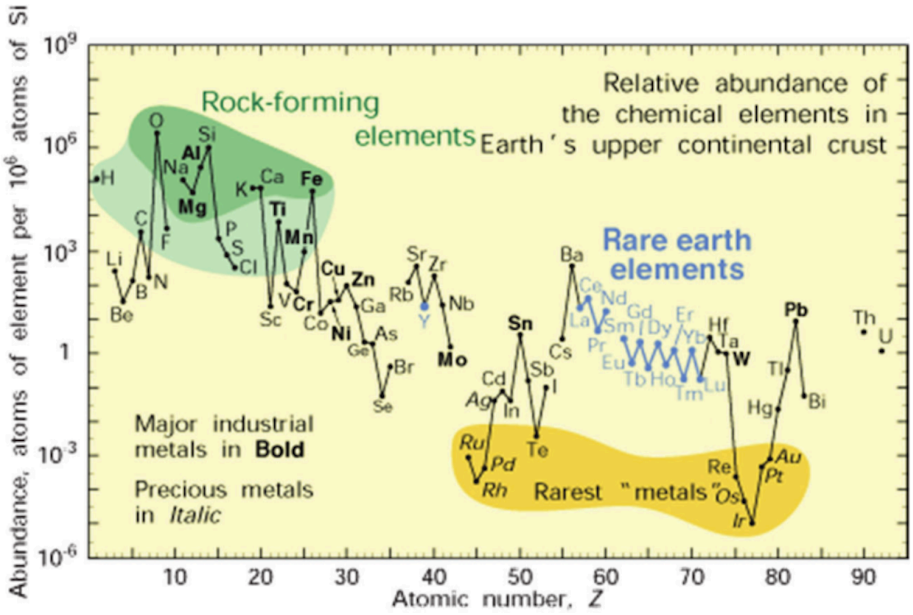

Figure 4-1 Abundance (expressed as atoms of element per 106 atoms of Si) of chemical elements in the Earth's upper crust as a function of atomic number. Reprinted with permission from ref 1. Copyright 2014 The Royal Society of Chemistry.

A notable example of this problem can be found when looking at the use of $[Ru(bpy)_3]^{2+}$ in OLEDs. While the complex can be easily synthesized and derivatized,[2] it continues to suffer from issues with stability. It has been shown that in an OLED, the

external quantum efficiency of a device using $[Ru(bpy)_3]^{2+}$ decreases with time (Figure 4-2).[3] This was attributed to the degradation of the complex and none of the other factors in the device.

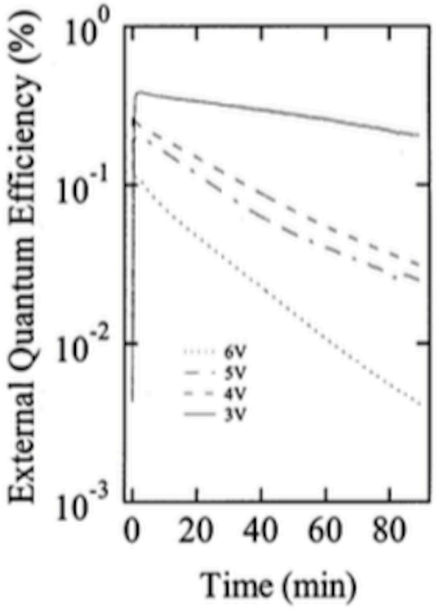

Figure 4-2 External quantum efficiency of a $[Ru(bpy)_3](PF_6)_2$ device as a function of time. Reprinted with permission from ref 3. Copyright 2002 American Chemical Society.

Furthermore, when used in photochemical applications, $[Ru(bpy)_3]^{2+}$ has been shown to degrade through ligand dissociation upon excitation (Figure 4-3).[4] When the complex is thermally excited to its ^{3}MC from the ^{3}MLCT state, rather than relaxing back to the ground state, the bonding from the ligand to the metal center is weakened, which can cause the ligand to partially dissociate. In the presence of coordinating species, the vacant site can be occupied, preventing the ligand from coordinating again. Eventually, the entire ligand would dissociate and render the complex photochemically inactive as a result.

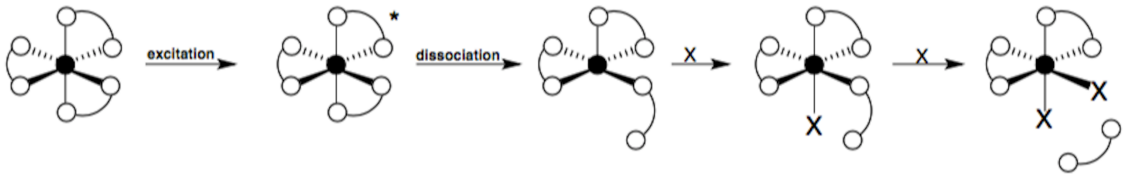

Figure 4-3 Ligand dissociation mechanism of $[Ru(bpy)_3]^{2+}$.

One strategy that has been employed to minimize ligand dissociation in metal complexes has been the use of hemicaging ligands, which tether three bidentate ligands together such that complete dissociation is minimized given the retention of the ligand within the coordination sphere of the metal. In addition, the increased rigidity of the complex is expected to lower non-radiative pathways of decay of the complexes' excited states such that quantum yields and excited state lifetimes are significantly improved. Work within the Bernhard lab has used hemicaging bipyridyl ligands on ruthenium, zinc, as well as hemicaging 8-hydroxyquinoline ligands on aluminum, gallium, and indium centers and observed improved excited state lifetimes and quantum yields of the complexes.[5,6] Other hemicaged complexes of ruthenium and iridium have been synthesized, studied and obtained similar photophysical results.[7–12]

In terms of ligand structure, the use of a benzene "cap" has been shown to provide a more favorable complexation of the metal center due to pre-organization of the ligands at the 1, 3, and 5 positions on the benzene ring. This also provides ample space for the ligands to properly orient themselves and minimize steric crowding. Further organization can be given by introducing alkyl groups on the 2,4 and 6 positions to entropically favor the complex formation.[13]

This chapter presents unpublished work aimed towards synthesizing a hemicaging ligand that contains three phenanthrolines, a central benzene cap, and substitution at the 3-position of the phenanthroline to allow for optimal coordination and minimal

polymerization of the ligand with metal centers. The use of a phenanthroline over bipyridine was expected to further increase quantum efficiency and stability. The development of a synthetic protocol and assessment of methods that failed will be presented. Subsequent complexation of the ligands to Fe(II), Zn(II) and Ru(II) was performed and the complexes were characterized photophysically and electrochemically to determine the effects of the phenanthroline hemicaging ligand structure.

4.2 Experimental

4.2.1 General

All reagents were used as received, with the exception of 1,2-phenylenediamine, which was purified by recrystallization from a 1% aqueous sodium dithionite solution with activated charcoal. Anhydrous triethylamine was obtained from a JC Meyer Solvent System. Reactions with phenanthroline products were monitored by TLC using an iron sulfate stain to visualize the phenanthrolines as a red spot. ^{1}H and ^{13}C NMR spectra were recorded on 300 and 500 MHz Bruker Avance spectrometers. ESI-MS was performed with 100 μM solutions in MeOH, EtOH, or CH_3CN using a Thermo-Fisher LCQ Instrument.

4.2.2 Synthetic Procedures

3-bromo-8-nitroquinoline. This procedure was adapted from the bromination of 1,10-phenanthroline by Saitoh *et. al*.[14] To a 500 mL round-bottom flask equipped with a reflux condenser was added 1-chlorobutane (250 mL) and 8-nitroquinoline (12.501 g, 71.773 mmol). The suspension was heated to 60 ^{o}C, at which point the 8-nitroquinoline was fully dissolved. Disulfur dichloride, S_2Cl_2 (6.35 mL, 10.661 g, 78.950 mmol) was added via an additional funnel dropwise, followed by pyridine (6.40 mL, 6.249 g, 78.950 mmol)

to give a cloudy yellow solution. Bromine (4.10 mL, 12.617 g, 78.950 mmol) was then added dropwise through an addition funnel, and the solution was heated to 95 ^{o}C for five hours. Once cooled to room temperature, 100 mL of hexanes was added and the flask was cooled to 0 ^{o}C. The solid that formed was filtered and washed with hexanes to give 14.830 g (82% yield) of a white solid. ^{1}H NMR (300 MHz, $CDCl_3$): δ 8.99 (d, J = 2.4 Hz, 1H), 8.40 (d, J = 2.1 Hz, 1H), 8.04 (dd, J = 7.5 Hz, 1.5 Hz, 1H), 7.96 (dd, J = 8.4 Hz ,1.2 Hz, 1H), 7.65 (dd, J = 8.1 Hz, 8.4 Hz, 1H) . ^{13}C NMR (126 MHz, $CDCl_3$): δ 153.55, 148.13, 137.43. 137.34, 131.18, 129.69, 126.69, 124.01, 119.24. ESI-MS (*m/z* ESI, MeOH) Calculated 252.9 $[M+H]^+$ Found 253.0 $[M+H]^+$.

3-bromo-8-aminoquinoline. To a 500 mL round-bottom flask fitted with a reflux condenser was added H_2O (84 mL), EtOH (168 mL), AcOH (168 mL), and 12 M HCl (6 mL). To this was added 3-bromo-8-nitroquinoline (10.231 g, 40.429 mmol), followed by iron filings (18.232 g, 309.820 mmol). The brown solution was heated to 120 ^{o}C for two hours. Once cooled to room temperature, the solution was filtered through Celite. The filtrate was diluted with 1 L of H_2O, which yielded a precipitate that was extracted with Et_2O. The Et_2O was carefully washed with saturated $NaHCO_3$ (until CO_2 evolution ceased), H_2O, and saturated NaCl. The Et_2O was dried over Na_2SO_4 and evaporated to get 8.205 g (91% yield) of 3-bromo-8-aminoquinoline as a yellow solid. Note: the product was stored in the dark, under argon to minimize oxidation. ^{1}H NMR (300 MHz, $CDCl_3$): δ 8.67 (d, J = 2.1 Hz, 1H), 8.10 (d, J = 2.4 Hz, 1H), 7.27 (t, J = 7.8 Hz, 1H), 6.95 (dd, J = 8.4 Hz, 0.9 Hz, 1H), 6.84 (dd, J = 7.2 Hz, 1.2 Hz, 1H), 4.95 (br s, 2H). ^{13}C NMR

(126 MHz, $CDCl_3$): δ 148.14, 144.20, 137.06, 136.25, 129.81, 128.71, 117.58, 114.99, 110.36 . MS (*m/z* ESI, MeOH) Calculated 222.9 $[M+H]^+$ Found 223.1 $[M+H]^+$.

3-bromo-8-isopropyl-1,10-phenanthroline. To a 100 mL round-bottom flask fit with a reflux condenser was added H_2O (9.9 mL) and H_2SO_4 (17.47 mL, 314.5 mmol). Note: the amount of H_2SO_4 used is critical to optimal reaction yields. A portion of NaI (312 mg, 2.081 mmol) was added, followed by 3-bromo-8-aminoquinoline (16.838 g, 75.483 mmol). The brown, viscous solution was heated to 110 ^oC, at which point 3-methy-2-methylenebutanal (12.347 g, 125.805 mmol) was added via syringe pump over five hours. Halfway through the addition, a second portion of NaI (317 mg, 2.114 mmol) was added to the reaction mixture. Once the addition was complete, the reaction was heated for an additional hour and then cooled to room temperature. Reaction progress was monitored using TLC and an iron sulfate staining solution. The reaction mixture was poured into H_2O, and made basic with 6M NaOH. The cloudy solution was extracted three times with CH_2Cl_2. The volume was reduced to ~100 mL, activated charcoal was added, and the solution was stirred for one hour. After filtration through Celite, the crude product was evaporated onto silica gel and chromatographed on silica gel using 25% pentanes in EtOAc, to yield a yellow-brown oil which solidified upon standing and drying in vacuo to give 8.562 g (38% yield) of 3-bromo-8-isopropyl-1,10-phenanthroline. ^1H NMR (300 MHz, $CDCl_3$) δ 9.14 (d, J = 2.3 Hz, 1H), 9.08 (d, J = 2.2 Hz, 1H), 8.33 (d, J = 2.3 Hz, 1H), 8.01 (d, J = 2.2 Hz, 1H), 7.77 (d, J = 8.8 Hz, 1H), 7.64 (d, J = 8.8 Hz, 1H), 3.22 (sept, 1H), 1.42 (d, J = 7.0 Hz, 6H). ^{13}C NMR (126 MHz, $CDCl_3$): δ 151.08,

150.99, 144.54, 144.32, 143.86, 137.35, 132.38, 129.27, 128.63, 128.03, 125.32, 119.37, 31.94, 23.74. MS (*m/z* ESI, MeOH) Calculated 301.0 $[M+H]^+$. Found 301.1 $[M+H]^+$.

1,3,5-tris((8-isopropyl-1,10-phenanthrolin-3-yl)ethynyl)benzene. To an oven-dried, 200 mL EPA-bottle with a silicone-septa cap was added 40 mL of anhydrous dimethylformamide, DMF, 40 mL of anhydrous triethylamine, 3-bromo-8-isopropyl-1,10-phenanthroline (4.969 g, 16.500 mmol), and 1,3,5-triethynylbenzene (751 mg, 5.000 mmol). The solution was degassed with three cycles of vacuum/argon, at which point tetrakis-triphenylphosphine palladium (0), $Pd(PPh_3)_4$ (867 mg, 0.750 mmol) and copper (I) iodide, CuI (157 mg, 0.825 mmol) were added. The solution was degassed with an additional two cycles of vacuum and argon. The reaction mixture was sonicated for one hour and then heated to 120 ^oC for twenty-four hours. Once cooled to room temperature, the reaction mixture was poured into ~600 mL of H_2O, which gave a beige precipitate which was isolated via vacuum filtration and washed with H_2O. The solid was then dissolved in $CHCl_3$ and concentrated to ~50 mL solvent volume. To this was added 400 mL of pentane, which gave a yellow-brown precipitate, which was isolated via vacuum filtration and washed with pentane. The crude product was then chromatographed on silica gel with $CHCl_3$ containing 3% triethylamine and 1% CH_3OH to obtain 3.855 g (95% yield) of 1,3,5-tris((8-isopropyl-1,10-phenanthrolin-3-yl)ethynyl)benzene. ^1H NMR (300 MHz, $CDCl_3$): δ 9.29 (d, J = 2.1 Hz, 3H), 9.11 (d, J = 2.4 Hz, 3H), 8.39 (d, J = 2.1 Hz, 3H), 8.03 (d, J = 2.1 Hz, 3H), 7.88 (s, 3H), 7.83-7.22 (m, 6H) 3.25 (sept, 3H), 1.44 (d, J = 7.2 Hz, 18H). MS (*m/z* ESI, CH_3CH_2OH) Calculated 811.4 $[M+H]^+$ Found 811.6 $[M+H]^+$.

*1,3,5-tris(2-(8-isopropyl-1,10-phenanthrolin-3-yl)ethyl)benzene (**1**).* To a 50 mL, three-necked round-bottom flask was added 1,3,5-tris((8-isopropyl-1,10-phenanthrolin-3-yl)ethynyl)benzene (150 mg, 0.185 mmol) and 20 mL of THF. To this was added 300 mg of LiOH dissolved in 7 mL of H_2O. The solution was degassed with three cycles of vacuum/argon. Under a positive pressure of argon, 70 mg of 10% palladium on carbon was added. The vessel was put under vacuum, followed by a balloon of hydrogen gas. The reaction mixture was stirred overnight. Reaction progress was monitored by TLC. After filtration of the reaction through Celite, the Celite was washed with THF and $CHCl_3$. The combined filtrates were evaporated to dryness, suspended in H_2O, and extracted with $CHCl_3$. Drying with Na_2SO_4 and evaporation of solvent gave 99 mg (65% yield) of **2** as a beige solid. ^{1}H NMR (300 MHz, $CDCl_3$): δ 9.04 (d, J = 2.1 Hz, 3H), 8.93 (br s, 3H), 7.96 (d, J = 2.1 Hz, 3H), 7.74 (d, J = 2.1 Hz, 3H), 7.72-7.65 (m, 6H) 6.78 (s, 3H), 3.18 (sept, 3H), 3.05-2.84 (m, 12H), 1.38 (d, J = 6.9 Hz, 18H). ^{13}C NMR (126 MHz, $CDCl_3$): δ 151.23, 150.46, 144.32, 144.26, 143.28, 141.15, 136.15, 135.20, 132.56, 128.36, 128.06, 127.03, 126.65, 126.39, 37.48, 35.29, 31.92, 23.79. MS (*m/z* ESI, CH_3CH_2OH) Calculated 823.4 $[M+H]^+$ Found 823.7 $[M+H]^+$.

*[Fe(**1**)](BF$_4$)$_2$.* To a 500 mL, three-neck round-bottom flask was added **2** (115 mg, 0.140 mg) in 250 mL of EtOH. In a separate 1 L flask, 34 mg (0.100 mmol) of $Fe(BF_4)_2 \cdot 6H_2O$ was dissolved in 100 mL of EtOH, fitted with condenser, and heated to 95^{o}C under argon. The ligand solution was cannulated into the metal solution via one of the additional necks over the course of 2 hours using a stainless steel cannula. Once the addition was

complete, the solution was heated for another twenty-four hours. Once cooled to room temperature, the solvent was evaporated, and the red solid was recrystallized by vapor diffusion of Et_2O into CH_3CN to produce 67 mg (64 % yield) of *[Fe(**2**)](BF$_4$)$_2$*. ^{1}H NMR (300 MHz, CD_3CN) δ 8.49 (dd, *J* = 5.7, 1.5 Hz, 6H), 8.17 (s, 6H), 7.48 (d, *J* = 1.6 Hz, 3H), 6.72 (s, 3H), 6.39 (d, *J* = 1.4 Hz, 3H), 3.22 (dd, *J* = 33.4, 12.9 Hz, 6H), 2.93 (sept, 3H), 2.77 (td, *J* = 13.0, 13.0, 3.2 Hz, 3H), 2.59 (td, *J* = 13.3, 13.3, 3.0 Hz, 3H), 1.11 (t, *J* = 6.4 Hz, 18H). MS (*m/z* ESI, CH_3CN) Calculated 439.2 [M^{2+}- 2 BF_4^-] 965.4 [M^{2+} - BF_4^-] Found 439.4 [M^{2+}- 2 BF_4^-] 965.1 [M^{2+} - BF_4^-].

*[Zn(**1**)](BF$_4$)$_2$.* To a 250 mL round-bottom flask was added **2** (77 mg, 0.093 mmol) in 100 mL of EtOH. To this was added 33 mg (0.093 mmol) of $Zn(BF_4)_2$ •$6.5H_2O$, and the solution was heated to 95 ^oC for twenty-four hours. The solution was cooled, and the solvent was removed in vacuo to produce an off-white solid. The solid was suspended in 40 mL of H_2O, filtered, washed with H_2O, and dried. The solid was recrystallized by vapor diffusion of pentanes into acetone to obtain 77 mg (78% yield) of $[Zn(2)](BF_4)_2$ as an off-white solid. ^{1}H NMR (300 MHz, Acetone) δ 8.85 (dd, *J* = 11.7, 2.0 Hz, 6H), 8.58 (d, *J* = 2.1 Hz, 3H), 8.28 (s, 6H), 7.12 (d, *J* = 1.9 Hz, 3H), 6.99 (s, 3H), 3.41 – 3.23 (m, 6H), 3.14 (sept, 3H), 3.04 – 2.89 (m, 3H), 2.79 – 2.71 (m, 3H), 1.23 (dd, *J* = 23.5, 6.9 Hz, 18H). MS (*m/z* ESI, CH_3CN) Calculated 443.1 [M^{2+}- 2 BF_4^-] 973.4 [M^{2+} - BF_4^-] Found 443.4 [M^{2+}- 2 BF_4^-] 973.1 [M^{2+} - BF_4^-].

*[Ru(**1**)](PF$_6$)$_2$.* To a 1 L round-bottom flask was added 132 mg (0.217 mmol) of $RuCl_2(DMSO)_4$ in 650 mL of EtOH. The flask was fitted with a condenser and heated to

95 ^{o}C under argon. A 250 mg (0.303 mmol) portion of **2** was dissolved in 50 mL of EtOH and delivered via syringe pump over twelve hours. The reaction mixture was heated for an additional 6 hours and then cooled to room temperature. The solvent was removed in vacuo; the brown solid was sonicated in 50 mL of H_2O, and filtered through Celite to obtain an orange filtrate. Upon the addition of excess NH_4PF_6, an orange precipitate formed and was isolated by vacuum filtration. The solid was dissolved in a minimum amount of CH_3CN, and purified by preparative thin-layer chromatography on silica gel with 4% H_2O and 2% saturated aqueous NH_4PF_6 in CH_3CN. The product was isolated by washing the silica gel from the topmost, orange luminescent band with 4% H_2O in CH_3CN and evaporating to dryness to yield 21 mg (6% yield) of [Ru(**2**)]$(PF_6)_2$. ^{1}H NMR (300 MHz, CD_3CN) δ 8.43 (d, *J* = 1.9 Hz, 6H), 8.12 (d, *J* = 1.2 Hz, 6H), 7.94 (d, *J* = 1.9 Hz, 3H), 6.78 – 6.63 (m, 6H), 3.32 – 3.05 (m, 6H), 2.95 (sept, 3H), 2.80 (td, *J* = 13.3, 13.3, 3.6 Hz, 3H), 2.57 (td, *J* = 13.5, 13.4, 3.4 Hz, 3H), 1.14 (dd, *J* = 17.8, 7.1 Hz, 18H). Due to poor reaction yields and difficulty of ligand synthesis, quantities sufficient for ^{13}C NMR analysis could not be obtained. MS (*m/z* ESI, CH_3CN) Calculated 462.4 [M^{2+}- 2 PF_6^-] 1069.3 [M^{2+} - PF_6^-] Found 462.3 [M^{2+}- 2 PF_6^-] 1069.3 [M^{2+} - PF_6^-].

3,8-diisopropyl-1,10-phenanthroline. *o*-Phenylenediamine (1.722g, 15.9 mmol) and NaI (24 mg, 0.159 mmol) were added to H_2SO_4 (2.60 mL) and H_2O (1.50 mL) and the mixture was heated to 110 ºC. 3-methyl-2-methylenebutanal (5.00 g, 5.95 mL, 52 mmol) was added to the reaction via syringe pump over five hours, with a second NaI portion halfway through the addition. After the addition was complete, an additional portion of NaI was added and the solution was heated overnight. The reaction mixture was cooled to

room temperature and poured into deionized water. The solution was then neutralized with solid Na_2CO_3 and basified with 6M NaOH. The reaction mixture was extracted with three times with CH_2Cl_2. The combined organic layers were washed once with brine and dried with Na_2SO_4. Volume was reduced to ~100 mL, activated charcoal was added and the mixture was stirred for one hour. After filtering through Celite, the crude product was evaporated onto silica gel and chromatographed using 25% pentanes in EtOAc to give the final product as a brown oil (244mg, 6 % yield). ^{1}H NMR (500 MHz, $CDCl_3$): δ 9.03 (d, J = 2.25 Hz, 2H), 7.98 (d, J = 2.22 Hz, 2H), 7.71 (s, 2H), 3.19 (sept, 2H), 1.39 (d, J = 6.93 Hz, 12H). ^{13}C NMR (210 MHz, $CDCl_3$): δ 150.40, 144.63, 142.91, 132.17, 128.14, 126.40, 31.81, 23.74. MS (*m/z* ESI, CH_3CH_2OH) Calculated 265.2 $[M+H]^+$ Found 265.2 $[M+H]^+$.

*[Fe(**2**)$_3$](BF$_4$)$_2$*. A minimum volume of methanol was added to the ligand (100 mg, 0.378 mmol), and a minimum volume of water was added to $Fe(BF_4)_2 \cdot 6H_2O$ (40 mg, 0.118 mmol). The two solutions were stirred together for 1 h at room temperature, after which excess aqueous NH_4BF_4 was added and a red precipitate was formed. The precipitate was isolated by vacuum filtration and recrystallized by vapor diffusion of Et_2O into CH_3CN to obtain 99 mg (82% yield) of $[Fe(\mathbf{1})_3](BF_4)_2$ as a red solid. ^{1}H NMR (500 MHz, d_6-acetone): δ 8.73 (br s, 6H), 8.35 (br s, 6H), 7.74 (s, 6H), 3.00 (sept, 6H), 1.12 (t, J = 7.28 Hz, 36H). ^{13}C NMR (210 MHz, d_6-acetone): δ 154.62, 148.60, 146.81, 134.70, 130.06, 128.15, 31.55, 23.16, 22.16. MS (*m/z* ESI, CH_3CN) Calculated 424.4 $[M^{2+} - 2\ BF_4^-]$ 935.6 $[M^{2+} - BF_4^-]$ Found 424.2 $[M^{2+} - 2\ BF_4^-]$ 934.9 $[M^{2+} - BF_4^-]$.

*[Zn(**2**)$_3$](BF$_4$)$_2$.* A minimum volume of methanol was added to the ligand (100 mg, 0.378 mmol), and a minimum volume of water was added to $Zn(BF_4)_2 \cdot 6.5H_2O$ (42 mg, 0.118 mmol) for dissolution. The two solutions were stirred together for 1 h at room temperature, after which additional aqueous NH_4BF_4 was added and a beige precipitate was seen. The precipitate was isolated by vacuum filtration and then recrystallized by vapor diffusion of pentanes into acetone to obtain 82 mg (67 % yield) of $[Zn(1)_3](BF_4)_2$ as an off white solid. ^{1}H NMR (500 MHz, d_6-acetone): δ 8.86 (d, J = 1.5 Hz, 6H), 8.34 (d, J = 1.7 Hz, 6H), 8.31 (s, 6H), 3.13 (sept, 6H), 1.21 (br s, 36H). ^{13}C NMR (210 MHz, d_6-acetone): δ 147.93, 146.45, 139.50, 137.52, 129.81, 127.85, 31.42, 22.91, 22.44. MS (*m/z* ESI, CH_3CN) Calculated 428.4 [M^{2+}- 2 BF_4^-] 943.6 [M^{2+} - BF_4^-] Found 428.1 [M^{2+}- 2 BF_4^-] 942.7 [M^{2+} - BF_4^-].

*[Ru(**2**)$_3$](PF$_6$)$_2$.* Ethylene glycol (6 mL) was combined with ligand (50 mg, 0.189 mmol) and $RuCl_3 \cdot 3H_2O$ (16.48 mg, 0.063 mmol) in a 50 mL pear flask. This solution was microwaved at 2 min intervals for 10 min. The solution was allowed to cool to room temperature and was poured into 30 mL of water. Excess NH_4PF_6 was added and a dark orange precipitate was seen. The precipitate was isolated by vacuum filtration and then recrystallized twice by vapor diffusion of Et_2O into a CH_3CN to obtain 55 mg (74 % yield) of $[Ru(1)_3](PF_6)_2$ as an orange solid. ^{1}H NMR (500 MHz, d_6-acetone): δ 8.68 (br s, 6H), 8.33 (br s, 6H), 8.14 (s, 6H), 3.00 (sept, 6H), 1.15 (t, J = 6.70 Hz, 36H). ^{13}C NMR (210 MHz, d_6-acetone): δ 151.30, 146.80, 146.78, 133.91, 130.59, 128.14, 31.48, 23.12, 22.14. MS (*m/z* ESI, CH_3CN) Calculated 447.2 [M^{2+}- 2 PF_6^-] 1039.4 [M^{2+} - PF_6^-] Found 447.4 [M^{2+}- 2 PF_6^-] 1039.3 [M^{2+} - PF_6^-].

8,8',8''-((2,4,6-trimethylbenzene-1,3,5-triyl)tris(ethyne-2,1-diyl))tris(3-isopropyl-1,10-phenanthroline). To an oven-dried, 40 mL EPA-vial was added 10 mL of anhydrous DMF, 10 mL of anhydrous triethylamine, 3-bromo-8-isopropyl-1,10-phenanthroline (1.012 g, 3.360 mmol), and 1,3,5-triethynyl-2,4,6-trimethylbenzene (195 mg, 1.018 mmol). The solution was degassed with three cycles of vacuum/argon, at which point $Pd(PPh_3)_4$ (176 mg, 0.152 mmol) and CuI (30 mg, 0.152 mmol) were added. The solution was degassed with an additional two cycles of vacuum and argon. The reaction mixture was sonicated for one hour and then heated to 120 ^oC for twenty-four hours. Once cooled to room temperature, the reaction mixture was poured into ~150 mL of H_2O and sonicated. A yellow precipitate was isolated via vacuum filtration and washed with H_2O. The solid was then dissolved in $CHCl_3$ and concentrated to ~50 % the original solvent volume. To this was added an excess of hexanes, which gave a yellow precipitate, which was isolated via vacuum filtration and washed with hexanes. The crude product was then chromatographed on alumina with 10% MeOH in $CHCl_3$ to obtain 763 mg (88% yield) of 8,8',8''-((2,4,6-trimethylbenzene-1,3,5-triyl)tris(ethyne-2,1-diyl))tris(3-isopropyl-1,10-phenanthroline. ^1H NMR (300 MHz, $CDCl_3$) δ 9.21 (d, J = 46.7 Hz, 6H), 8.36 (s, 3H), 8.02 (s, 3H), 7.73 (s, 6H), 3.25 (sept, 3H), 2.92 (s, 9H), 1.45 (d, J = 6.9 Hz, 18H). MS (*m/z* ESI, EtOH) Calculated 853.3 $[M+H]^+$ Found 853.6 [M+H].

*8,8',8''-((1Z,1'Z,1''Z)-(2,4,6-trimethylbenzene-1,3,5-triyl)tris(ethene-2,1-diyl))tris(3-isopropyl-1,10-phenanthroline) (**3**)*. To a 100 mL, three-necked round-bottom flask was added 8,8',8''-((2,4,6-trimethylbenzene-1,3,5-triyl)tris(ethyne-2,1-diyl))tris(3-isopropyl-

1,10-phenanthroline (520 mg, 0.609 mmol) and 40 mL of THF. To this was added 900 mg of LiOH dissolved in 14 mL of H_2O. The solution was degassed with three cycles of vacuum/argon. Under a positive pressure of argon, 270 mg of 10% palladium on carbon was added. The vessel was put under vacuum, followed by a balloon of hydrogen gas. The reaction mixture was stirred overnight. After filtration of the reaction through Celite, the Celite was washed with THF and $CHCl_3$. The combined filtrates were evaporated to dryness, suspended in H_2O, and extracted with $CHCl_3$. After drying with Na_2SO_4 and evaporation of solvent, the product was passed through a short silica gel plug with 100/2.5/1 CH_2Cl_2:MeOH/triethylamine, which gave 252 mg (48% yield) of **3** as a yellow solid. ^{1}H NMR (500 MHz, $CDCl_3$) δ 8.20 – 8.06 (m, 9H), 7.88 – 7.81 (m, 6H), 7.76 (d, *J* = 2.1 Hz, 3H), 6.88 – 6.79 (m, 6H), 2.89 (sept, 3H), 1.99 (s, 9H), 1.16 (dd, *J* = 35.3, 6.7 Hz, 18H). ^{13}C NMR (126 MHz, $CDCl_3$) δ 148.57, 148.53, 144.09, 143.98, 143.88, 135.81, 135.37, 133.59, 133.45, 133.08, 133.02, 129.03, 128.61, 128.31, 127.10, 77.41, 77.16, 76.91, 31.93, 24.13, 23.30, 17.94. MS (*m/z* ESI, EtOH) Calculated 865.5 $[M+Li]^+$ Found 867.9 $[M+Li]^+$.

*[Zn(**3**)](BF$_4$)$_2$.* To a 100 mL round-bottom flask was added **3** (25 mg, 0.029 mmol) in 50 mL of EtOH. To this was added 10 mg (0.029 mmol) of $Zn(BF_4)_2$ •$6.5H_2O$, and the solution was heated to 95 ^{o}C for twenty-four hours. The solution was cooled, and the solvent was removed in vacuo to produce an off-white solid. The solid was suspended in acetone, filtered through a pipette filter, and dried. The solid was recrystallized by vapor diffusion of ether into acetonitrile to obtain 29 mg (93 % yield) of [Zn(**3**)]$(BF_4)_2$ as an off-white solid. ^{1}H NMR (500 MHz, Acetone) δ 8.86 (dd, J = 12.0, 1.7 Hz, 6H), 8.29 (s,

6H), 8.00 (d, J = 2.0 Hz, 3H), 7.87 (d, J = 1.8 Hz, 3H), 7.07 (q, J = 11.7, 11.7, 11.7 Hz, 6H), 3.07 (sept, 3H), 2.01 (s, 9H), 1.19 (t, J = 6.5, 6.5 Hz, 18H). ^{13}C NMR (126 MHz, Acetone) δ 206.26, 148.54, 148.48, 147.50, 140.58, 140.46, 140.13, 138.72, 136.38, 135.79, 135.16, 134.45, 131.18, 130.84, 129.02, 128.92, 128.54, 32.46, 24.17, 23.23, 18.17. MS (*m/z* ESI, EtOH) Calculated: 461.2 [M^{2+}- 2 BF_4^-] 1009.4 [M^{2+} - BF_4]. Found: 461.4 [M^{2+}- 2 BF_4] 1009.1 [M^{2+} - BF_4^-].

4.2.3 Electrochemical Characterization

Cyclic voltammetry experiments were performed using a CH-Instruments Electrochemical Analyzer 600C potentiostat with a three-electrode system consisting of a platinum coil counter electrode, a silver wire pseudo-reference, and a 1 mm^2 platinum disk working electrode. Scans were performed with positive scan polarity, at 0.10 V/S, under an atmosphere of argon, using argon-purged acetonitrile solutions that contained 0.10 M tetra-*n*-butylammonium hexafluorophosphate as the supporting electrolyte and 0.5 mM of the analyte. An internal standard of ferrocene was added to each solution, referencing potentials to SCE via the oxidation of ferrocene at 0.40 V.[15]

4.2.4 Photophysical Characterization

Photophysical measurements were carried out on argon-degassed 25 μM solutions in CH_3CN at room temperature, using 1 cm quartz cuvettes that were capped with septa. Absorption spectra were recorded using a Shimadzu UV-1800 spectrophotometer. Emission spectra were recorded using a Fluorolog-3 spectrophotometer equipped with dual monochromators and a photomultiplier tube at a right-angle geometry. All Ru complexes were excited at 450 nm, whereas Zn complexes and quinine sulfate were excited at 320 nm. Excited state lifetimes were determined using a 337 nm pulsed

Stanford Research Systems NL 100 N_2 laser, where emission decays were monitored with an oscilloscope and converted into a linear regression using a Labview interface. Quantum yields were determined using a 30 μM solution of $[Ru(bpy)_3](PF_6)_2$ in CH_3CN ($\phi_r = 0.062$) as a reference for the Ru complexes, and a 25 μM solution of quinine in 0.5 M H_2SO_4 ($\phi_r = 0.546$) as a reference for the Zn complexes. The equation used to determine quantum yields was as follows: $\phi_s = \phi_r(\eta_s^2/\eta_r^2)(I_s/I_r)(A_r/A_s)$, where η represents the refractive index of the solvent used, I represents the maximum emission intensity, and A represents the absorption at the excitation wavelength. Radiative decay constants (k_r) were calculated using the equation $k_r = (\Phi_s/\tau_s)$ where τ_s is the excited state lifetime of the sample and subsequently nonradiative decay constants (k_{nr}) were calculated using the relationship $k_{nr} = (1/\tau_s) - kr$. Emission intensities were corrected for the detector's response over the spectral range.

4.3 Results & Discussion

4.3.1 Synthesis

Hemicaging ligands of bipyridine and phenylpyridine have already been shown to minimize ligand dissociation from metal complexes and improve their photophysical properties.[5,6,8,9,11,16–18] In addition, the rigidity of a phenanthroline ligand when compared to a bipyridine and phenylpyridine has also been shown to improve photophysical efficiency of their complexes.[2,4,19] By marrying the two different structures and creating a hemicaging, phenanthroline based ligand, investigations into the overall improvement of its metal complexes as luminophores could be performed.

A previously established synthetic strategy towards hemicaging ligands involved the deprotonation of a methylated bipyridine ligand using lithium diisopropylamide,

followed by nucleophilic substation with a brominated aryl cap.[5] To make the phenanthroline based hemicage, reactions using the corresponding methylated phenanthroline were used, however the final product could not be isolated (Scheme 4-1). In an attempt to introduce additional stability, a phenyl-methyl phenanthroline was also attempted, but did not produce the desired product either. Upon further review, the 3-position of phenanthroline is resistant to deprotonation[20–22] compared to the 2-[23] and 4-positions,[11] which have been used previously.

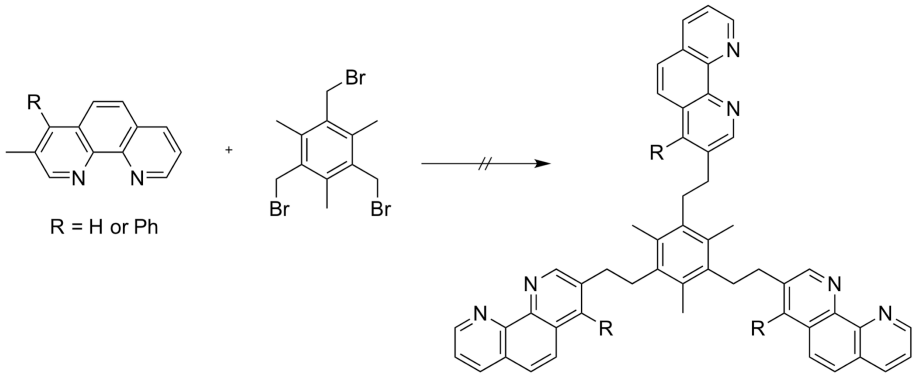

Scheme 4-1. Attempted alkylations of 3-methylphenanthrolines towards a phenanthroline hemicaging ligand.

Given the lack of success of the nucleophilic substitution method, another synthetic pathway involving cross-coupling reactions was pursued. Work by Colman *et. al*.[8] demonstrated that a phenylpyridine hemicage could be synthetized via a Sonogashira coupling reaction, followed by a Pd/C catalyzed reduction with H_2. While this procedure required installation of the alkyne to the phenylpyridine before coupling to the aryl cap, it was also envisioned that the synthesis could couple a tris-alkynyl benzene to the corresponding ligand, followed by reduction. To pursue this method, a brominated phenanthroline was necessary.

While there are published bromination procedures for phenanthroline that are selective for the 3-position,[14,24] these reactions unfortunately suffer from overbromination to the dibrominated product, as well as underbromination leaving unreacted starting material. Separation of those three compounds was possible, but this resulted in diminished yields of the desired monobrominated product. Subsequently, while the Sonogashira coupling reaction was successful, the tris-alkyne product proved insoluble, and could not be hydrogenated (Scheme 4-2). Therefore, the installation of solubilizing groups to the phenanthroline was pursued.

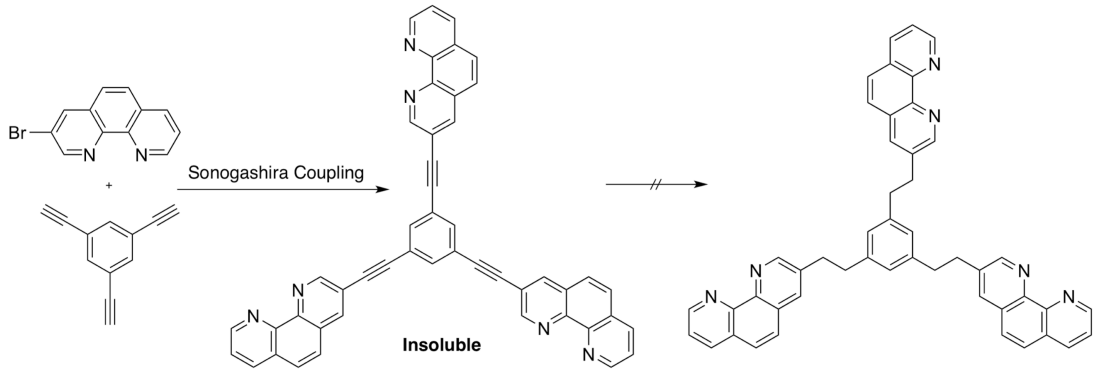

Scheme 4-2. Attempted synthesis of phenanthroline hemicage ligand via Sonogashira Coupling and Alkyne Hydrogenation.

Ultimately, synthesizing a phenanthroline with the bromine already installed along with a solubilizing alkyl group was pursued. Bromination of 8-nitroquinoline, followed by reduction of the nitro group was a highly scalable, selective protocol to arrive at 3-bromo-8-aminoquinoline, as shown in Scheme 4-3. This was subsequently reacted with 3-methyl-2-methylenebutanal to produce 3-bromo-8-isopropylphenanthroline. Subsequent coupling and reduction furnished the desired hemicaging ligand (**1**). It's worth noting that the addition of LiOH and H_2O were necessary to drive the hydrogenation.[25] Synthesis of the Ru(II) and Fe(II) complexes was

accomplished by slow addition of a dilute ligand solution to the corresponding metal precursor with heat. Column chromatography was used to remove the polymeric by-products for the reaction with Ru. The Zn(II) and Fe(II) complexes were more accessible since they did not require chromatography prior to recrystallization.

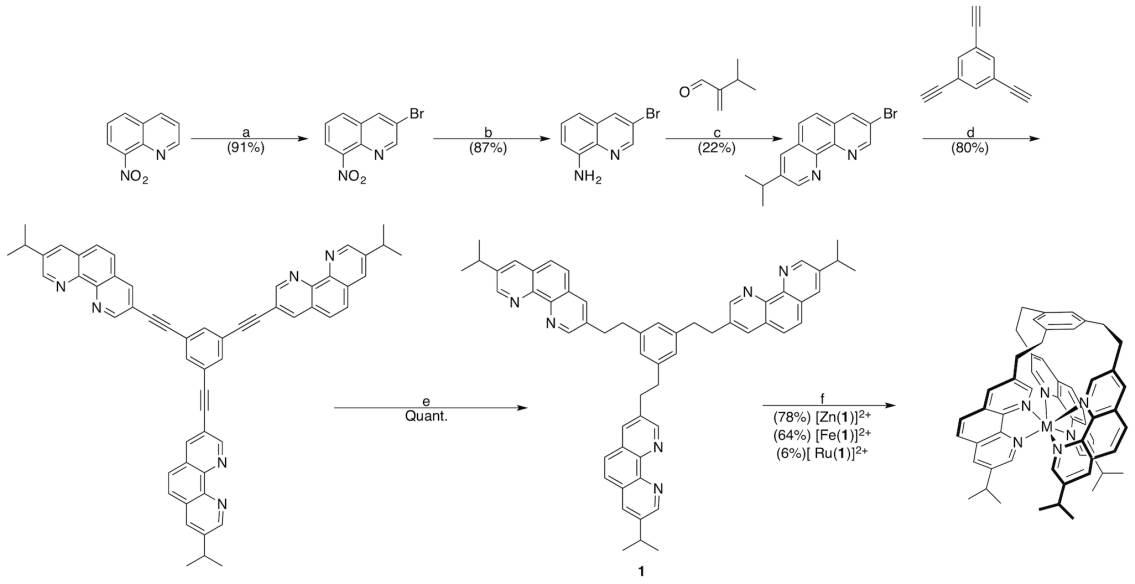

Scheme 4-3. Synthesis of phenanthroline hemicaging ligand **1** and its corresponding metal complexes. Reaction conditions as follows: a) S_2Cl_2, Chlorobutane, Pyridine, Br_2, 95 ^oC, 5 h. b) Fe, AcOH, EtOH, H_2O, HCl, 120 ^oC, 2 h. c) H_2O, H_2SO_4, NaI, 110 ^oC, 5 h. d) $Pd(PPh_3)_4$, CuI, DMF, 120 ^oC, 24 h. e) THF, H_2O, LiOH, Pd/C, H_2, overnight. f) $M(BF_4)_2$, EtOH, 95 ^oC, 4-24 h. Isolated yields in parentheses.

In order to confirm that any photophysical improvements were the result of the hemicaging of the complex, the corresponding 3,8-diisopropylphenanthroline was also synthesized (Scheme 4-4). This synthesis was accomplished in one step by the condensation of 1,2-phenylenediamine with 3-methyl-2-methylenebutanal. The use of freshly purified 1,2-phenylenediamine, slow addition of the acrolein, and use of activated charcoal to remove polymeric byproducts were all necessary to increase yields, but the highest reaction yield obtained was only 6 %. Complexation to Fe(II) and Zn(II) was accomplished by mixing the ligand and metal precursor in water-methanol mixtures,

followed by recrystallization. The corresponding Ru(II) complex required the use of microwave heating and ethylene glycol as a solvent in order to ensure the Ru center was fully complexed.

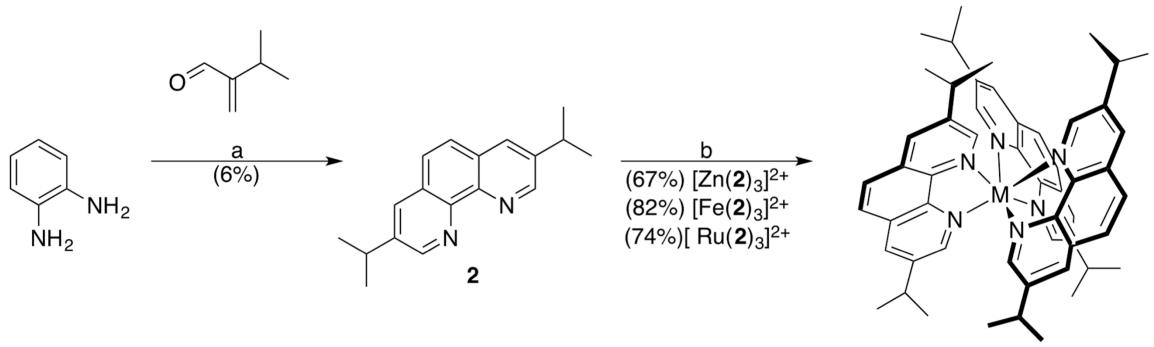

Scheme 4-4. Synthesis of phenanthroline ligand **2** and its corresponding metal complexes. Reaction conditions as follows: a) H_2O, H_2SO_4, NaI, 110 ^oC, 24 h b) $Zn(BF_4)_2$/$Fe(BF_4)_2$, MeOH, H_2O, RT, 1 h or $RuCl_3$, ethylene glycol, MW, 10 min. Isolated yields in parentheses.

While the use of a phenyl-capped hemicaging ligand is thought to impart additional rigidity to a metal complex, it has also been shown that a mesityl cap can introduce even more rigidity. Increases of quantum yields for Ru(III) complexes have been observed when switching from a phenyl cap to a mesityl cap.[5] As such, a mesityl analogue of the phenanthroline hemicage **1** was also pursued (Scheme 4-5). The previously used 3-bromo-8-isopropylphenanthroline was successfully coupled with the triethynylmesityl core. However, when the same hydrogenation protocol for **1** was used, only the semi-hydrogenated **3** was formed. This partial hydrogenation was confirmed by NMR and ESI-MS analysis of **3** as well as of the corresponding Zn(II) complex. A plausible rationale for the partial hydrogenation can stem from the fact that they mesityl cap's methyl groups and the bulky phenanthroline make it difficult for the precursor to add to the Pd/C catalyst in the necessary syn-orientation. Furthermore, several studies have shown that hydrogenation of an alkyne between two alkyl groups in the presence of

hydroxide result in selective partial hydrogenations, preferring the cis-alkene over the trans-alkene. [26–30]

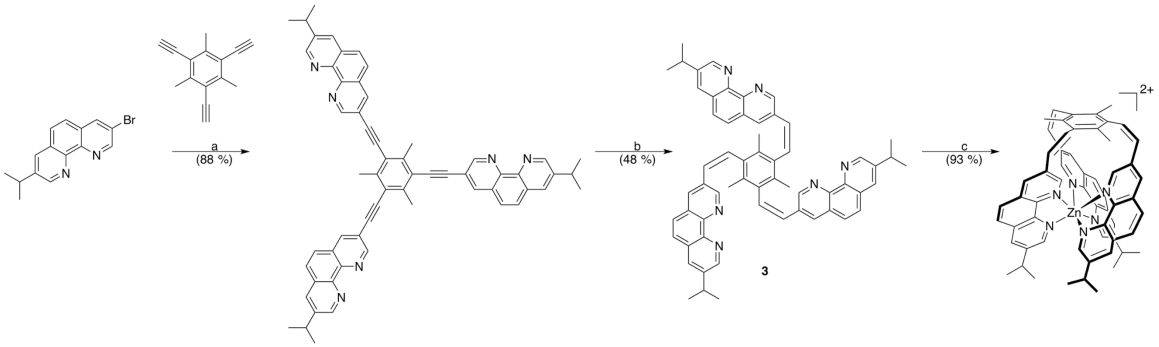

Scheme 4-5. Synthesis of mesityl capped phenanthroline hemicaging ligand **3** and its corresponding Zn(II) complex. Reaction conditions as follows: a) $Pd(PPh_3)_4$, CuI, DMF, 120 ^oC, 24 h. b) THF, H_2O, LiOH, Pd/C, H_2, overnight. c) $Zn(BF_4)_2$, EtOH, 95 ^oC, 24 h. Isolated yields in parentheses.

4.3.2 Absorption & Emission Spectroscopy

Table 4-1 summarizes the photophysical properties of the hemicaged Ru(II) complex $[Ru(\mathbf{1})]^{2+}$ along with the uncaged, diisopropyl phenanthroline complex and $[Ru(\mathbf{2})_3]^{2+}$ and $[Ru(bpy)_3]^{2+}$. The change from a bpy to a phenanthroline results in a large blue shift of the absorption maxima, whereas the maxima is only slightly impacted by hemicaging of the complex (Figure 4-4). A similar trend is observed in terms of the emission maxima, although all of the complexes still emit orange. Consistent with previous hemicaged complexes, there is an extension of the excited state lifetime of the hemicaged $[Ru(\mathbf{1})]^{2+}$ when compared to $[Ru(\mathbf{2})_3]^{2+}$. Unfortunately, the lifetime of $[Ru(\mathbf{2})_3]^{2+}$ was drastically lowered compared to $[Ru(bpy)_3]^{2+}$, likely due to the addition of the isopropyl groups. The quantum yield of $[Ru(\mathbf{1})]^{2+}$ was also improved when compared to the uncaged phenanthroline complex, but lower than that of the bipyridine complex. Likewise, the k_r of $[Ru(\mathbf{1})]^{2+}$ was enhanced compared to $[Ru(\mathbf{2})_3]^2$. Finally, the

k_{nr} of $[Ru(\mathbf{1})]^{2+}$ was slightly improved when compared to $[Ru(bpy)_3]^{2+}$, but when compared to the uncaged phenanthroline complex $[Ru(\mathbf{2})_3]^{2+}$, it was nearly 30 times less.

This photophysical enhancement can be ascribed to the changes in the ligand structure. Ligand dissociation upon photoexcitation is minimized since the ligands are tethered to the central cap. In addition, the rate of non-radiative decay is decreased due to an increase in rigidity of the complex. While it would have been expected that the more rigid phenanthroline backbone would have made the complex more photophysically efficient than the bpy complex, the rigidity of the ligand could not compensate for the additional non-radiative decay through the isopropyl groups. This resulted in a precipitous drop in the photophysical properties of $[Ru(\mathbf{2})_3]^{2+}$.

Table 4-1 Photophysical properties of Ru(II) complexes.

		emission				
complex	absorption λ_{max}/ nm (intensity/10^4 M^{-1} cm^{-1})	λ_{max} / nm	τ/ μs	Φ/ %	k_r (10^4) / s^{-1}	k_{nr} (10^5)/ s^{-1}
$[Ru(\mathbf{1})]^{2+}$	415 (1.61)	583	1.27	4.64	3.66	7.51
$[Ru(\mathbf{2})_3]^{2+}$	424 (1.63)	595	0.05	0.002	2.98	217.1
$[Ru(bpy)_3]^{2+}$	502 (1.48)	620	1.21	6.20	5.12	7.75

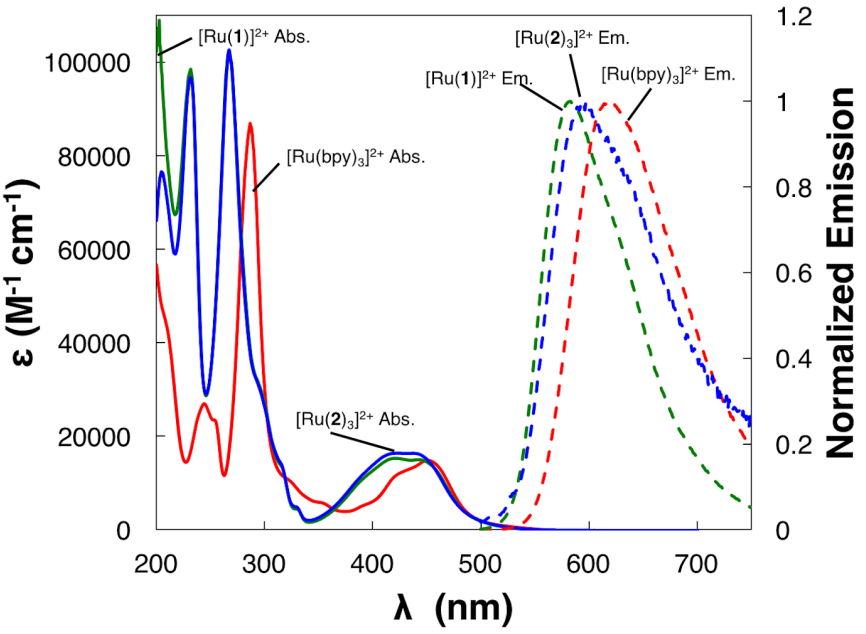

Figure 4-4 Normalized emission and UV-Vis absorption spectra of Ru(II) complexes. Spectra were obtained using argon-degassed 25 μM solutions in MeCN at room temperature.

Previously, it was discovered that the use of a hemicaging ligand with Zn(II) that had a mesityl cap would dramatically change the emissive properties when compared to the uncaged counterparts.[5] As shown in Figure 4-5, the emission of $[Zn(\mathbf{1})]^{2+}$ is identical to that of $[Zn(\mathbf{2})_3]^{2+}$, indicating that the addition of the cap did not impact the emission of the complex. This is also observed through the very similar quantum yield. Additionally, the excited state lifetimes of the two complexes were too short to be measured. When the unsaturated, mesityl-capped complex $[Zn(\mathbf{3})]^{2+}$ is evaluated, the emission maxima red shifts more than 100 nm and becomes much broader and structureless. Despite the changes in the emission spectra, the quantum yield was not improved. To evaluate if this change in emission structure corresponded to a switching from fluorescence to phosphorescence, oxygen quenching studies were performed (Figure 4-6). Marginal quenching was observed for the complexes, with the mesityl capped $[Zn(\mathbf{3})]^{2+}$ only being

slightly more easily quenched by oxygen quenching than the other complexes. Given the results are on the same orders of magnitude, it was concluded that this change in emission did not result from a change from fluorescence to phosphorescence.

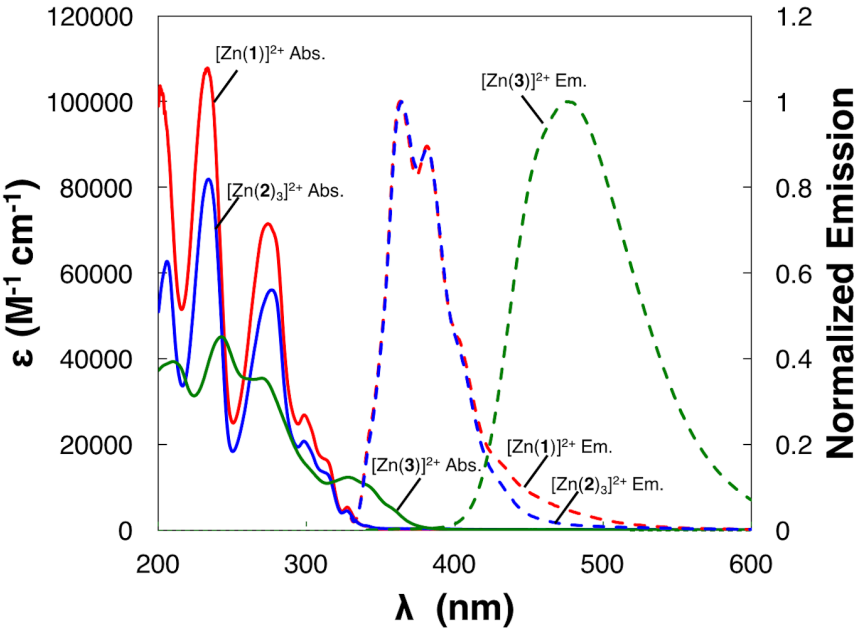

Figure 4-5 Normalized emission and UV-Vis absorption spectra of Zn(II) complexes. Spectra were obtained using argon-degassed 25 μM solutions in MeCN at room temperature.

Table 4-2 Photophysical properties of Zn(II) complexes.

		emission	
complex	absorption λ_{max}/ nm (intensity/10^4 M^{-1} cm^{-1})	λ_{max}/ nm	Φ/ %
$[Zn(\mathbf{1})]^{2+}$	298 (2.68)	364	17.2
$[Zn(\mathbf{2})_3]^{2+}$	297 (2.05)	364	15.5
$[Zn(\mathbf{3})]^{2+}$	270 (3.54)	477	14.2

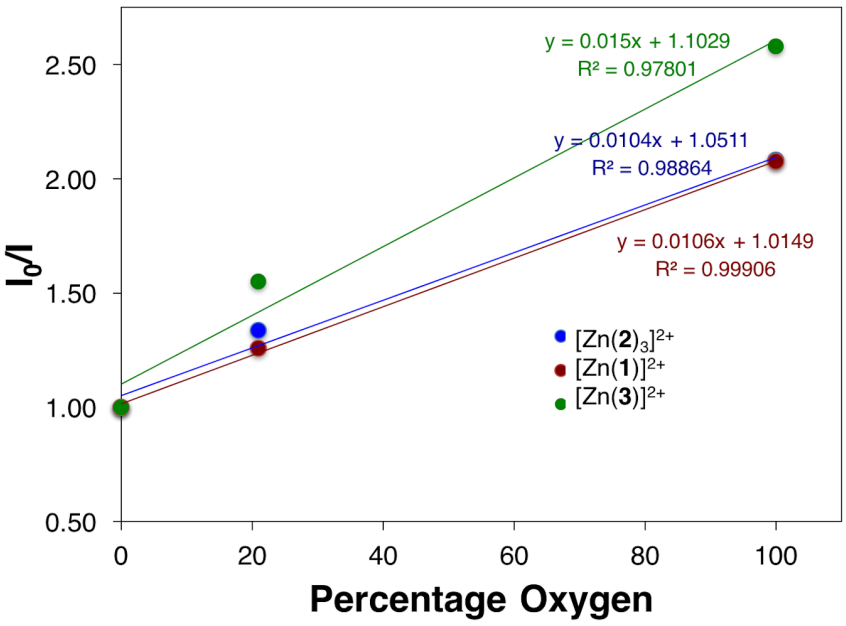

Figure 4-6 Emission quenching of Zn(II) complexes by oxygen.

Finally, the Fe(II) complexes were evaluated. Unfortunately, the changed ligand structure did not result in any detectable emission from the much more rigid Fe(II) hemicage complex. The absorption spectra of $[Fe(\mathbf{1})]^{2+}$ and $[Fe(\mathbf{2})_3]^{2+}$ appear identical, with only a marginal increase in the absorption around 350 nm (Figure 4-7). However, given the change in ligand structure and similarities in absorption, $[Fe(\mathbf{1})]^{2+}$ could potentially serve as a more stable, substitution inert alternative to $[Fe(bpy)_3]^{2+}$ based complexes.

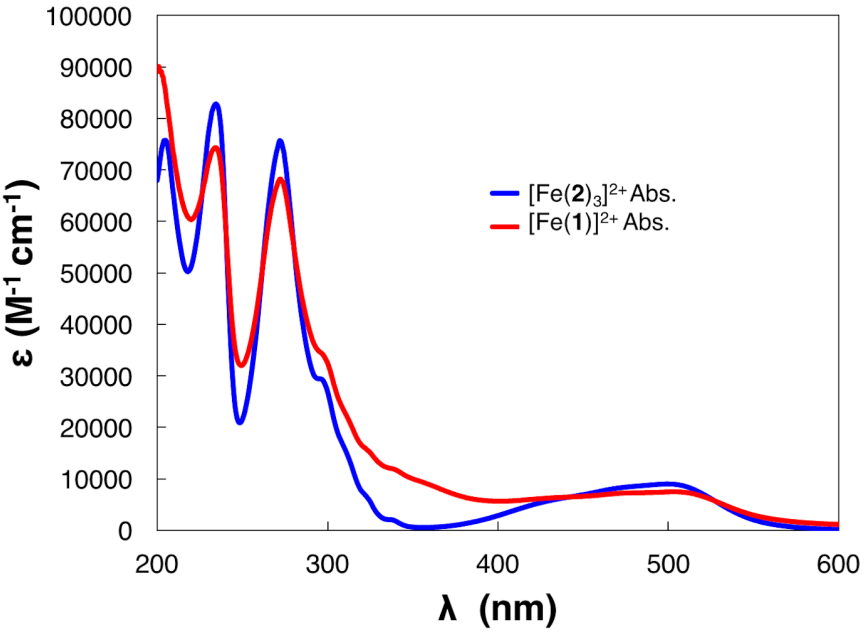

Figure 4-7 UV-Vis UV-Vis absorption spectra of Fe(II) complexes. Spectra were obtained using argon-degassed 25 μM solutions in MeCN at room temperature.

4.3.3 Electrochemical Characterization

The caging of metal complexes, while demonstrated to impart photochemical enhancement, is not expected to impact the electrochemistry of the complexes when the caged and uncaged version of the complexes are compared.[7,18,31] This is a useful feature of the caging process because it allows for ease of substation of a caged complex for its uncaged counterpart in applications including OLED fabrication, where differences in redox potential can impact device performance. As such, some of the complexes were analyzed by cyclic voltammetry to determine the effects of the hemicaging process. Due to lack of ample compound for analysis and the inability to recover samples after electrochemical analysis, [Ru(**1**)]$(PF_6)_2$ and [Zn(**3**)]$(BF_4)_2$ were not able to be analyzed.

The cyclic voltammograms of $[Fe(\mathbf{2})_3]^{2+}$ and $[Fe(\mathbf{1})]^{2+}$ both show three sequential, reversible reductions that correspond to one-electron reductions of each of the bidentate ligands (Figure 4-8). Hemicaging alters the $E_{1/2}$ of the first reduction, whereas the second

reduction is unaffected. The third reduction in $[Fe(\mathbf{1})]^{2+}$ is masked by solvent breakdown, but the $E_{1/2}$ is still close to that of $[Fe(\mathbf{2})_3]^{2+}$. The metal centered oxidations are also unaffected by hemicaging, and remain reversible in both complexes. When compared to $[Fe(bpy)_3]^{2+}$ the oxidation and reduction potentials are consistent with that of $[Fe(\mathbf{1})]^{2+}$ and $[Fe(\mathbf{2})_3]^{2+}$ demonstrate that these complexes can serve as more stable replacements for $[Fe(bpy)_3]^{2+}$ (Table 4-3).[32]

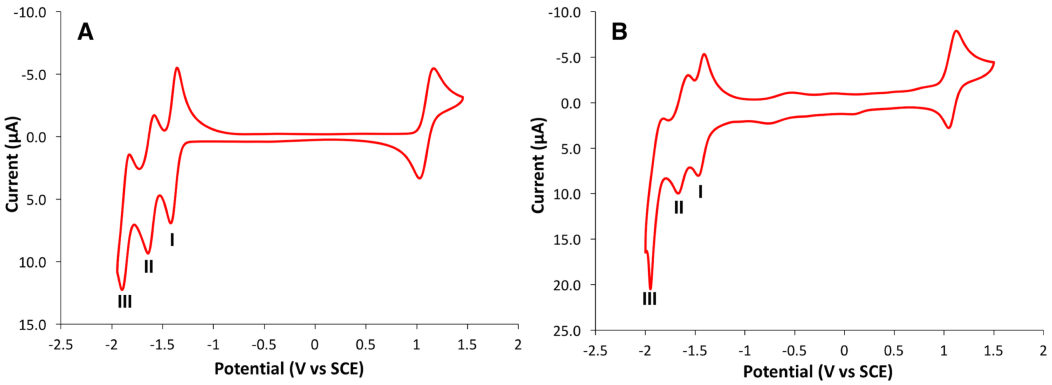

Figure 4-8 Cyclic voltammograms of $[Fe(\mathbf{2})_3]^{2+}$ (A) and $[Fe(\mathbf{1})]^{2+}$ (B). Roman numerals indicate the different reductions observed. Voltammograms were recorded with argon-degassed acetonitrile solutions containing 0.10 M tetra-n-butylammonium hexafluorophosphate as the electrolyte and 0.5 mM of analyte. Scans recorded at 0.10 V/s with a three-electrode system. All potentials are referenced to SCE using ferrocene as an internal standard ($fc/fc^+ = 0.40$ V).[15]

Table 4-3. Electrochemical Properties of Fe(II) complexes and $[Fe(bpy)_3]^{2+}$.[32]

compound	oxidation	reduction		
	E_{pa}/V	**I:** $E_{1/2}$/V	**II:** $E_{1/2}$/V	**III:** $E_{1/2}$/V
$[Fe(\mathbf{1})]^{2+}$	+1.08	-1.44	-1.62	-1.90
$[Fe(\mathbf{2})_3]^{2+}$	+1.10	-1.38	-1.61	-1.86
$[Fe(bpy)_3]^{2+}$	+1.06[32]	-1.35[32]	-1.54[32]	-1.78[32]

When analyzing the corresponding Zn(II) complexes $[Zn(\mathbf{2})_3]^{2+}$ and $[Zn(\mathbf{1})]^{2+}$, hemicaging does not appear to alter the electrochemical properties (Figure 4-9). Both complexes still have an oxidation that is beyond the stability window of acetonitrile. There are two reductions observed, however their reversibility is masked by the overlap

of the of $Zn^{2+/0}$ plating onto electrode. The observed potentials are not affected between the cage and uncaged ligand structures (Table 4-4). When compared to $[Zn(bpy)_3]^{2+}$, the change in ligand structure from a bpy to a phenanthroline, caged or uncage, does not impart any electrochemical changes that would indicate any electrochemical benefit to caging of the Zn(II) complex.

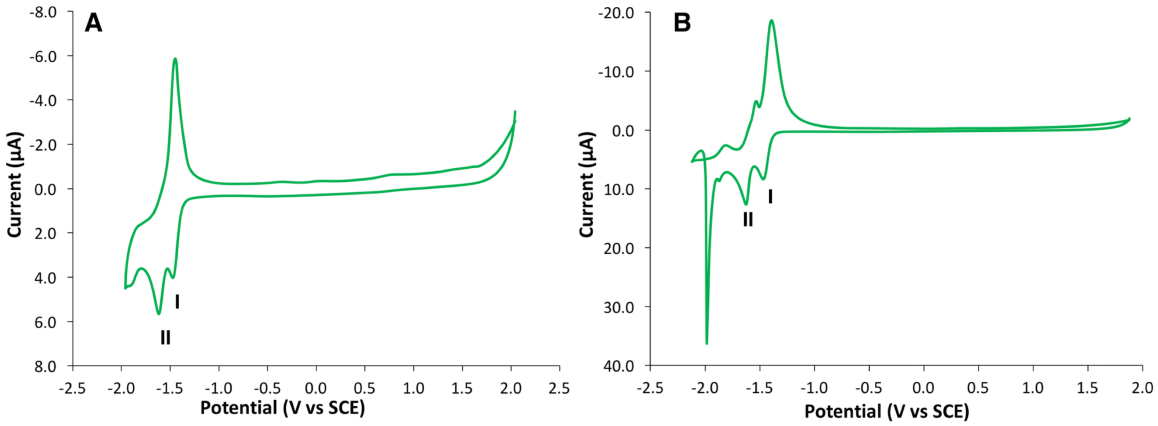

Figure 4-9 Cyclic voltammograms of $[Zn(\mathbf{2})_3]^{2+}$ (A) and $[Zn(\mathbf{1})]^{2+}$ (B). Roman numerals indicate the different reductions observed. Voltammograms were recorded with argon-degassed acetonitrile solutions containing 0.10 M tetra-n-butylammonium hexafluorophosphate as the electrolyte and 0.5 mM of analyte. Scans recorded at 0.10 V/s with a three-electrode system. All potentials are referenced to SCE using ferrocene as an internal standard ($fc/fc^+ = 0.40$ V).[15]

Table 4-4 Electrochemical Properties of Zn(II) complexes and $[Zn(bpy)_3]^{2+}$.[33] [a] Overlap of $Zn^{2+/0}$ plating onto electrode and complex reduction.

compound	oxidation	reduction[a]	
	E_{pa}/V	**I** (2e): $E_{1/2}$/V	**II:** $E_{1/2}$/V
$[Zn(\mathbf{1})]^{2+}$	>+2.20	-1.47	-1.62
$[Zn(\mathbf{2})_3]^{2+}$	>+2.20	-1.48	-1.62
$[Zn(bpy)_3]^{2+}$	>+2.30[33]	-1.37[33]	-1.85[33]

The addition of the isopropyl groups to the phenanthroline does alter the redox potentials of $[Ru(\mathbf{2})_3]^{2+}$ when compared to the corresponding bpy and phenanthroline analogues. The reversible, metal centered oxidation is made significantly easier compared to the bpy and phenanthroline analogues, owing to the increased electron density from the

isopropyl groups. Meanwhile, the reversible reductions I is in proximity to that of $[Ru(phen)_3]^{2+}$, indicating there is less of an impact on the functionality of the phenanthroline. However, the second and third reductions are more negative than the unsubstituted phenanthroline.

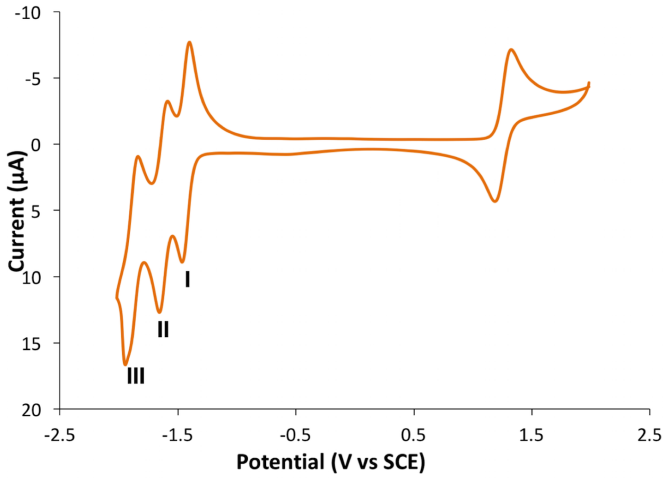

Figure 4-10 Cyclic voltammogram of $[Ru(\mathbf{2})_3]^{2+}$. Roman numerals indicate the different reductions observed. Voltammogram was recorded with an argon-degassed 0.10 M tetra-n-butylammonium hexafluorophosphate (acetonitrile) solution containing 0.5 mM of analyte, at 0.10 V/s with a three-electrode system. All potentials are referenced to SCE using ferrocene as an internal standard (fc/fc^+ = 0.40 V).[15]

Table 4-5 Electrochemical Properties of Ru(II) complex $[Ru(\mathbf{2})_3]^{2+}$, $[Ru(bpy)_3]^{2+}$, and $[Ru(phen)_3]^{2+}$.[34]

compound	oxidation	reduction		
	E_{pa}/V	**I**: $E_{1/2}$/V	**II:** $E_{1/2}$/V	**III:** $E_{1/2}$/V
$[Ru(\mathbf{2})_3]^{2+}$	+1.26	-1.43	-1.63	-1.89
$[Ru(bpy)_3]^{2+}$	+1.35[34]	-1.33[34]	-1.51[34]	-1.76[34]
$[Ru(phen)_3]^{2+}$	+1.40[34]	-1.41[34]	-1.54[34]	-1.84[34]

4.4 Conclusions

Two new hemicaging ligands, a benzene capped structure **1** and a mesitylene linked chelator **3** were successfully synthesized and complexed to Fe(II), Zn(II) and Ru(II). While ligand **1** was successfully made through a Sonogashira coupling followed by complete hydrogenation of the alkyne, ligand **3** was obtained as a result of an unexpected,

partial hydrogenation. Photophysical results from the Ru(II) based complexes revealed that while the complexes had higher quantum yields, higher k_r, and lower k_{nr} than the corresponding diisopropylphenanthroline complex, the complex was not significantly improved over $[Ru(bpy)_3]^{2+}$. When benzene capped $[Zn(\mathbf{1})]^{2+}$ was compared to mesityl capped $[Zn(\mathbf{3})]^{2+}$, a change in the emission maxima and structure was observed and thought to be a change from fluorescence to phosphorescence. However, similar quantum yields and a weak quenching by oxygen indicated that this change had not occurred. Electrochemically, the complexes of **1** were shown to have nearly identical redox potentials while still having a more stable ligand structure, meaning they could serve as replacements for their uncaged counterparts with little to no electrochemical issues. Future work could involve changing the functionalities on the phenanthroline to see their effects on the photophysical properties of the complexes, and have a site to functionalize for specific applications. It can also be envisioned that a completely caged "cryptate" version of this complex could be made and provide additional photophysical enhancement.

4.5 References

(1) Izatt, R. M.; Izatt, S. R.; Bruening, R. L.; Izatt, N. E.; Moyer, B. A. *Chem. Soc. Rev.* **2014**, *43*, 2451–2475.
(2) Juris, A.; Valzani, V.; Barigelletti, F.; Campagna, S.; Belser, P.; von Zelewsky, A. *Coord. Chem. Rev.* **1988**, *84*, 85–277.
(3) Bernhard, S.; Barron, J. A.; Houston, P. L.; Abruña, H. D.; Ruglovksy, J. L.; Gao, X.; Malliaras, G. G. *J. Am. Chem. Soc.* **2002**, *124*, 13624–13628.
(4) Kalyanasundaram, K. *Photochemistry of Polypyridine and Porphyrin Complexes*; Academic Press: New York, 1992.
(5) Oyler, K. D.; Coughlin, F. J.; Bernhard, S. *J. Am. Chem. Soc.* **2007**, *129*, 210–217.
(6) Wang, J.; Oyler, K. D.; Bernhard, S. *Inorg. Chem.* **2007**, *46*, 5700–5706.
(7) Barigelletti, F.; Cola, L. De; Balzani, V.; Belser, P.; Zelewsky, A. Von; Vogtle, F.; Ebmeyer, F.; Grammenudild, S. *J. Am. Chem. Soc.* **1989**, *111*, 4662–4668.
(8) St-Pierre, G.; Ladouceur, S.; Fortin, D.; Zysman-Colman, E. *Dalton Trans.* **2011**, *40*, 11726–11731.

(9) Ruggi, A.; Berenguel Alonso, M.; Reinhoudt, D. N.; Velders, A. H. *Chem. Commun.* **2010**, *46*, 6726–6728.
(10) Goze, C.; Chambron, J.-C.; Heitz, V.; Pomeranc, D.; Salom-Roig, X. J.; Sauvage, J.-P.; Morales, A. F.; Barigelletti, F. *Eur. J. Inorg. Chem.* **2003**, *2003*, 3752–3758.
(11) Beeston, R. F.; Aldridge, W. S.; Treadway, J. A.; Fitzgerald, M. C.; DeGraff, B. A.; Stitzel, S. E. *Inorg. Chem.* **1998**, *37*, 4368–4379.
(12) Higashihara, G.; Inagaki, A.; Akita, M. *Dalton Trans.* **2008**, 1888–1898.
(13) Zysman-Colman, E.; Denis, C. *Coord. Chem. Rev.* **2012**, *256*, 1742–1761.
(14) Saitoh, Y.; Koizumi, T.; Osakada, K.; Yamamoto, T. *Can. J. Chem.* **1997**, *75*, 1336–1339.
(15) Connelly, N. G.; Geiger, W. E. *Chem. Rev.* **1996**, *96*, 877–910.
(16) Ruggi, A.; Mauro, M.; Polo, F.; Reinhoudt, D. N.; De Cola, L.; Velders, A. H. *Eur. J. Inorg. Chem.* **2012**, 1025–1037.
(17) Schaffner-Hamann, C.; Von Zelewsky, A.; Barbieri, A.; Barigelletti, F.; Muller, G.; Riehl, J. P.; Neels, A. *J. Am. Chem. Soc.* **2004**, *126*, 9339–9348.
(18) Beeston, R. F.; Larson, S. L.; Fitzgerald, M. C. *Inorg. Chem.* **1989**, *28*, 4187–4189.
(19) Accorsi, G.; Listorti, A.; Yoosaf, K.; Armaroli, N. *Chem. Soc. Rev.* **2009**, *38*, 1690.
(20) Liu, S.; Michel, C.; Schmittel, M. *Org. Lett.* **2000**, *2*, 3959–3962.
(21) Sammes, P. G.; Yahioglu, G. *Chem. Soc. Rev.* **1994**, 327–334.
(22) Katritzky, A. R.; Long, Q. H.; Malhotra, N.; Ramanarayanan, T. A.; Vedage, H. *Synthesis (Stuttg)*. **1992**, *10*, 911–913.
(23) Bernhard, S.; Takada, K.; Jenkins, D.; Abruña, H. D. *Inorg. Chem.* **2002**, *41*, 765–772.
(24) Tzalis, D.; Tor, Y.; Failla, S.; Siegel, J. S. *Tetrahedron Lett.* **1995**, *36*, 3489–3490.
(25) Nishimura, S. *Handbook Of Heterogenous Catalytic Hydrogenation For Organic Synthesis*; John Wiley & Sons, Inc.: New York, 2001.
(26) Mori, H.; Matsuo, T.; Yoshioka, Y.; Katsumura, S. *Tetrahedron Lett.* **2001**, *42*, 3093–3095.
(27) Mori, H.; Matsuo, T.; Yoshioka, Y.; Katsumura, S. *J. Org. Chem.* **2006**, *71*, 9004–9012.
(28) Lei, C.; Jin, X.; Zhou, J. *ACS Catal.* **2016**, *6*, 1635–1639.
(29) Tedeschi, R. J.; Clark Jr, G. *J. Org. Chem.* **1962**, *27*, 4323–4326.
(30) Li, J.; Hua, R.; Liu, T. *J. Org. Chem.* **2010**, *75*, 2966–2970.
(31) Balzani, V.; Sabbatini, N.; Scandola, F. *Chem. Rev.* **1986**, *86*, 319–337.
(32) Sawyer, D. T. *J. Mol. Catal. A Chem.* **2003**, *194*, 53–67.
(33) Richert, S. A.; Tsang, P. K. S.; Sawyer, D. T. *Inorg. Chem.* **1989**, *28*, 2471–2475.
(34) Kirsch-De Mesmaeker, A.; Nasielski-Hinkens, R.; Maetens, D.; Pauwels, D.; Nasielski, J. *Inorg. Chem.* **1984**, *23*, 377–379.